# *Versatile nonlinear frequency conversion sources in the near- and mid-infrared*

**Sukeert**

# Versatile nonlinear frequency conversion sources in the near- and mid-infrared

**Sukeert**

*Universitat Politècnica de Catalunya*

*Barcelona, December 2021*

*Doctorate Program*: **Photonics**

*Duration*: **2017-2021**

*Thesis advisor:* **Prof. Majid Ebrahim-Zadeh**

*Thesis co-advisor:* **Dr. Chaitanya Kumar Suddapalli**

**Thesis submitted in partial fulfillment of the requirements**
**for the degree of Doctor of Philosophy of the**
**Universitat Politècnica de Catalunya**

# Declaration

I hereby declare that the matter embodied in the thesis entitled, **"Versatile nonlinear frequency conversion sources in the near- and mid-infrared"** is the result of investigations carried out by me at ICFO- The Institute of Photonic Sciences, Castelldefels, Barcelona, Spain under the supervision of Prof. Majid Ebrahim-Zadeh, and Dr. Chaitanya Kumar Suddapalli, and that it has not been submitted elsewhere for the award of any degree or diploma. In keeping with the general practice in reporting scientific observations, due acknowledgment has been made whenever the work described is based on the findings of other investigators.

Sukeert

# Certificate

I hereby certify that the matter embodied in this thesis entitled, **"Versatile nonlinear frequency conversion sources in the near- and mid-infrared"** has been carried out by Mr. Sukeert at ICFO- The Institute of Photonic Sciences, Castelldefels, Barcelona, Spain, under my supervision, and that it has not been submitted elsewhere for the award of any degree or diploma.

Prof. Majid Ebrahim-Zadeh
(**ICFO, Thesis advisor)**

Dr. Chaitanya Kumar Suddapalli
(**ICFO, Thesis co-advisor)**

# Acknowledgements

This thesis would not have been possible without the constant help, support and encouragement of many people, and I would like to express my gratitude towards them. However, I have realized that I do not do a good job of it in general, nevertheless I shall try my best.

First of all, I would like to thank my thesis advisor, Majid Ebrahim-Zadeh for giving me the opportunity to work under his supervision for my PhD. His research advice and guidance, support and constant encouragement have been invaluable. The pleasant, cheerful and constructive atmosphere that he has ensured in the group has made my journey very enriching and enjoyable. I would also like to thank my thesis-co advisor, Chaitanya Kumar Suddapalli for sharing his knowledge and experience, being my mentor, enduring me for countless discussions, preparing delicious food, and always being there to support and guide me, in and outside lab. I am thankful to Antoniangelo Agnesi, Christian Pedersen and Pablo Loza-Alvarez for reviewing my thesis.

I would like to thank Kavita, with whom I did my first project, for sharing her experience and knowledge, and all the fun discussions that we had along with Anuja. It was a delight to share my office with Anuja, Hanyu, and Joe. I would like to thank my other labmates, Biplob, Callum, Pep, Jun, Shahrzad, Gyanendra and Alfredo for their help and support. I would also like to thank Alfredo for translating the abstract into Spanish.

The move to Barcelona (or rather Castelldefels) and dealing with various administrative procedures during my stay would not have been possible without the help of people at HR. I would like to thank Manuela, Anne and Ingrid for

helping me and taking care of administrative parts related to my move, work and stay. Anne has been really helpful in sorting out all logistic issues, and my experience of living in Castelldefels, and dealing with external bureaucracy would not be the same without her. I would also like to thank Laia, Mery, Mireia, Rut, Anna and all the other HR staff for their help. ICFO runs like a well-oiled machine and this has been made possible due to the leadership and management of Lluis and Dolors. I am also indebted to the mechanical workshop team led by Xavier and the electronic workshop team led by Jose. I would also like to thank Santi, Magda, Maria and others from the travel and purchasing unit, Carlos, Nuria and others from facilities, ICFO frontdesk, KTT, the communications and events team, and the IT team led by Oriol. A shout-out to the IT team for ensuring my name was correct on all IT related resources.

The life of PhD student can be difficult at times, and I would like to thank the board members of ICONS for spending their time and energy to improve the life of every PhD student at ICFO. Being a part of the IONS organizing team was a gratifying experience, and I would like to thank all the team members for it. The ICFO football team also deserves a mention here.

My motivation to pursue research was strongly influenced by my experience during internships. I would like to thank Deepak Mathur, S.V.K. Kumar and Hema Ramachandran for giving me a chance to work in their labs. I am grateful to all the teachers who taught me, and especially the optics faculty, S. Duttagupta, V.S. Ashoka, N. Vishwanathan, D.N.R. Rao, P. Ananthlakshmi. N. Sriramgopal and Suneel Singh, at the University of Hyderabad. I would also like to thank A.K. Bhatnagar, Avanish Parmar, Jayeeta Lahiri, and Karoline Pershell for guiding me through the PhD admission process.

Many names come to my mind when I think of friends in Barcelona who have helped me at different times, and have included me in various social activities. Many of them have made delicious food without expecting much in return. I have also gone on trips with some of them and they have been memorable. Aamir, Anubhav, Arindam, Avijit, Biswajit, Chandan, Charithra, Chetan, Debraj, Gaurav, Himanshu, Hitesh, Hyun-Soo, Ipsita, Kavitha, Mamatha, Manabendra, Mohit, Monserrat, Pandian, Parmeshwar, Rajashree, Rinu, Roop, Samyobrata, Sandhya, Santanu, Saptam, Siddarth, Srividya, Stephy, Stuti, Sumana, Swapan, Utso, Varun, Vikas, Vindhiya, Vrinda, Zoraze, thank you for creating cherishable moments. It was great to have Dnyanada, Ameya, and Lily for long stays at my place. I would like to thank Prashant, Diksha, Vivek, Kris and Cindy for making me feel at home when I was in the US. Some people have been bearing me for more than a decade now. Vamsi, Surya Abhishek, Praneeth, Sahithi, Nithin, and Debalina deserve credit for that.

I would like to express my gratitude to my grandparents and my parents for their love and support, and being there for me at every stage of my life. This thesis would not have been possible without them.

# Abstract

Tunable laser sources in different spectral regions are of interest for a variety of applications including spectroscopy, trace gas sensing, medical diagnostics, LIDAR and material processing. Existing lasers have limited tunability and many spectral regions continue to remain inaccessible to lasers due to lack of suitable gain media. Nonlinear frequency conversion is a viable approach to cover such difficult spectral regions in the visible, near and mid-infrared (mid-IR).

Optical parametric oscillators (OPO) can provide wide wavelength tunability with high output powers in good beam quality across continuous-wave (cw), nanosecond and ultrafast picosecond and femtosecond time-scales. With the development of quasi-phase-matched (QPM) nonlinear materials in fan-out grating structure, wide wavelength tuning is possible at a fixed temperature, enabling the development of rapidly tunable devices for practical applications. Difference-frequency-generation (DFG) is also an attractive approach for generating high powers in the mid-IR in a single-pass scheme.

In this thesis, we have developed second-order nonlinear frequency conversion sources based on nanosecond and cw OPOs and cw DFG. Widely tunable green-pumped OPOs have been developed by using fan-out grating structure for the first time in different nonlinear materials, and a high-power cw source in the mid-IR has been developed by exploiting DFG. The sources developed in this thesis cover a wavelength range spanning 677-2479 nm. One of the OPOs developed in this work has also been deployed in an industrial environment in a device characterization setup.

In green-pumped OPOs, we demonstrate a widely tunable cw OPO based

on PPKTP in a fan-out grating structure. The OPO is continuously tunable across 742-922 nm in the signal, and 1258-1884 nm in the idler. Resonant wave output coupling has been deployed to extract useful signal power and reduce the thermal load, and the OPO can deliver up to 1.65 W of total output power. The use of output coupling results in superior performance of the OPO over pure singly-resonant oscillator (SRO) configuration.

We also develop the first green-pumped OPO based on MgO:cPPLT. Continuous wavelength tuning across 689-1025 nm in the signal and 1106-2336 nm in the idler at room temperature has been achieved in the nanosecond OPO by using a fan-out grating structure. The OPO can provide up to 131 mW of average output power at 25 kHz repetition rate, and the idler passive power stability is 3.9% rms over 30 minutes.

A cw OPO based on MgO:PPLN in a fan-out grating design is then described. The OPO is continuously tunable across 813-1032 nm in the signal and 1098-1539 nm in the idler. A short crystal length and signal output coupling are used to minimise thermal effects, and the OPO can generate up to 710 mW of total output power with signal and idler passive power stabilities better than 2.8% rms and 1.8% rms, respectively over 1 hour and signal $M^2 < 1.1$.

As a part of an industrial internship, a cw green-pumped MgO:PPLN OPO is developed at Radiantis. The OPO is used as the input light source of a device characterization setup to test sensors for the aerospace sector. Compared to the existing light source, using the OPO results in orders-of magnitude-higher response of the InGaAs sensor, leading to a more precise and accurate characterization, and lower measurement error, thus improving the device evaluation process.

Finally, we demonstrate a high-power cw source at 2.26 µm using the DFG process. The source can deliver up to 3.84 W of output power at 2262 nm, with a power stability better than 0.6% rms over 1 hour, in a Gaussian mode profile with $M^2 < 1.2$.

# Resumen

Los láseres sintonizables en diferentes regiones espectrales presentan una amplia variedad de aplicaciones que incluyen espectroscopía, sensado de gases, diagnóstico clínico, LIDAR y procesamiento de materiales, entre otras. Los láseres existentes tienen una sintonizabilidad limitada y muchas porciones del espectro permanecen aún inaccesibles debido a la falta de medios activos con ganancia en dicha región. Un enfoque viable para cubrir las regiones espectrales en los rangos visible, infrarrojo cercano e infrarrojo medio (mid-IR) es mediante la conversión no lineal de frecuencias.

Los osciladores paramétricos ópticos (OPO) proporcionan un amplio rango de sintonizabilidad con altas potencias y con calidad de haz excelente en escalas de tiempo de onda continua (cw), pulsado en nanosegundo y ultra rápido (picosegundo y femtosegundo). Con el desarrollo de materiales no lineales que presentan la propiedad de quasi-phase-matching (QPM) con estructura de red del tipo fan-out es posible sintonizar, a una temperatura fija, un amplio rango de longitudes de onda que habilitan el desarrollo de dispositivos sintonizables para aplicaciones prácticas en las que se requieran cambios de longitudes de onda de manera rápida. El proceso no lineal de generación de diferencia de frecuencias (DFG) es un enfoque atractivo para la generación de potencias altas en el mid-IR en esquemas de un solo paso a través del medio no lineal (single pass).

En esta tesis se desarrollan fuentes de luz basadas en la conversión de frecuencias no lineal de segundo orden usando OPOs en los regímenes de cw y nanosegundos, y de cw que usan el proceso de DFG. Se desarrollan por primera vez OPO sintonizables bombeados por un láser verde usando estructuras de red

fan-out en diferentes materiales no lineales. Además, se desarrolla una fuente de cw de alta potencia en el mid-IR al explotar el proceso de DFG. El rango de las fuentes desarrolladas en esta tesis cubren el intervalo de longitudes de onda de 677-2479 nm. Uno de los OPOs que se desarrollan en este trabajo se utilizó en un ambiente industrial como parte de un dispostivo de caracterización de sensores.

En OPOs con láser de bombeo verde, se demuestra un OPO de cw ampliamente sintonizable basado en un cristal PPKTP que posee una estructura de red fan-out. La señal generada por el OPO es sintonizable continuamente en el intervalo 742-922 nm, mientras que el idler puede sintonizarse en el intervalo 1258-1884 nm. El acoplamiento de salida de la onda resonante se usó para extraer potencia de señal útil y reducir la carga térmica. Este OPO puede entregar una potencia total de salida de hasta 1.65 W. El uso del acoplamiento de salida da como resultado un rendimiento superior del OPO a la configuración de oscilador resonante individual (SRO) pura.

Se realiza la primera demostración de un OPO bombeado por láser verde basado en un cristal no lineal de MgO:cPPLT. Se consiguió a temperatura ambiente un intervalo de longitudes de onda para la señal de 689-1025 nm, y para el idler de 1106-2336 nm, en el OPO que opera en el régimen del nanosegundo usando una estructura de red fan-out. El OPO puede proveer hasta una potencia media de salida de 131 mW a una tasa de repetición de 25 kHz, mientras que la estabilidad pasiva de potencia de idler es 3.9% medida durante 30 minutos.

Seguidamente se desarrolló un OPO de cw basado en un cristal no lineal de MgO:PPLN con un diseño de red del tipo fan-out. La señal generada en el OPO puede sintonizarse de manera continua en el rango de 813-1032 nm, mientras que el idler puede sintonizarse en el rango de 1098-1539 nm. Se utiliza un cristal de

longitud corta y un acoplamiento de salida de la señal para minimizar los efectos térmicos. El OPO puede generar hasta 710 mW de potencia de salida total con una estabilidad pasiva de potencia de señal y de idler mejores que 2.8% rms y 1.8% rms, respectivamente, a lo largo de una hora, y con un valor $M^2 < 1.1$ para la señal.

Luego se describe el desarrollo del OPO con bombeo verde de cw basado en un cristal no lineal de MgO:PPLN en el entorno industrial de la compañía Radiantis. El mismo se utiliza como la fuente de luz de entrada en un esquema de caracterización de dispositivos con el propósito de probar sensores para el sector aeroespacial. En comparación con la fuente de luz existente, el uso de OPO da como resultado una respuesta de órdenes de magnitud mayor que la de un sensor de InGaAs, lo que lleva a una caracterización más precisa y exacta, y a un menor error de medición, mejorando de este modo el proceso de evaluación de los dispositivos.

Finalmente, se demuestra una fuente de cw de alta potencia que opera en una longitud de onda de 2.26 µm utilizando el proceso DFG. La fuente puede entregar hasta 3.84 W de potencia de salida a 2262 nm, con una estabilidad de potencia mejor que 0.6 % rms durante una hora, en un perfil de modo gaussiano y con $M^2 < 1.2$.

# Publications

## Journal publications

1. K. Devi, A. Padhye[*], **Sukeert**,[*] and M. Ebrahim-Zadeh, "Widely tunable room-temperature continuous-wave optical parametric oscillator based on periodically-poled $KTiOPO_4$," Optics Express **27**, 24093 (2019).
   [*] *equal contribution*

2. **Sukeert**, S. Chaitanya Kumar, and M. Ebrahim-Zadeh, "Green-pumped optical parametric oscillator based on fan-out grating periodically-poled MgO-doped congruent $LiTaO_3$," Optics Letters **44**, 5796 (2019).

3. **Sukeert**, S. Chaitanya Kumar, and M. Ebrahim-Zadeh, "Green-pumped continuous-wave parametric oscillator based on fanout–grating MgO:PPLN," Optics Letters **45**, 6486 (2020).

4. **Sukeert**, S. Chaitanya Kumar, and M. Ebrahim-Zadeh, "High-Power, Continuous-Wave, Fiber-Pumped Difference-Frequency-Generation at 2.26 µm," IEEE Photonics Technology Letters **33**, 627 (2021).

5. S. Chaitanya Kumar, **Sukeert**, and M. Ebrahim-Zadeh, "High-power continuous-wave mid-infrared difference-frequency generation in the presence of thermal effects," Journal of the Optical Society of America B **38**, B14 (2021).

## Conference publications

1. K. Devi, A. Padhye, **Sukeert**, and M. Ebrahim-Zadeh, "Widely tunable, green-pumped, visible and near-infrared continuous-wave optical parametric oscillator based on fan-out-grating PPKTP," in $8^{\text{th}}$ EPS-QEOD Europhoton Conference, Barcelona, Spain, September 2018, paper WeM2.2.

2. **Sukeert**, S. Chaitanya Kumar, and M. Ebrahim-Zadeh, "Green-pumped optical parametric oscillator based on fan-out-grating periodically-poled Mg-doped congruent $LiTaO_3$," in CLEO/Europe-EQEC, Munich, Germany, June 2019, paper CD-P.30.

3. **Sukeert**, S. Chaitanya Kumar, and M. Ebrahim-Zadeh, "Green-pumped optical parametric oscillator based on fanout-grating periodically-poled Mg-doped congruent $LiTaO_3$," in IEEE Photonics Conference (IPC), San Antonio, USA, September 2019, paper WC3.3.

4. **Sukeert**, S. Chaitanya Kumar, and M. Ebrahim-Zadeh, "Rapidly tunable continuous-wave green-pumped optical parametric oscillator based on fanout MgO:PPLN," in Conference on Lasers and Electro-optics (CLEO), San Jose, USA, May 2020, paper JTu2F.24.

5. **Sukeert**, S. Chaitanya Kumar, and M. Ebrahim-Zadeh, "Continuous-wave green-pumped optical parametric oscillator based on fanout MgO:PPLN," in IEEE Photonics Conference (IPC), September 2020, paper TuF2.5.

6. **Sukeert**, S. Chaitanya Kumar, and M. Ebrahim-Zadeh, "Continuous-wave difference-frequency-generation at 2.26 µm," in CLEO/Europe-EQEC, Munich, Germany, June 2021, paper CD-10.4.

7. **Sukeert**, S. Chaitanya Kumar, and M. Ebrahim-Zadeh, "Continuous-wave high-power fiber-based difference-frequency-generation at 2.26 µm," in IEEE Photonics Conference (IPC), October 2021, paper MD1.3.

# Contents

**List of Figures** **v**

**List of Tables** **xiii**

**List of Acronyms** **xv**

**1 Introduction** **1**

1.1 Background . . . . . 1

1.2 Thesis structure and overview . . . . . 8

References . . . . . 12

**2 Basics of nonlinear optics** **23**

2.1 Linear and nonlinear optics . . . . . 23

2.2 Optical nonlinearity . . . . . 24

2.3 Second-order nonlinear processes . . . . . 25

2.4 Second-order nonlinear susceptibility . . . . . 28

2.5 Coupled wave equations in nonlinear optics . . . . . 31

2.6 Phase-matching . . . . . 34

2.6.1 Birefringent phase-matching . . . 35
2.6.2 Quasi-phase-matching . . . 38
2.7 Optical parametric oscillator . . . 41
2.7.1 Oscillator configurations . . . 42
2.7.2 Gain, amplification, and threshold . . . 43
2.7.3 Phase-matching bandwidth . . . 46
2.7.4 Material requirements . . . 47
2.7.5 Wavelength tuning . . . 48
2.7.6 Cavity Design . . . 50
2.8 Difference-frequency-generation . . . 55
References . . . 57

**3 Widely tunable continuous-wave PPKTP optical parametric oscillator 61**

3.1 Motivation . . . 61
3.2 Experimental Setup . . . 64
3.2.1 Crystal Characterization . . . 66
3.3 Output-coupled SRO . . . 68
3.3.1 Wavelength tuning . . . 69
3.3.2 Power scaling and stability . . . 77
3.3.3 Performance with time . . . 81
3.3.4 Spectral characteristics . . . 83
3.3.5 Spatial beam profile . . . 86
3.4 SRO . . . 86
3.4.1 Wavelength tuning . . . 86
3.4.2 Power scaling and stability . . . 92
3.4.3 Spatial and spectral characteristics . . . 93
3.5 Conclusion . . . 95

References . . . . . 96

**4 Green-pumped nanosecond optical parametric oscillator based on MgO:cPPLT 101**

4.1 Motivation . . . . . 101

4.2 Experimental setup . . . . . 104

4.3 Results and discussion . . . . . 106

4.3.1 Wavelength tuning . . . . . 106

4.3.2 Power scaling . . . . . 110

4.3.3 Power stability . . . . . 113

4.3.4 Spatial and temporal characteristics . . . . . 114

4.4 Conclusion . . . . . 116

References . . . . . 118

**5 Green-pumped continuous-wave optical parametric oscillator based on fan-out grating MgO:PPLN 121**

5.1 Motivation . . . . . 121

5.2 Green-pumped cw OPO based on MgO:PPLN . . . . . 124

5.2.1 Experimental setup . . . . . 124

5.2.2 MgO:PPLN DRO . . . . . 126

5.2.3 MgO:PPLN SRO . . . . . 126

5.3 Results and discussion . . . . . 131

5.3.1 Wavelength tuning . . . . . 131

5.3.2 Power scaling and stability . . . . . 134

5.3.3 Spectral characteristics . . . . . 137

5.3.4 Spatial beam quality . . . . . 139

5.4 Conclusion . . . . . 140

References . . . . . 142

**6 Industrial internship** **147**

6.1 Motivation . . . 147

6.2 Experimental Setup . . . 151

6.3 Results . . . 153

6.3.1 OPO characterization . . . 153

6.4 Testing of components . . . 160

6.5 Conclusion . . . 162

References . . . 164

**7 High-power continuous-wave difference-frequency-generation at 2.26 µm** **165**

7.1 Motivation . . . 165

7.2 Experimental design . . . 169

7.3 Results and discussion . . . 174

7.3.1 Temperature acceptance bandwidth . . . 174

7.3.2 Power scaling, power stability, and thermal effects . . . 177

7.3.3 Spectral Characteristics . . . 185

7.3.4 Spatial profile and beam quality . . . 188

7.4 Conclusion . . . 191

References . . . 193

**8 Summary and outlook** **199**

# List of Figures


1.1 Emission wavelengths of some common solid-state lasers. . . . . 3

2.1 Second-order nonlinear frequency conversion processes. . . . . 27
2.2 Birefringent phase-matching in a uniaxial crystal. . . . . 37
2.3 Grating design in a quasi-phase-matched nonlinear crystal. . . . . 39
2.4 Evolution of field amplitude along the crystal length for perfect phase-matching, quasi-phase-matching, and no-phase-matching conditions. . . . . 40
2.5 Green-pumped QPM temperature tuning curves of MgO:cPPLT. . 49
2.6 Green-pumped QPM grating tuning curve of MgO:PPLN. . . . . 49
2.7 Cavity configurations for OPOs. . . . . 51
2.8 Signal beam waist in a ring cavity. . . . . 54

3.1 Schematic of the fan-out grating design PPKTP-based cw OPO. . 64
3.2 Transmission measurements of PPKTP crystal. . . . . 67
3.3 Wide wavelength tuning with lateral translation of PPKTP crystal at room temperature. . . . . 68

3.4 Theoretically calculated grating period corresponding to crystal position. . . . . 70
3.5 Theoretical temperature tuning curves. . . . . 71
3.6 Temperature tuning at a fixed grating period of $\Lambda = 9.28$ µm. . . . 72
3.7 Temperature tuning at a fixed grating period of $\Lambda = 10.58$ µm. . . 73
3.8 Variation of (a) signal, and (b) idler power across the grating period tuning range at room temperature. . . . . 74
3.9 Variation of (a) signal, and (b) idler power across the temperature tuning range for grating period of $\Lambda = 9.28$ µm. . . . . 75
3.10 Variation of (a) signal, and (b) idler power across the temperature tuning range for grating period of $\Lambda = 10.58$ µm. . . . . 76
3.11 Idler and signal output power as a function of pump power at room temperature. . . . . 78
3.12 Variation of signal wavelength with pump power at room temperature. . . . . 78
3.13 Passive power stability of the (a) idler output, and (b) extracted signal over 2.6 minutes. . . . . 80
3.14 Variation of signal and idler power, and corresponding signal wavelength with time when the crystal is exposed to the varying pump power over initial time period of 20 seconds. . . . . 81
3.15 Single-frequency spectrum of the extracted signal at 831 nm. . . . 84
3.16 Frequency stability of the extracted signal beam at 831 nm. . . . . 84
3.17 Signal spectra across the widely-tunable room temperature spectral range. . . . . 85
3.18 Far-field energy distribution of the extracted signal beam at 831 nm at room temperature. . . . . 85
3.19 Signal and idler wavelength tuning range at room temperature in SRO configuration. . . . . 87

3.20 Signal and idler wavelength tuning range at T= 50 ˚C in SRO configuration. . . . . 88
3.21 Idler output power across the grating tuning range at (a) room temperature, and (b) T=50 ˚C in SRO configuration. . . . . 89
3.22 Temperature tuning at a fixed grating period of $\Lambda = 9.41$ µm in SRO configuration. . . . . 90
3.23 Temperature tuning at a fixed grating period of $\Lambda = 10.55$ µm in SRO configuration. . . . . 90
3.24 Variation of idler power across the temperature tuning range for grating period of (a) $\Lambda = 9.28$ µm, and (b) $\Lambda = 10.55$ µm in SRO configuration. . . . . 91
3.25 Idler output power as a function of pump power at T=50 ˚C in SRO configuration. . . . . 92
3.26 Passive power stability of the output idler in SRO configuration. . 93
3.27 Some signal spectra across the room temperature tuning range in SRO configuration. . . . . 94
3.28 Far-field energy distribution of the signal beam at 838 nm. . . . . 94

4.1 Experimental setup of the green-pumped nanosecond OPO based on MgO:cPPLT. . . . . 105
4.2 Laboratory photograph of the cavity of the MgO:cPPLT nanosecond OPO. . . . . 105
4.3 Room-temperature tuning range of the green-pumped nanosecond MgO:cPPLT OPO. . . . . 107
4.4 Idler average power across the tuning range of the MgO:cPPLT nanosecond OPO while operating at room temperature. . . . . 107
4.5 (a) Temperature tuning, and (b) variation of idler power across the tuning range for the short grating period of $\Lambda = 8.14$ µm. . . . 108

4.6 (a) Temperature tuning, and (b) variation of idler power across the tuning range for the long grating period of $\Lambda = 10.15$ µm. . . . 109
4.7 Idler average power scaling as a function of pump power for the MgO:cPPLT nanosecond OPO. . . . . 111
4.8 Idler power scaling as a function of pump power modulated by a chopper for the MgO:cPPLT nanosecond OPO. . . . . 111
4.9 Transmission measurements of MgO:cPPLT. . . . . 112
4.10 Power stability of the (a) idler output from the MgO:cPPLT nanosecond OPO, and (b) pump over 30 min. . . . . 113
4.11 Idler beam profile from the OPO. . . . . 115
4.12 Temporal profile of the (a) pump pulse at 532 nm, and (b) signal pulse at 875 nm. . . . . 115

5.1 Configuration of green-pumped fanout–grating MgO:PPLN cw OPO. 125
5.2 Transmission of MgO:PPLN crystal at 532 nm in the phase-matched polarisation. . . . . 126
5.3 Temperature tuning at a fixed grating period of $\Lambda = 6.95$ µm using all highly reflecting mirrors. . . . . 127
5.4 Idler power across the temperature tuning range using all highly reflecting mirrors. . . . . 128
5.5 Change in idler output power when the aperture is open and closed at the idler wavelength of 1219 nm while using all highly reflecting mirrors. . . . . 129
5.6 Change in idler output power when the aperture is open and closed at the idler wavelength of 1411 nm using all highly reflecting mirrors. 129
5.7 Passive power stability of idler after increasing the pump beam waist, using all highly reflecting mirrors. . . . . 130

5.8 Signal and idler wavelength tuning range of the green-pumped cw OPO as a function of the MgO:PPLN fanout grating period at a fixed temperature of 55 °C. . . . . 132
5.9 (a) Idler, and (b) signal output powers across the tuning range of the green-pumped fanout–grating MgO:PPLN cw OPO. . . . . 133
5.10 Passive power stability of the (a) idler, and (b) extracted signal over 1 hour. . . . . 135
5.11 Passive power stability of the (a) idler, and (b) extracted signal over 1 hour. . . . . 135
5.12 Signal and idler power scaling as a function of pump power. . . . . 136
5.13 Frequency stability of the extracted signal beam at 890 nm. . . . . 137
5.14 Single-frequency spectrum of the extracted signal at 889.4 nm. . . 138
5.15 Some signal spectra across the grating tuning range. . . . . 138
5.16 Spatial beam profile of (a) signal at 889 nm, and (b) idler at 1324 nm. . . . . 139
5.17 Measured signal beam quality factor at 952 nm . . . . . 140

6.1 Example spectra for different slits and grating configurations of a monochromator used with a tungsten-halogen lamp. . . . . 150
6.2 Schematic of green-fiber-pumped fan-out grating MgO:PPLN cw OPO with the device characterization setup. . . . . 152
6.3 Laboratory photograph of the green-pumped cw OPO developed at Radiantis along with the device characterization setup. . . . . 152
6.4 Wavelength tuning range of the green-pumped cw OPO as a function of the MgO:PPLN fanout grating period at a fixed temperature of 70 °C. . . . . 154
6.5 Wavelength tuning at a fixed grating period of $\Lambda = 6.96$ µm. . . . 155

6.6 Idler output power across the tuning orange of the green-pumped cw OPO. . . . . 155

6.7 Passive power stability of the idler for the idler wavelength of (a) 1230 nm at T=55 °C, (b) 1360 nm at T=70 °C, and (c) 1184 nm at T=70 °C . . . . . 156

6.8 Variation of idler power as a function of input pump power for the green-pumped cw OPO. Inset: spatial beam profile of the idler at 1265 nm. . . . . 157

6.9 Idler spectra across the tuning range of the green-pumped cw OPO. 159

6.10 Example spectra from the monochromator for grating with 300g/mm and slit of 0.6 mm. . . . . 159

6.11 Comparison of the idler and monochromator spectra around 1200 nm, along with an example of the corresponding photocurrent measured in DUT. . . . . 160

6.12 DUT photocurrent, and power of reference detector as a function of wavelength when using monochromator on the tungsten-halogen lamp as the input light source. . . . . 161

6.13 DUT photocurrent, and power of reference detector as a function of wavelength when using green-pumped cw OPO as the input light source. . . . . 161

7.1 Schematic of the experimental setup for cw single-pass DFG based on MgO:PPLN. . . . . 170

7.2 Transmission of the 50-mm-long MgO:PPLN crystal at (a) pump, and (b) signal wavelength in phase-matched polarization. . . . . 171

7.3 Theoretical normalized DFG efficiency as a function of the phase-matching temperature. . . . . 172

7.4 Normalized DFG efficiency as a function of pump wavelength together with the pump spectra. . . . . 173
7.5 Normalized DFG efficiency as a function of signal wavelength together with the signal spectra. . . . . 173
7.6 Temperature acceptance bandwidth measurement at low DFG power. 175
7.7 Temperature acceptance bandwidth measurements at high DFG power. . . . . 175
7.8 DFG Power scaling . . . . . 178
7.9 DFG efficiency as a function of the product of pump and signal power. . . . . 179
7.10 Simulated DFG power as a function of signal beam waist radius for a fixed pump beam waist radius at maximum input powers. . . 180
7.11 Drop in DFG output power over time. . . . . 181
7.12 Passive power stability of the DFG output. . . . . 182
7.13 Power stability of (a) pump, and (b) signal at maximum input power levels . . . . . 182
7.14 Temperature profiles in the MgO:PPLN crystal caused by local heating due to linear absorption of (a) pump, (b) signal, (c) DFG, and (d) all three interacting beams. . . . . 184
7.15 Spectrum of DFG beam at maximum output power. . . . . 186
7.16 Spectral stability of the generated DFG at maximum output power. 187
7.17 Spectral stability of (a) pump, and (b) signal at maximum input power. . . . . 187
7.18 Spatial beam profile of (a) pump, (b) signal, and (c) DFG at maximum output power. . . . . 188
7.19 Beam pointing stability of DFG at maximum output power. . . . . 189
7.20 Measured beam quality factor of the DFG output . . . . . 189
7.21 Measured beam quality factor of the pump, and signal . . . . . 190

# List of Tables

1.1 Tunable continuous-wave OPOs based on PPKTP. . . . . 6
1.2 Continuous-wave green-pumped OPOs based on MgO:PPLN. . . . 7

2.1 Contracted notations. . . . . 29
2.2 Ray matrices of common optical elements. . . . . 53

3.1 Material properties of PPKTP . . . . . 65

4.1 Material properties of MgO:cPPLT . . . . . 103

5.1 Material properties of MgO:PPLN . . . . . 124

7.1 Mid-IR cw DFG based on bulk MgO:PPLN. . . . . 169

8.1 Green-pumped cw OPOs based on fan-out grating crystals. . . . . 202

# List of Acronyms

| | |
|---|---|
| **AR** | Antireflection |
| **BPM** | Birefringent phase-matching |
| **CPM** | Critical phase-matching |
| **cw** | Continuous-wave |
| **DBC** | Dichroic beam combiner |
| **DFG** | Difference-frequency-generation |
| **DPSS** | Diode-pumped solid-state |
| **DRO** | Doubly-resonant oscillator |
| **DUT** | Device under test |
| **FOM** | Figure-of-merit |
| **FSR** | Free spectral range |
| **FWHM** | Full-width-at-half-maximum |
| **GRIIRA** | Green-induced infrared absorption |
| **IC-SRO** | Intracavity singly-resonant oscillator |
| **IR** | Infrared |
| **LWMIR** | Long-wave mid-infrared |
| **mid-IR** | Mid-infrared |
| **nA** | Nanoamperes |
| **NCPM** | Non-critical phase-matching |
| **near-IR** | Near-Infrared |
| **ns** | Nanosecond |
| **OC** | Output coupler |

| | |
|---|---|
| **OC-SRO** | Output-coupled singly-resonant oscillator |
| **OPG** | Optical parametric generation |
| **OPO** | Optical parametric oscillator |
| **PBS** | Polarizing beam-splitter |
| **PE-SRO** | Pump-enhanced singly-resonant oscillator |
| **ps** | Picosecond |
| **QPM** | Quasi-phase-matching |
| **RT** | Room temperature |
| **SFG** | Sum-frequency-generation |
| **SHG** | Second-harmonic-generation |
| **SRO** | Singly-resonant oscillator |
| **SVEA** | Slowly varying envelope approximation |
| **TRO** | Triply-resonant oscillator |
| **UV** | Ultraviolet |

# 1. Introduction

## 1.1 Background

The advent of laser has led to unprecedented advances in science and technology. From unravelling the behaviour of electrons in atoms to detecting gravitational waves, from drilling holes in metals to etching with nanometre and picometre resolution, lasers are employed across almost all fields of scientific and technological research, and industry. They are also widely used in imaging and surgery, navigation and range finding, satellite and fiber communication, security, and much more. Common everyday applications of lasers include bar code scanners, laser printers, disc players, fiber optic internet modems among others. Continued research and development in the field of lasers has played an invaluable role in improving our understanding of fundamental physics, contributing to 11 Nobel Prizes across physics and chemistry, development of new technologies, and has also made vital contributions to improving our daily life. Since the first demonstration of the working laser in 1960 [1], the laser industry has grown exponentially, with a global market of $ 16.7 Billion in 2020 [2].

The working principle of laser is based on stimulated emission, in which photons stimulate the excited atoms of the laser medium, also known as the gain medium, to radiatively transition to a lower energy level. The emitted photons are at a specific wavelength, corresponding to the energy difference between the energy levels of the atomic transition, and these generated photons are further amplified by means of a resonator. Such photons have identical physical properties, resulting in a coherent unidirectional beam of light. Lasers can deliver output in various time scales, for example the output can be modulated in time, resulting in pulses of light, or be at constant intensity with time, known as continuous-wave (cw). With pulsed lasers, the laser output can be in nanosecond pulses, normally achieved by Q-switching and typically having high pulse energies, or in ultrashort pulses of picosecond or femtosecond duration achieved by mode-locking. The early lasers, and even many of the lasers manufactured today are fixed wavelength devices, because of the discrete transitions in the laser gain media. The development of dye lasers resulted in the first lasers with tunable wavelength output. Later on, the development of Ti:Sapphire laser also exploited its broadband emission spectra to achieve tunable output over a wide wavelength range. A broadband gain spectrum is also required for the generation of ultrashort pulses, which enables study of ultrafast processes such as the behaviour of electrons in atoms and molecules in real time. While such lasers can be continuously tuned over a significant wavelength range, only a certain part of the electromagnetic spectrum is covered in a single device. Moreover, certain regions of the electromagnetic spectrum, spanning from the ultraviolet (UV) to mid-infrared (mid-IR) remain inaccessible to conventional lasers due to lack of suitable gain media.

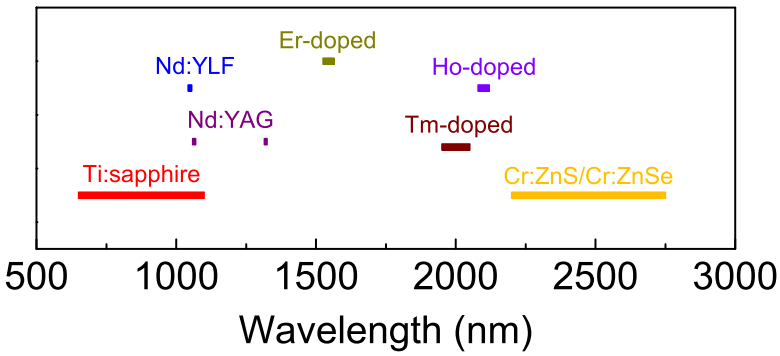


Figure 1.1: Emission wavelengths of some common solid-state lasers.

Coherent tunable sources in the near-infrared (near-IR) and mid-IR are required for applications in spectroscopy, microscopy, imaging and frequency meteorology [3–6]. Many molecules also have their absorption features in these spectral regions, and this is exploited in various applications including security, trace gas detection and environment sensing, food and medical diagnostics. The emission region of some common solid-state lasers is shown in Fig. 1.1. As can be seen, important parts of the spectrum in visible, near-IR and mid-IR are not covered, especially by a single device. Thus, there is a need to develop coherent optical sources to cover these spectral regions, in order to fully realize the potential of laser-based technologies.

Nonlinear optics, in particular nonlinear frequency conversion, is a viable approach to develop tunable coherent sources in spectral regions inaccessible to lasers. The history of nonlinear optics in fact predates the development of the laser. Certain nonlinear optical effects such as the Kerr effect, Pockels effect and the Raman effect were observed in the late 19th and early 20th century [7–9]. The term “nonlinear optics” was coined in the 1942 by Erwin Schrodinger [10].

Nonlinear optics is essentially the study of the nonlinear response of materials to incident electric fields in the optical domain. As will be described in details in chapter 2, very high fields are required to induce nonlinear response in a dielectric medium. Thus the invention of the laser in 1960 enabled the generation of high-intensity electric fields in a controlled laboratory environment, and subsequently led to an explosion in discovering new phenonmena in the field of nonlinear optics. Soon after the development of the laser, the first demonstration of optical nonlinear frequency conversion followed, when the first observation of *second-harmonic-generation* (SHG) was reported in 1961 [11]. This was achieved by focussing a pulsed ruby laser operating at 694.3 nm into a quartz crystal, resulting in the generation of second harmonic output beam at 347.2 nm. Intense phase-matched SHG was demonstrated in 1962 [12, 13]. The first demonstration of *sum-frequency-generation* (SFG) was also published at the same time [14]. The proposal and theoretical framework for *optical parametric generation* (OPG), amplification and oscillation was soon formulated [15–17], followed by a detailed and comprehnsive treatment of interacting waves in a nonlinear dielectric [18]. The first demonstration of *difference-frequency-generation* (DFG) was reported soon after in 1963 [19].

In 1965, parametric gain accompanying DFG was reported [20], which was followed by the first experimental demonstration of an *optical parametric oscillator* (OPO) [21]. This was a pivotal moment, as a single device was now able to generate coherent light with tunable wavelength, and provided access to the spectral regions not accessible by the laser. In this demonstration, the second harmonic of a Nd:$CaWO_4$ laser was used as the pump source, and $LiNbO_3$ as the nonlinear crystal, generating tunable radiation across 970-1150 nm. The first

demonstration of cw OPOs followed a couple of years later [22, 23]. The first synchronously-pumped picosecond OPO was demonstrated in 1977 [24].

The rapid progress made in the 1960s in the field of nonlinear frequency conversion was eventually hindered due to the lack of suitable pump lasers and nonlinear optical materials, inhibiting the development of practical OPOs. This period of stagnation came to an end in the 1980s, with the development of femtosecond lasers [25, 26], and new nonlinear optical materials such as $AgGaS_2$, $AgGaSe_2$ and $\beta$-$BaB_2O_4$ (BBO) [27–29]. The first synchronously pumped femtosecond OPO was demonstrated in 1989 [30], and the first cw *singly-resonant oscillator* (SRO) was demonstrated in 1993 [31]. Both demonstrations were based on the nonlinear material $KTiPO_4$ (KTP). The emergence of electric field poling techniques for domain inversion engineering in ferroelectric nonlinear crystals to develop periodically-poled crystals for *quasi-phase-matching* (QPM) was a major milestone in the field of nonlinear freuquency conversion [32, 33]. It was now possible to use large crystal aperture and long crystal lengths to develop practical devices based on QPM. The first nanosecond and cw OPOs based on periodically-poled $LiNbO_3$ (PPLN) were demonstrated in 1995 [34]. Due to the stringent requirements of the pump laser in the cw regime, such as high output power, single-frequency operation in good beam quality, along with the low nonlinear optical gain available in cw regime, development of high-power cw SROs was not possible until the introduction of PPLN. The first cw SROs based on PPLN were demonstrated in 1996 [35, 36]. Wavelength tuning in a QPM OPO at a fixed temperature was demonstrated by using a fan-out grating structure in 1998 [37].

| Pump (nm) | Configuration | Signal (nm) | Idler (nm) | Signal Power (mW) | Idler Power (mW) | QPM grating period (µm) | Crystal Temperature (°C) | Ref |
|---|---|---|---|---|---|---|---|---|
| 532 | DRO | 1037-1093 | | 6.5 (signal+idler) | | 9 | 32-38 | [39] |
| 532 | DRO | 763.4-769.1 | 1639.2-1665.7 | - | 10 (1650 nm) | 9.55 | 20-55 | [50] |
| 800 | Intracavity SRO | 1140-1270 | 2230-2730 | - | 455 (2470 nm) | 28.5 | 20 (Pump tuning) | [51,52] |
| | | 1180-1260 | 2290-2570 | - | 115 (2350 nm) | | 35-100 | |
| 532 | Pump-enhanced SRO | 865-1032 | 1100-1384 | 28 (946.4 nm) | 72 (1215 nm) | 9 | 37.5-225 | [53] |
| 532 | SRO | 656-1035 | 1096-2830 | 60 | 800 | 8.96-12.194 | RT to 150 | [54] |
| 526.5 | OC-DRO | 791.3-807.5 | 1512.9-1573.4 | 156 (805 nm) | 89 (1522 nm) | 9.68 | 10-90 | [55] |

Table 1.1: Tunable continuous-wave OPOs based on PPKTP.

Green-pumped OPOs are versatile sources for generating tunable coherent radiation from the visible and near-IR to mid-IR. However, green pumping is also challenging, especially in the cw regime, because of the higher residual absorption in the visible in common ferroelectric nonlinear crystals as compared to pumping at ∼1 µm. The advent of QPM led to the possibility of developing high-power cw green-pumped OPOs, with the nonlinear materials of choice being the oxide-based ferroelectric crystals, $LiNbO_3$ (LN), KTP, and $LiTaO_3$ (LT), because of their broad transparency range from the UV to mid-IR, and the ability to be periodically poled. The first cw green-pumped OPO based on PPLN was demonstrated in 1998 [38]. However, the deleterious effects of green-induced infrared absorption (GRIIRA) and photorefraction hampered its further development. KTP, on the other hand, did not suffer from either GRIIRA or photorefraction, and the first green-pumped cw OPO based on peridocally-poled KTP (PPKTP) was also demonstrated in 1998 [39]. A summary of cw tunable OPOs based on PPKTP is given in Table 1.1. A green-pumped cw OPO based on periodically-poled LT (PPLT) was demonstrated in 1999 [40]. It was

| Configuration | Crystal length (mm) | Signal (nm) | Idler (nm) | Signal Power (mW) | Idler Power (mW) | QPM grating period (µm) | Crystal Temperature (˚C) | Ref |
|---|---|---|---|---|---|---|---|---|
| PE-SRO | 40 | 800-920 | 1250-1580 | 5 | 8 (1404 nm) | 7.1-7.6 | 30-100 | [56] |
| SRO | 40 | 840-856 | 1406-1451 | 5 | 310 (1416 nm) | 7.3 | 40-80 | [57] |
| OC-SRO | 40 | 770-890 | 1330-1680 | 100 (885 nm) | 200 (1333 nm) | 7.2-7.8 | 40-100 | [58] |
| SRO | 40 | 885 | 1334 | - | 300 (1334 nm) | 7.2 | 40 | [59] |
| OC-SRO | 50 | 920-1030 | 1100-1260 | 600 (981 nm) | 400 (1163 nm) | 6.92 | 65-135 | [60] |

Table 1.2: Continuous-wave green-pumped OPOs based on MgO:PPLN.

observed that stoichiometric LT (sLT) had a significantly lower susceptibility to GRIIRA and photorefraction [41, 42], and doping with MgO improved material properties in LT and LN [43–46], and green-pumped OPOs based on MgO-doped PPLN (MgO:PPLN) and sPPLT (MgO:sPPLT) [47–49] have been demonstrated. A summary of cw green-pumped OPOs based on MgO:PPLN is given in Table 8.1. Wavelength tuning in all the OPOs listed in Tables 1.1 and 8.1 is primarily carried out by temperature tuning, which is a slow process, as the nonlinear crystal needs to reach thermal equilibrium with each temperature change. Moreover, because of material dispersion properties, large temperature changes are required for small changes in wavelength away from degeneracy. As mentioned above, wavelength tuning at a fixed temperature can be achieved by using a fan-out grating structure. However, fabricating QPM structures for green pumping is more challenging because of the requirements of short grating periods, $\Lambda \leq 10$ µm. With progress in crystal growth and poling technology, it is now possible to fabricate these ferroelectric crystals in a fan-out grating suitable for green pumping, and in this thesis, we have investigated green-pumped cw OPOs

based on fan-out grating PPKTP and MgO:PPLN, for the first time. We have also studied periodically-poled MgO-doped congruent $LiTaO_3$ (MgO:cPPLT) in a green-pumped OPO, for the first time.

As mentioned earlier, the mid-IR spectral range is of great importance, and cw high-power sources are required for a variety of applications from spectroscopy to material processing in the 2-3 µm spectral region. While various sources exist in this spectral range, certain regions and wavelengths are still not accessible in the cw regime in high power, and with good beam quality, such as 2.26 µm. Nonlinear frequency conversion is a viable approach to provide gap-free spectral coverage in this wavelength range. In this thesis, we utilise the progress made in fiber laser technology and combine commercial Yb-fiber and Tm-fiber lasers in MgO:PPLN for the first time, to develop a high power cw source at 2.26 µm based on single-pass DFG.

## 1.2 Thesis structure and overview

The research work done in this thesis is on the development of novel frequency conversion sources encompassing the visible to the mid-IR spectral region. Based on visible, near- and mid-IR OPOs, and mid-IR DFG, the spectral regions are covered in the cw and nanosecond time-scales. One of the OPOs developed in this thesis is also used as the input light source for the device characterization process of sensors for the aerospace sector in an industrial environment. The pump sources used in this work include commercially available diode-pumped solid-state (DPSS) lasers at 532 nm and 1064 nm, and commercially available fiber lasers at 532, 1064 and 2010 nm. Quasi-phase-matched nonlinear crystals

are used for maximum efficiency in the frequency conversion process. Fan-out gratings in MgO:cPPLT, PPKTP and MgO:PPLN are investigated, for the first time, in green-pumped OPOs, while a single grating MgO:PPLN is used for the DFG source. Detailed experimental characterization of each device is performed, and the output characteristics are extensively studied and complimented with theoretical simulations. The work in this thesis is divided into 8 chapters and a brief description of each chapter is given below.

Chapter 2 describes the basic concepts of nonlinear optics, especially second-order nonlinear optics, which forms the basis for three-wave interaction and frequency conversion processes in this thesis. Starting from an introduction to second-order nonlinear susceptibility, the coupled-wave equations are derived using Maxwell's wave equations. Different ways of achieving phase-matching are discussed, followed by the basic concepts required for designing and developing an OPO, including nonlinear material considerations and optical resonator designs.

In Chapter 3, we demonstrate wide wavelength tuning in the near-IR spectral region at room temperature by using a fan-out grating design in PPKTP, for the first time, in a cw OPO. Pumped in the green, the cw SRO has a tuning range spanning more than 800 nm. Resonant signal wave output-coupling to extract useful signal power to increase extraction efficiency is also deployed in a PPKTP cw SRO, for the first time, and the performance is compared with a pure SRO configuration.

Chapter 4 describes the development of the first green-pumped OPO based on the recent nonlinear material, MgO:cPPLT. Using an externally frequency doubled Q-switched DPSS Nd:YAG laser as the pump source, and a fan-out grating MgO:cPPLT as the nonlinear crystal, we demonstrate a nanosecond OPO with

a tuning range of ∼350 nm in the signal, and ∼1350 nm in the idler, encompassing the visible, near- and mid-IR. The results of output power scaling, power stability, beam profile and temporal characteristics are also discussed.

In chapter 5, we develop a rapidly tunable and stable near-IR source by building the first cw green-pumped OPO based on fan-out grating MgO:PPLN. Using a DPSS laser at 532 nm, the OPO is continuously tunable across 813-1032 nm in the signal and 1098-1539 nm in the idler. By optimising the pump focussing condition and deploying output coupling to manage thermal effects, we obtain high-quality output across the tuning range. Characterization of the OPO including output power scaling, power stability, spectral and spatial characteristics are discussed.

Chapter 6 describes the development of a fiber-laser-pumped cw SRO in an industrial environment, performed as a part of an internship at Radiantis. Using a cw green fiber laser as the pump, the near-IR output of the OPO is used as the input light source for a device characterization setup, to test sensors for the aerospace sector. Using the OPO results in orders-of-magnitude improvement in the device characterization process compared to the pre-existing setup. Characterization of the OPO and comparison of the results with the pre-existing setup are discussed.

In chapter 7, we develop a high-power fiber-pumped source of cw mid-IR radiation at 2.26 µm. By combining the outputs of Yb- and Tm-fiber lasers in MgO:PPLN crystal, we obtain high quality multi-watt output. Detailed characterization of the mid-IR source, including temperature acceptance bandwidth, thermal effects, power scaling, power stability, spectral and spatial characteristics are discussed, and compared with theoretical simulations.

In chapter 8, the thesis is concluded by highlighting the key results of this work, together with a discussion on their relevance, and some suggestions for future research directions to advance the field of nonlinear frequency conversion.

# References

[1] T. H. Maiman, "Stimulated Optical Radiation in Ruby," Nature **187**, 493–494 (1960).
http://www.nature.com/articles/187493a0

[2] https://www.laserfocusworld.com/photonics-business/article/14200786/global-laser-markets-in-the-time-of-covid19

[3] K. C. Cossel, E. M. Waxman, I. A. Finneran, G. A. Blake, J. Ye, and N. R. Newbury, "Gas-phase broadband spectroscopy using active sources: progress, status, and applications [Invited]," Journal of the Optical Society of America B **34**, 104 (2017).
https://www.osapublishing.org/abstract.cfm?uri=josab-34-1-104

[4] A. Schliesser, N. Picqué, and T. W. Hänsch, "Mid-infrared frequency combs," Nature Photonics **6**, 440–449 (2012).
http://www.nature.com/articles/nphoton.2012.142

[5] C. W. Freudiger, W. Min, B. G. Saar, S. Lu, G. R. Holtom, C. He, J. C. Tsai, J. X. Kang, and X. S. Xie, "Label-Free Biomedical Imaging with High Sensitivity by Stimulated Raman Scattering Microscopy," Science **322**, 1857–1861 (2008).
http://www.sciencemag.org/lookup/doi/10.1126/science.1165758

[6] S. Junaid, S. Chaitanya Kumar, M. Mathez, M. Hermes, N. Stone, N. Shepherd, M. Ebrahim-Zadeh, P. Tidemand-Lichtenberg, and C. Pedersen, "Video-rate, mid-infrared hyperspectral upconversion imaging," Optica **6**, 702 (2019).
https://www.osapublishing.org/abstract.cfm?uri=optica-6-6-702

[7] R. C. Gray, "The Rev. John Kerr, F.R.S., inventor of the Kerr cell," Nature **136**, 245–247 (1935).
https://www.nature.com/articles/136245a0

[8] F. C. A. Pockels, *Lehrbuch der kristalloptik* (BG Teubner, 1906).
https://openlibrary.org/books/OL6983024M/Lehrbuch_der_Kristalloptik

[9] C. V. Raman and K. S. Krishnan, "A New Type of Secondary Radiation," Nature **121**, 501–502 (1928).
http://www.nature.com/articles/121501c0

[10] E. Schrödinger, "Non-Linear Optics," Proceedings of the Royal Irish Academy. Section A: Mathematical and Physical Sciences **47**, 77–117 (1942).
https://www.jstor.org/stable/20488437

[11] P. A. Franken, A. E. Hill, C. W. Peters, and G. Weinreich, "Generation of optical harmonics," Physical Review Letters **7**, 118–119 (1961).
https://link.aps.org/doi/10.1103/PhysRevLett.7.118

[12] J. A. Giordmaine, "Mixing of light beams in crystals," Physical Review Letters **8**, 19–20 (1962).
https://link.aps.org/doi/10.1103/PhysRevLett.8.19

[13] P. D. Maker, R. W. Terhune, M. Nisenoff, and C. M. Savage, "Effects of dispersion and focusing on the production of optical harmonics," Physical Review Letters **8**, 21–22 (1962).
https://link.aps.org/doi/10.1103/PhysRevLett.8.21

[14] M. Bass, P. A. Franken, A. E. Hill, C. W. Peters, and G. Weinreich, "Optical mixing," Physical Review Letters **8**, 18 (1962).
https://link.aps.org/doi/10.1103/PhysRevLett.8.18

[15] N. M. Kroll, "Parametric Amplification in Spatially Extended Media and Application to the Design of Tuneable Oscillators at Optical Frequencies,"

Physical Review **127**, 1207–1211 (1962).
https://link.aps.org/doi/10.1103/PhysRev.127.1207

[16] R. H. Kingston, "Parametric Amplification and Oscillation at Optical Frequencies," Proceedings of the IRE **50**, 472 (1962).
http://ieeexplore.ieee.org/document/4066665/

[17] S. A. Akhmanov and R. V. Khokhlov, "Concerning one possibility of amplification of light waves," Journal of Experimental and Theoretical Physics (U.S.S.R) **43**, 351–353 (1962).
http://jetp.ras.ru/cgi-bin/e/index/r/43/1/p351?a=list

[18] J. A. Armstrong, N. Bloembergen, J. Ducuing, and P. S. Pershan, "Interactions between light waves in a nonlinear dielectric," Physical Review **127**, 1918–1939 (1962).
https://link.aps.org/doi/10.1103/PhysRev.127.1918

[19] A. W. Smith and N. Braslau, "Observation of an optical difference frequency," Journal of Applied Physics **34**, 2105–2106 (1963).
http://aip.scitation.org/doi/10.1063/1.1729748

[20] C. C. Wang and G. W. Racette, "Measurement of parametric gain accompanying optical difference frequency generation," Applied Physics Letters **6**, 169–171 (1965).
http://aip.scitation.org/doi/10.1063/1.1754219

[21] J. A. Giordmaine and R. C. Miller, "Tunable Coherent Parametric Oscillation in $LiNbO_3$ at Optical Frequencies," Physical Review Letters **14**, 973–976 (1965).
http://link.aps.org/doi/10.1103/PhysRevLett.14.973

[22] R. G. Smith, J. E. Geusic, H. J. Levinstein, J. J. Rubin, S. Singh, and L. G. Van Uitert, "CONTINUOUS OPTICAL PARAMETRIC OSCILLATION in

$Ba_2NaNb_5O_{15}$," Applied Physics Letters **12**, 308–310 (1968).
http://aip.scitation.org/doi/10.1063/1.1652004

[23] R. L. Byer, M. K. Oshman, J. F. Young, and S. E. Harris, "Visible Cw Parametric Oscillator," Applied Physics Letters **13**, 109–111 (1968).
http://aip.scitation.org/doi/10.1063/1.1652520

[24] T. Kushida, Y. Tanaka, and M. Ojima, "Tunable Picosecond Pulse Generation by Optical Parametric Oscillator," Japanese Journal of Applied Physics **16**, 2227–2235 (1977).
https://iopscience.iop.org/article/10.1143/JJAP.16.2227

[25] R. L. Fork, B. I. Greene, and C. V. Shank, "Generation of optical pulses shorter than 0.1 psec by colliding pulse mode locking," Applied Physics Letters **38**, 671–672 (1981).
http://aip.scitation.org/doi/10.1063/1.92500

[26] D. E. Spence, P. N. Kean, and W. Sibbett, "60-fsec pulse generation from a self-mode-locked Ti:sapphire laser," Optics Letters **16**, 42 (1991).
https://www.osapublishing.org/abstract.cfm?uri=ol-16-1-42

[27] Y. X. Fan, R. C. Eckardt, R. L. Byer, R. K. Route, and R. S. Feigelson, "$AgGaS_2$ infrared parametric oscillator," Applied Physics Letters **45**, 313–315 (1984).
http://aip.scitation.org/doi/10.1063/1.95275

[28] L. K. Cheng, W. R. Bosenberg, and C. L. Tang, "Broadly tunable optical parametric oscillation in $\beta$-$BaB_2O_4$," Applied Physics Letters **53**, 175–177 (1988).
http://aip.scitation.org/doi/10.1063/1.100582

[29] R. C. Eckardt, Y. X. Fan, R. L. Byer, C. L. Marquardt, M. E. Storm, and L. Esterowitz, "Broadly tunable infrared parametric oscillator using

$AgGaSe_2$," Applied Physics Letters **49**, 608–610 (1986).
http://aip.scitation.org/doi/10.1063/1.97055

[30] D. C. Edelstein, E. S. Wachman, and C. L. Tang, "Broadly tunable high repetition rate femtosecond optical parametric oscillator," Applied Physics Letters **54**, 1728–1730 (1989).
http://aip.scitation.org/doi/10.1063/1.101272

[31] S. T. Yang, R. C. Eckardt, and R. L. Byer, "Continuous-wave singly resonant optical parametric oscillator pumped by a single-frequency resonantly doubled Nd:YAG laser," Optics Letters **18**, 971 (1993).
https://www.osapublishing.org/abstract.cfm?uri=ol-18-12-971

[32] M. Yamada, N. Nada, M. Saitoh, and K. Watanabe, "First-order quasi-phase matched $LiNbO_3$ waveguide periodically poled by applying an external field for efficient blue second-harmonic generation," Applied Physics Letters **62**, 435–436 (1993).
http://aip.scitation.org/doi/10.1063/1.108925

[33] M. Fejer, G. Magel, D. Jundt, and R. Byer, "Quasi-phase-matched second harmonic generation: tuning and tolerances," IEEE Journal of Quantum Electronics **28**, 2631–2654 (1992).
http://ieeexplore.ieee.org/document/161322/

[34] L. E. Myers, R. C. Eckardt, M. M. Fejer, R. L. Byer, W. R. Bosenberg, and J. W. Pierce, "Quasi-phase-matched optical parametric oscillators in bulk periodically poled $LiNbO_3$," Journal of the Optical Society of America B **12**, 2102 (1995).
https://www.osapublishing.org/abstract.cfm?uri=josab-12-11-2102

[35] W. R. Bosenberg, L. E. Myers, R. L. Byer, A. Drobshoff, and J. I. Alexander, "Continuous-wave singly resonant optical parametric oscillator based

on periodically poled $LiNbO_3$," Optics Letters **21**, 713 (1996).
https://www.osapublishing.org/abstract.cfm?uri=ol-21-10-713

[36] W. R. Bosenberg, L. E. Myers, R. L. Byer, A. Drobshoff, and J. I. Alexander, "93% pump depletion, 3.5-W continuous-wave, singly resonant optical parametric oscillator," Optics Letters **21**, 1336 (1996).
https://www.osapublishing.org/abstract.cfm?uri=ol-21-17-1336

[37] P. E. Powers, T. J. Kulp, and S. E. Bisson, "Continuous tuning of a continuous-wave periodically poled lithium niobate optical parametric oscillator by use of a fan-out grating design," Optics Letters **23**, 159 (1998).
https://www.osapublishing.org/abstract.cfm?uri=ol-23-3-159

[38] R. G. Batchko, D. R. Weise, T. Plettner, G. D. Miller, M. M. Fejer, and R. L. Byer, "Continuous-wave 532-nm-pumped singly resonant optical parametric oscillator based on periodically poled lithium niobate," Optics Letters **23**, 168 (1998).
https://www.osapublishing.org/abstract.cfm?uri=ol-23-3-168

[39] A. Garashi, A. Arie, A. Skliar, and G. Rosenman, "Continuous-wave optical parametric oscillator based on periodically poled $KTiOPO_4$," Optics Letters **23**, 1739 (1998).
https://www.osapublishing.org/abstract.cfm?uri=ol-23-22-1739

[40] U. Strö$\beta$ner, A. Peters, J. Mlynek, S. Schiller, J.-P. Meyn, and R. Wallenstein, "Single-frequency continuous-wave radiation from 0.77 to 1.73 µm generated by a green-pumped optical parametric oscillator with periodically poled $LiTaO_3$," Optics Letters **24**, 1602 (1999).
http://www.opticsinfobase.org/abstract.cfm?uri=ol-24-22-1602

[41] A. L. Alexandrovski, G. Foulon, L. E. Myers, R. K. Route, and M. M. Fejer, "UV and visible absorption in $LiTaO_3$," **112**, 44 (1999).
http://proceedings.spiedigitallibrary.org/proceeding.aspx?doi=10.1117/12.349242

[42] M. Katz, R. K. Route, D. S. Hum, K. R. Parameswaran, G. D. Miller, and M. M. Fejer, "Vapor-transport equilibrated near-stoichiometric lithium tantalate for frequency-conversion applications." Optics letters **29**, 1775–7 (2004).
https://www.osapublishing.org/abstract.cfm?uri=ol-29-15-1775

[43] D. A. Bryan, R. Gerson, and H. E. Tomaschke, "Increased optical damage resistance in lithium niobate," Applied Physics Letters **44**, 847–849 (1984).
http://aip.scitation.org/doi/10.1063/1.94946

[44] Y. Furukawa, K. Kitamura, A. Alexandrovski, R. K. Route, M. M. Fejer, and G. Foulon, "Green-induced infrared absorption in MgO doped $LiNbO_3$," Applied Physics Letters **78**, 1970–1972 (2001).
http://aip.scitation.org/doi/10.1063/1.1359137

[45] A. G. Getman, S. V. Popov, and J. R. Taylor, "7 W average power, high-beam-quality green generation in MgO-doped stoichiometric periodically poled lithium tantalate," Applied Physics Letters **85**, 3026–3028 (2004).
http://aip.scitation.org/doi/10.1063/1.1806538

[46] J. Hirohashi, T. Tago, O. Nakamura, A. Miyamoto, and Y. Furukawa, "Characterization of GRIIRA properties in $LiNbO_3$ and $LiTaO_3$ with different compositions and doping," in *Nonlinear Frequency Generation and Conversion: Materials, Devices, and Applications VII*, P. E. Powers, ed., **6875**, 687 516 (2008).
http://proceedings.spiedigitallibrary.org/proceeding.aspx?doi=10.1117/12.773742

[47] G. K. Samanta, G. R. Fayaz, Z. Sun, and M. Ebrahim-Zadeh, "High-power, continuous-wave, singly resonant optical parametric oscillator based on MgO:sPPLT," Optics Letters **32**, 400 (2007).
https://www.osapublishing.org/abstract.cfm?uri=ol-32-4-400

[48] G. K. Samanta, G. R. Fayaz, and M. Ebrahim-Zadeh, "1.59 W, single-frequency, continuous-wave optical parametric oscillator based on MgO:sPPLT," Optics Letters **32**, 2623 (2007).
https://www.osapublishing.org/abstract.cfm?uri=ol-32-17-2623

[49] K. Devi and M. Ebrahim-Zadeh, "Room-temperature, rapidly tunable, green-pumped continuous-wave optical parametric oscillator," Optics Letters **42**, 2635 (2017).
https://www.osapublishing.org/abstract.cfm?uri=ol-42-13-2635

[50] G. M. Gibson, M. Ebrahimzadeh, M. J. Padgett, and M. H. Dunn, "Continuous-wave optical parametric oscillator based on periodically poled $KTiOPO_4$ and its application to spectroscopy," Optics Letters **24**, 397–399 (1999).
http://www.osapublishing.org/abstract.cfm?uri=ol-24-6-397

[51] M. Ebrahimzadeh, G. A. Turnbull, T. J. Edwards, D. J. M. Stothard, I. D. Lindsay, and M. H. Dunn, "Intracavity continuous-wave singly resonant optical parametric oscillators," Journal of the Optical Society of America B **16**, 1499 (1999).
https://www.osapublishing.org/abstract.cfm?uri=josab-16-9-1499

[52] T. Edwards, G. Turnbull, M. Dunn, and M. Ebrahimzadeh, "Continuous-wave, singly-resonant, optical parametric oscillator based on periodically poled $KTiOPO_4$," Optics Express **6**, 58 (2000).
http://www.osapublishing.org/oe/abstract.cfm?uri=oe-6-3-58

[53] D. R. Weise, U. Strößner, A. Peters, J. Mlynek, S. Schiller, A. Arie, A. Skliar, and G. Rosenman, "Continuous-wave 532-nm-pumped singly resonant optical parametric oscillator with periodically poled $KTiOPO_4$," Optics Communications **184**, 329–333 (2000).
https://linkinghub.elsevier.com/retrieve/pii/S0030401800009500

[54] U. Ströβner, J.-P. Meyn, R. Wallenstein, P. Urenski, A. Arie, G. Rosenman, J. Mlynek, S. Schiller, and A. Peters, "Single-frequency continuous-wave optical parametric oscillator system with an ultrawide tuning range of 550 to 2830 nm," Journal of the Optical Society of America B **19**, 1419 (2002).
https://www.osapublishing.org/abstract.cfm?uri=josab-19-6-1419

[55] C. Liu, X. Guo, Z. Bai, X. Wang, and Y. Li, "High-efficiency continuously tunable single-frequency doubly resonant optical parametric oscillator," Applied Optics **50**, 1477 (2011).
https://www.osapublishing.org/abstract.cfm?uri=ao-50-10-1477

[56] D.-H. Lee, S. K. Kim, S.-N. Park, H. Su Park, J. Y. Lee, and S.-K. Choi, "Continuous-wave 532 nm pumped MgO:PPLN optical parametric oscillator with external power regulation and spatial mode filtering," Applied Optics **48**, 37 (2009).
https://www.osapublishing.org/abstract.cfm?uri=ao-48-1-37

[57] S. Zaske, D.-H. Lee, and C. Becher, "Green-pumped cw singly resonant optical parametric oscillator based on MgO:PPLN with frequency stabilization to an atomic resonance," Applied Physics B **98**, 729–735 (2010).
http://link.springer.com/10.1007/s00340-009-3871-7

[58] I.-H. Bae, H. S. Moon, S. Zaske, C. Becher, S. K. Kim, S.-N. Park, and D.-H. Lee, "Low-threshold singly-resonant continuous-wave optical parametric oscillator based on MgO-doped PPLN," Applied Physics B **103**, 311–319

(2011).
http://link.springer.com/10.1007/s00340-010-4297-y

[59] I.-H. Bae, H.-S. Moon, S.-K. Kim, S.-N. Park, and D.-H. Lee, "Self-guided operation of singly resonant continuous-wave optical parametric oscillator based on bulk MgO-doped PPLN," Applied Physics B **106**, 797–801 (2012).
http://link.springer.com/10.1007/s00340-012-4922-z

[60] P. Groß, I. D. Lindsay, C. J. Lee, M. Nittmann, T. Bauer, J. Bartschke, U. Warring, A. Fischer, A. Kellerbauer, and K.-J. Boller, "Frequency control of a 1163 nm singly resonant OPO based on MgO:PPLN," Optics Letters **35**, 820 (2010).
https://www.osapublishing.org/abstract.cfm?uri=ol-35-6-820

# 2. Basics of nonlinear optics

## 2.1 Linear and nonlinear optics

Light is an electromagnetic wave, and optics is the study of light, and its interaction with matter. Everyday effects of light that we observe such as reflection, refraction, and scattering come under the domain of linear optics, where the response of the system is linear with respect to the incident electromagnetic field. For a low-intensity light beam propagating through a transparent medium, the induced polarization $\mathbf{P}$ is linear to the incident electric field $\mathbf{E}$ and is given by

$$\mathbf{P}^{\mathrm{L}} = \epsilon_0 \chi^{(1)} \mathbf{E} \tag{2.1}$$

where $\epsilon_0$ is the permittivity of free space and $\chi^{(1)}$ is the linear electric susceptibility of the medium. In general, $\chi$ is a tensor with components dependent on the frequency $\omega$ and material properties, and $\mathbf{P}$ and $\mathbf{E}$ are vector quantities.

## 2.2 Optical nonlinearity

When the intensity of the input light is high, comparable to the intra-atomic electric field, the response is no longer linear. The induced polarization acquires a nonlinear dependence and can be expressed as a power series in electric field [1]

$$\mathbf{P} = \epsilon_0 \left[ \chi^{(1)} \cdot \mathbf{E} + \chi^{(2)} : \mathbf{EE} + \chi^{(3)} \vdots \mathbf{EEE} + \cdots \right] \tag{2.2}$$

$$\mathbf{P} = \mathbf{P}^{\mathrm{L}} + \mathbf{P}^{\mathrm{NL}} \tag{2.3}$$

where $\mathbf{P}^{\mathrm{L}} = \epsilon_0 \chi^{(1)} \mathbf{E}$ is the linear polarization, $\chi^{(2)}$ and $\chi^{(3)}$ are the second- and third-order nonlinear susceptibility tensors, respectively. The linear polarization oscillates with the frequency of the input wave, whereas the higher-order terms are responsible for the generation of new oscillation frequencies [2] . This exciting phenomenon, however, requires strong input electric fields, the generation of which was not possible until the invention of the laser. The advent of laser led to the generation of unprecedented optical intensities, propelling the field of nonlinear optics, which until then was poorly understood. Major breakthroughs have taken place and significant advances have been made in this field in the last few decades, and it continues to be one of the frontiers of research in physics, optics, and photonics. The work presented in this thesis is based on second-order nonlinear processes, and hence the discussion will be limited to processes involving second-order nonlinear susceptibility $\chi^{(2)}$. A good discussion on nonlinear optical processes can be found in [3–5].

## 2.3 Second-order nonlinear processes

In the nonlinear regime it is possible for electromagnetic waves of equal or different frequencies to interact with each other while propagating through a medium. If the order of nonlinear interaction is given by $n$, then the number of interacting waves is $n+1$, thus implying that second-order nonlinear processes involve three waves. Consider an electric field having two distinct frequency components at $\omega_1$ and $\omega_2$

$$\mathbf{E}(t) = \mathbf{E}_1 e^{-i\omega_1 t} + \mathbf{E}_2 e^{-i\omega_2 t} + c.c. \tag{2.4}$$

where *c.c.* denotes the complex conjugate to account for the reality of the fields, and the amplitudes are $E_1$ and $E_2$ at frequencies $\omega_1$ and $\omega_2$, respectively. The second-order polarization term, given by the second term of equation (2.2) is

$$\mathbf{P}^{\mathrm{NL}} = \epsilon_0 \chi^{(2)} \mathbf{E}^2 \tag{2.5}$$

Substituting equation (2.4) into equation (2.5), we find that the second-order nonlinear polarization can be expressed as a sum of frequency components

$$\begin{aligned} P^{\mathrm{NL}} &= \sum_n P(\omega_n) e^{-i\omega_n t} \\ &= \epsilon_0 \chi^{(2)} \Big[ E_1^2 e^{-2i\omega_1 t} + E_2^2 e^{-2i\omega_2 t} + 2E_1 E_2 e^{-i(\omega_1+\omega_2)t} \\ &+ 2E_1 E_2^* e^{-i(\omega_1-\omega_2)t} + c.c. \Big] + 2\epsilon_0 \chi^{(2)} \Big[ E_1 E_1^* + E_2 E_2^* \Big] \end{aligned} \tag{2.6}$$

The exponents of first two terms are proportional to twice of the input frequency, representing the phenomenon of second-harmonic-generation (SHG), while the

third and fourth term are proportional to the sum and difference of the input frequencies respectively, representing the the process of sum-frequency-generation (SFG) and difference-frequency-generation (DFG), respectively. The last term corresponds to *optical rectification*. In SHG, two photons at frequency $\omega$ combine to produce a single photon at frequency $2\omega$, while in DFG two photons at $\omega_1$ and $\omega_2$ combine to generate a photon at frequency $\omega_3 = \omega_1 - \omega_2$. In SFG, two photons at $\omega_1$ and $\omega_2$ combine to generate a third photon at frequency $\omega_3 = \omega_1 + \omega_2$. SHG is the degenerate case of SFG, where the two input photons are at the same frequency. These processes are shown in Fig. 2.1 (a)-(c), where it should be noted that energy is conserved in each process. Along with energy conservation, momentum is also conserved, and the two conservation laws can be expressed as

$$\omega_3 = \omega_2 + \omega_1 \tag{2.7}$$

$$k_3 = k_2 + k_1 \tag{2.8}$$

where $k_i = n(\omega_i)\omega_i/c$ are the respective wave wectors, and $n(\omega)$ is the refractive index at frequency $\omega$. Equation (2.8) is referred to as the *phase-matching* condition and will be explained in section 2.6. Another process that can take place, which is analytically identical to DFG, is that a photon at $\omega_3$ called the *pump*, generates two photons at frequencies $\omega_1$ and $\omega_2$. This process, shown in Fig. 2.1 (d), is known as *spontaneous parametric down-conversion, parametric fluorescence*, or optical parametric generation (OPG). Of the two generated photons, the one with a shorter wavelength (higher frequency) is called the *signal* and the one with the longer wavelength (lower frequency) is called the *idler*, by convention. As the initial and final quantum states are identical, it is a paramet-

ric process [4]. For a low-intensity laser beam, OPG is very inefficient and only a negligible amount of parametric fluorescence is generated. However, placing the nonlinear material inside an optical cavity to resonate either one or both of the generated fields can greatly enhance the fluorescence intensity such that a large number of input photons are converted into signal and idler photons. This configuration, shown in Fig. 2.1 (e), is known as an optical parametric oscillator (OPO), and provides an efficient method of producing tunable new frequencies from a single input beam [1].

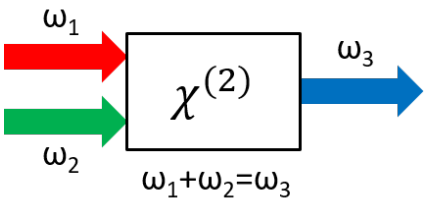


(a) Sum-frequency-generation

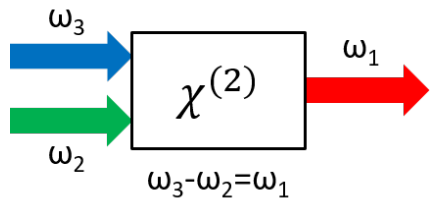


(b) Difference-frequency-generation

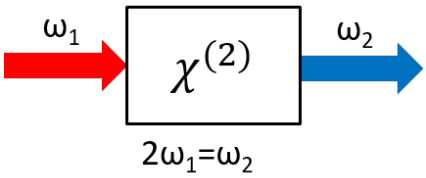


(c) Second harmonic generation

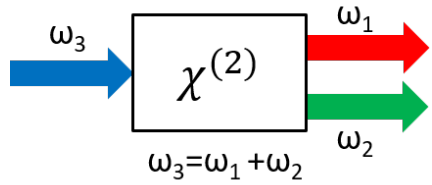


(d) Optical parametric generation

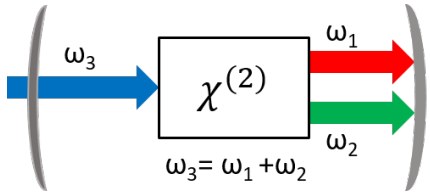


(e) Optical parametric oscillator

Figure 2.1: Second-order nonlinear frequency conversion processes.

## 2.4 Second-order nonlinear susceptibility

The second-order nonlinear susceptibility $\chi^{(2)}$ is a tensor of rank two, and thus has 27 elements. Explicitly written, $\chi^{(2)} = \chi^{(2)}_{ijk}$, where the indices $i, j, k$ can take the values 1, 2, 3, corresponding to $x$, $y$, $z$, and represent the polarization direction. The nonlinear polarization, equation (2.5), can be written in the most general form as [4]

$$P_i(\omega_n + \omega_m) = \epsilon_0 \sum_{jk} \sum_{(nm)} \chi^{(2)}_{ijk}(\omega_n + \omega_m, \omega_n, \omega_m) E_j(\omega_n) E_k(\omega_m) \tag{2.9}$$

where $(nm)$ implies that while carrying the sum over $n$ and $m$, the sum of $\omega_n + \omega_m$ should be fixed. It is a common practice in nonlinear optics to use the $d$-matrix notation instead of the susceptibility tensor, defined as

$$d_{ijk} = \frac{1}{2}\chi_{ijk} \tag{2.10}$$

Often, nonlinear optical interactions involve optical waves whose frequencies are much smaller than the lowest resonance frequency of the material system. A consequence of this is that the nonlinear suscpetibility is essentially independent of frequency. As the frequencies are within the transparency range of the medium, and hence the medium is essentially lossless, the conditions of full permutation symmetry, which states that indices of $\chi^{(2)}_{ijk}(\omega_3 = \omega_1 + \omega_2)$ can be permuted as long as the corresponding frequencies are permuted simultaneously, is valid. But as $\chi^{(2)}$ does not depend on frequency, the indices of $\chi^{(2)}_{ijk}$ can be freely permuted. This result is known as the Kleinman symmetry [4, 6].

Using the Kleinman symmetry condition, the 27 element $\chi^{(2)}$ tensor can be reduced to a $3 \times 6$ matrix using the notations given in Table 2.1. The matrix elements $d_{il}$ are known as the nonlinear coefficients of the material. For two in-

| jk | 11 | 22 | 33 | 23, 32 | 31, 13 | 12, 21 |
|---|---|---|---|---|---|---|
| l | 1 | 2 | 3 | 4 | 5 | 6 |

Table 2.1: Contracted notations.

put frequencies at $\omega_1$ and $\omega_2$ combining to produce a polarization at $\omega_3$, by using the intrinsic permutation symmetry and contracted notations, equation (2.9) can be written as

$$\begin{bmatrix} P_x(\omega_3) \\ P_y(\omega_3) \\ P_y(\omega_3) \end{bmatrix} = 2\epsilon_0 K \begin{bmatrix} d_{11} & d_{12} & d_{13} & d_{14} & d_{15} & d_{16} \\ d_{21} & d_{22} & d_{23} & d_{24} & d_{25} & d_{26} \\ d_{31} & d_{32} & d_{33} & d_{34} & d_{35} & d_{36} \end{bmatrix} \begin{bmatrix} E_x(\omega_1)E_x(\omega_2) \\ E_y(\omega_1)E_y(\omega_2) \\ E_z(\omega_1)E_z(\omega_2) \\ E_y(\omega_1)E_z(\omega_2) + E_z(\omega_1)E_y(\omega_2) \\ E_x(\omega_1)E_z(\omega_2) + E_z(\omega_1)E_x(\omega_2) \\ E_x(\omega_1)E_y(\omega_2) + E_y(\omega_1)E_x(\omega_2) \end{bmatrix} \tag{2.11}$$

where $K$ is the degeneracy factor, taking the value 2 for SFG, DFG and OPG and 1 for degenerate cases such as SHG and optical rectification. Out of the 18 elements in the $d$-matrix, only 10 are independent because of the Kleinmann

symmetry condition. Another important symmetry condition is gemoetrical symmetry, which arises from the structural or the spatial symmetry of the material. Depending on the crystal class, structural symmetry can further reduce the number of independent nonlinear coefficients. For example, lithium niobate ($LiNbO_3$), a negative uniaxial bireffringent crystal belonging to point group $3m$ has only 3 independent elements in its $d_{il}$ matrix and is given by [4]

$$d_{il} = \begin{bmatrix} 0 & 0 & 0 & 0 & d_{31} & -d_{22} \\ -d_{22} & d_{22} & 0 & d_{31} & 0 & 0 \\ d_{31} & d_{31} & d_{33} & 0 & 0 & 0 \end{bmatrix}$$

For a material that possesses inversion symmetry, i.e is centrosymmetric, all second-order nonlinear coefficients must vanish altogether. From equation (2.5), we have

$$\mathbf{P}^{\mathrm{NL}} = \epsilon_0 \chi^{(2)} \mathbf{E}^2 \tag{2.12}$$

If the material possesses inversion symmetry, then if the sign of the applied electric field is changed, the sign of the induced polarization must also change, which gives us

$$-\mathbf{P}^{\mathrm{NL}} = \epsilon_0 \chi^{(2)} [-\mathbf{E}]^2 = \epsilon_0 \chi^{(2)} \mathbf{E}^2 \tag{2.13}$$

Comparing equation (2.12) and (2.13), we see that $\mathbf{P}^{\mathrm{NL}}$ must be equal to $-\mathbf{P}^{\mathrm{NL}}$, which can happen only if $\mathbf{P}^{\mathrm{NL}}$ identically vanishes. This results in

$$\chi^{(2)} = 0 \tag{2.14}$$

for centrosymmetric materials. Therefore, all second-order nonlinear optical ef-

fects are excluded in centrosymmetric materials, which include gases, liquids, glasses and many crystal classes.

## 2.5 Coupled wave equations in nonlinear optics

The previous section dealt with the nonlinear response of a medium to an incident electromagnetic wave, which in turn can result in generation of new frequencies. Maxwell's wave equations can be used to explore the energy flow between all electric field components at different frequencies. Using some simple approximations such as there being no free charges in the region of interest ($\rho = 0$), no free currents ($\mathbf{J} = 0$), the material is non magnetic, and lossless ($\mathbf{B} = \mu_o \mathbf{H}$), the Maxwell's equations can be expressed as

$$\nabla \cdot \mathbf{D} = 0 \tag{2.15}$$

$$\nabla \cdot \mathbf{H} = 0 \tag{2.16}$$

$$\nabla \times \mathbf{D} = -\mu_o \frac{\partial \mathbf{H}}{\partial t} \tag{2.17}$$

$$\nabla \times \mathbf{H} = \frac{\partial \mathbf{D}}{\partial t} \tag{2.18}$$

where $\mathbf{D}$ is the electric displacement field, given by $\mathbf{D} = \epsilon_0 \mathbf{E} + \mathbf{P}$. Taking the curl of equation (2.17) and using equation (2.18) in it, followed by using a suitable vector identity and assuming that $\mathbf{E}$ is of the form of a transverse infinite plane wave, we obtain a wave equation describing the evolution of the electric field in the medium generated by the driving polarization as

$$\nabla^2 \mathbf{E} - \frac{1}{c^2} \frac{\partial^2 \mathbf{E}}{\partial t^2} = \frac{1}{\epsilon_0 c^2} \frac{\partial^2 \mathbf{P}}{\partial t^2} \tag{2.19}$$

Using equation (2.3), and assuming a lossless isotropic material, equation (2.19) can be further simplified into [4]

$$\nabla^2\mathbf{E} - \frac{\epsilon^{(1)}}{c^2}\frac{\partial^2\mathbf{E}}{\partial t^2} = \frac{1}{\epsilon_0 c^2}\frac{\partial^2\mathbf{P}^{\mathrm{NL}}}{\partial t^2} \tag{2.20}$$

where $\epsilon^{(1)}$ is the relative permittivity of the material. We assume that the total electric field consists of three waves propagating along the $z$-axis, and each has the form

$$E_i = A_i(z)e^{(\omega_i t - k_i z)} + c.c. \tag{2.21}$$

where $i = 1, 2, 3$ represent the three fields, $\omega_i$ is the corresponding frequency, and $k_i$ is the wave number,

$$k_i = \frac{n(\omega_i)\omega_i}{c} \tag{2.22}$$

The nonlinear polarization takes the form

$$P_i = P_i(z, \omega_i)e^{(\omega_i t - k_i z)} + c.c. \tag{2.23}$$

Since the waves at three different frequencies are exchanging energy through the second-order nonlinear optical process as they propagate through the medium, their respective amplitudes in general will vary with position, and hence have been considered as functions of the propagation direction $z$. We also assume that the change in the amplitude is very small over a distance comparable to the wavelength, and thus can use the *slowly varying envelope approximation* (SVEA)

$$\left|\frac{d^2A_i}{dz^2}\right| \ll \left|k_i\frac{dA_i}{dz}\right| \tag{2.24}$$

Substituting equations (2.21) and (2.23) in (2.20), using (2.11) for the amplitudes of the polarization in terms of electric field amplitudes, and using SVEA, equation (2.24), results in three coupled amplitude equations for each interacting wave [4]

$$\frac{dA_1}{dz} = \frac{2id_{\text{eff}}\omega_1^2}{k_1c^2}A_3A_2^*e^{i\Delta kz} \tag{2.25}$$

$$\frac{dA_2}{dz} = \frac{2id_{\text{eff}}\omega_2^2}{k_2c^2}A_3A_1^*e^{i\Delta kz} \tag{2.26}$$

$$\frac{dA_3}{dz} = \frac{2id_{\text{eff}}\omega_3^2}{k_1c^2}A_1A_2e^{-i\Delta kz} \tag{2.27}$$

where $d_{\text{eff}}$ is the effective nonlinear coefficient, and

$$\Delta k = k_3 - k_2 - k_1 \tag{2.28}$$

is the phase-mismatch. The work done in this thesis is concerned with the OPG and DFG processes, and $\omega_3, \omega_2, \omega_1$ represent the pump, signal and idler frequencies, respectively, with $\omega_3 = \omega_1 + \omega_2$. The phase-mismatch $\Delta k$ is very important as it dictates the conversion efficiency and direction of energy flow between the waves. For $\Delta k = 0$, a condition known as *perfect phase-matching*, the amplitude (intensity) of a given wave increases linearly (quadratically) with $z$ if the other two amplitudes are constant. Physically, perfect phase-matching implies that the oscillating dipoles at the corresponding frequency are properly phased so that the field emitted by each oscillating dipole adds up coherently in the forward direction. For the case of $\Delta k \neq 0$, the spatial evolution of the amplitude $A_1(z)$ has to be considered. The amplitude at the exit plane of the nonlinear crystal of length $L$ can be obtained by integrating equation (2.25) over the crystal length, assuming that $A_2$ and $A_3$ are constant, which is a valid approximation for small

fields. The result can be expressed in terms of intensities as [4]

$$I_1 = \frac{8d_{\text{eff}}^2\omega_1^2 I_2 I_3}{n_1 n_2 n_3 \epsilon_0 c^2} L^2 \text{sinc}^2\left(\frac{\Delta k L}{2}\right) \tag{2.29}$$

where $I_i = 2n_i\epsilon_0 c\left|A_i^2\right|$. From equation (2.29), we can see that the output intensity will oscillate as a function of $\Delta kL$. For a fixed $\Delta k$, the intensity will continue to grow up to a distance defined as the coherent length $L_c$, beyond which the waves can go out of phase with the driving polarization, resulting in continuous forward and backward flow of energy between the interacting waves as they drift in and out of phase. The coherent length $L_c$ is defined as

$$L_c = \frac{2\pi}{\Delta k} \tag{2.30}$$

This is the maximum useful crystal length for the nonlinear process in presence of phase-mismatch. Phase-matching is essential for generation of useful output from a nonlinear process and the next section will discuss different ways of achieving phase-matching.

## 2.6 Phase-matching

Materials that are transparent in the range of frequencies of interest and used for the nonlinear process have normal dispersion, where the refractive index increases monotonically with the frequency (i.e. $n_3 > n_2 \geq n_1$ for $\omega_3 > \omega_2 \geq \omega_1$). Using equation (2.28), the condition of perfect phase-matching, $\Delta k = 0$ for three waves

with $\omega_3 = \omega_1 + \omega_2$, can be expressed as

$$\frac{n_3\omega_3}{c} = \frac{n_1\omega_1}{c} + \frac{n_2\omega_2}{c} \tag{2.31}$$

Because of normal dispersion, waves at different frequencies travel with different phase velocities, and the condition of perfect phase-matching cannot be achieved in general. However, there are methods through which phase-matching can be achieved, and the two most common ways will be described here. The first method uses the birefringence displayed by many crystals, and is called *birefringent phase-matching* (BPM). The second method, which is used in the work done in this thesis, is to periodically invert the sign of the effective nonlinear coefficient ($d_{\text{eff}}$) to compensate for the non-zero wave vector mismatch. This technique is called *quasi-phase-matching* (QPM).

Since energy is automatically conserved in a parametric process, the set of signal and idler wavelengths that will be generated from a given pump are those that can satisfy the phase-matching condition $\Delta k = 0$. If a physical parameter such as the temperature of the crystal is changed, resulting in the change of refractive indices, the generated signal and idler wavelength will also change in order to be phase-matched under the new condition. This results in the ability to tune the output wavelength and is used in the optical parametric process to generate coherent tunable radiation over a wide spectral range.

### 2.6.1 Birefringent phase-matching

Birefringence is the dependence of the refractive index on the direction of polarization of the optical radiation, expressed generally as $n_x \neq n_y \neq n_z$ in terms

of the three orthogonal axes. If the refractive index is equal in two directions $n_x = n_y \neq n_z$, the the material is said to be *uniaxial*, with $z$ axis known as the *optic axis*. In this case, light polarized perpendicular to the plane containing the propagation vector $\mathbf{k}$ and the optic axis will experience the same refractive index, called *ordinary* refractive index ($\bar{n}_o$), irrespective of the direction of propagation, and the polarization is called the ordinary polarization. The polarization orthogonal to ordinary polarization is called *extraordinary* polarization, and light polarized in the plane containing the propagation vector $\mathbf{k}$ and the optic axis experiences extraordinary refractive index ($n_e(\theta)$), which depends on the angle $\theta$ between the optic axis and the propagation vector $\mathbf{k}$ as

$$\frac{1}{n_e(\theta)^2} = \frac{\sin^2(\theta)}{\bar{n}_e^2} + \frac{\cos^2(\theta)}{\bar{n}_o^2} \tag{2.32}$$

where $\bar{n}_o$ is the ordinary refractive index, and $\bar{n}_e$ is the principal value of $n_e$, $\bar{n}_e = n_e(\theta = 90)$. By choosing the polarization of one or more of the interacting beams such that they experience $n_e(\theta)$, then the angle $\theta$ can be adjusted until phase-matching is achieved, as shown in Fig. 2.2. A drawback of BPM is that whenever the angle $\theta$ has value other than $0^\circ$ or $90^\circ$, the direction of the energy flow, given by the Poynting vector $\mathbf{S}$ is not parallel to the propagation vector $\mathbf{k}$ for extraordinary rays, a phenomenon known as the Poynting vector walk-off. As a result, ordinary and extraordinary polarized light with parallel propagation vectors diverge from each other as they propagate through the crystal, thus limiting the spatial overlap and hence decreasing the efficiency of the nonlinear process involving the waves.

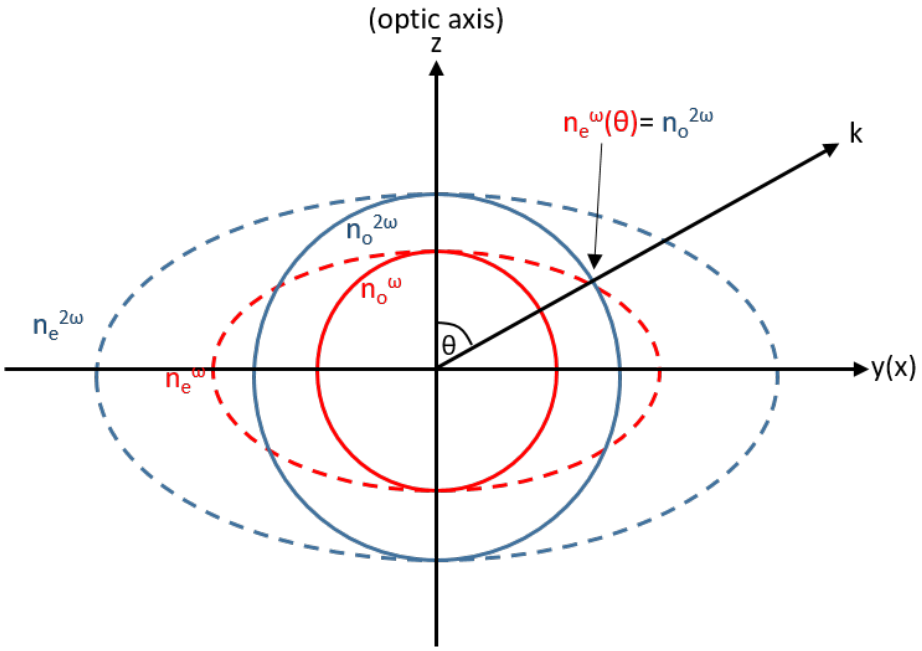


Figure 2.2: Birefringent phase-matching in a uniaxial crystal.

The walk-off angle $\rho$ can be calculated from [5]

$$\tan\rho = -\frac{1}{2}\left|n_e(\theta)\right|^2\left(\frac{1}{n_e^2}-\frac{1}{n_o^2}\right)\sin(2\theta) \tag{2.33}$$

As can be noted, the walk-off angle vanishes for $\theta$=0° or 90°, a case known as *non-critical phase-matching* (NCPM), as approximate phase-matching can be sustained over larger deviations from the precise angle. For $0 < \theta < 90$, this case is known as *critical phase-matching* (CPM). Using the walk-off angle $\rho$, the effective interaction length, or aperture length $l_a$ can be defined as

$$l_a = \frac{\sqrt{\pi}w_0}{\rho} \tag{2.34}$$

where $w_0$ is the beam waist radius at the focus in the crystal. From equation (2.34), it can be seen that for a larger interaction length, the beam waist should be larger. However, nonlinear optical processes require high intensity, and hence small beam waists. Therefore a balance between the two is necessary to achieve practical gain. For NCPM, since there is no walk-off, it ensures complete spatial overlap over the entire length of the crystal. Another drawback of BPM is the inflexibility in the choice of polarizations of the interacting waves, leading to a $d_{\text{eff}}$ which can be lower than the theoretical maximum, thus increasing the threshold for the parametric process. Furthermore, many materials may posses insufficient birefringence to compensate for dispersion over the wavelength range of interest. These issues can be overcome by using QPM, which will be explained in the next section.

### 2.6.2 Quasi-phase-matching

Another way of achieving phase-matching is to apply a phase shift whenever the fields start going out of phase to restore phase-matching. This can be done by periodically inverting the sign of the nonlinear coefficient $d_{\text{eff}}$, to compensate for the wave vector mismatch [3, 7], as shown in Fig. 2.3(a). By inverting the sign of $d_{\text{eff}}$ every coherent length $L_c$, each time the field amplitude of the generated wave(s) is about to decrease due to the wavevector mismatch, the reversal of the sign of $d_{\text{eff}}$ ensures that the amplitudes continue to grow monotonically, as can be seen from the coupled wave equations (2.25)-(2.27). The largest element of the nonlinear susceptibility tensor is often a diagonal element $d_{ij}$ with both indices equal ($i = j$) for many materials. A major advantage of QPM is that it permits the polarization of all three interacting waves to be the same, chosen to access

the largest nonlinear coefficient. This also ensures the absence of spatial walk-off under NCPM. The nonlinear coefficient of the material is modulated with a period $\Lambda = 2L_c$ for an optimum 50% duty cycle. The phase-matching equation for quasi-phase-matching is modified from equation (2.28) to include the grating vector as [4, 7, 8]

$$\Delta k = k_3 - k_2 - k_1 - \frac{2\pi m}{\Lambda} \tag{2.35}$$

where $m$ is the order of the QPM interaction. The effective nonlinear coefficient is given by [7]

$$d_{\text{eff}} = \frac{2}{\pi m} d_{ij} \tag{2.36}$$

Therefore for a first-order ($m = 1$) QPM interaction, the effective nonlinearity is

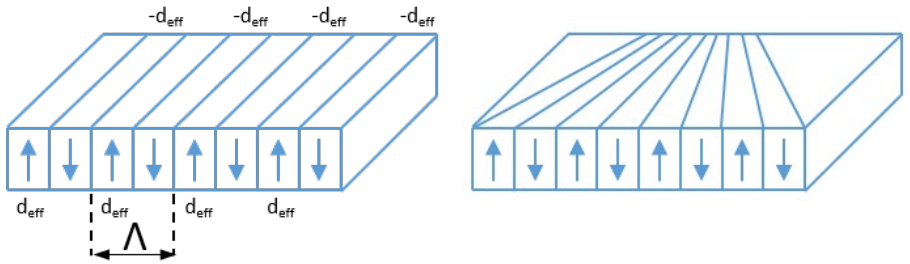


(a) Uniform grating (b) Fanout grating

Figure 2.3: Grating design in a quasi-phase-matched nonlinear crystal.

reduced by a factor $2/\pi$, which is often more than compensated by access to the highest nonlinear coefficient in QPM as compared to BPM. The typical value of $\Lambda$ is of the order of ∼10 µm for pumping in the green, to generate wavelengths in the visible and near-IR, and ∼30 µm for pumping at 1 µm to generate wavelengths in the mid-IR. As can be seen from equation (2.35), the phase-matching condi-

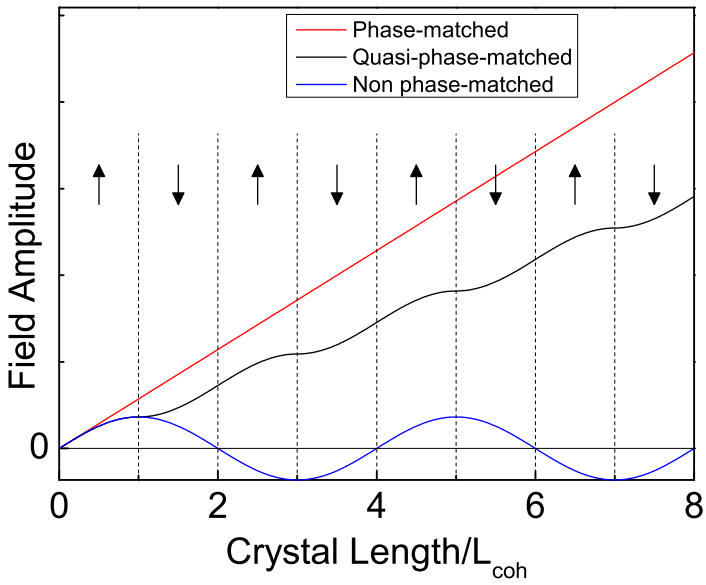


Figure 2.4: Evolution of field amplitude along the crystal length for perfect phase-matching, quasi-phase-matching, and no-phase-matching conditions.

tion can be altered by changing the grating period $\Lambda$. This introduces another degree of freedom to tune the generated wavelengths. For this reason, the crystal is sometimes poled in a fan-out grating structure with a continuously varying grating period across its aperture, as shown in Fig. 2.3(b). The grating periods can be continuously changed by lateral translation of the crystal, and wide and rapid wavelength tuning can be achieved at a fixed temperature. The evolution of the generated field amplitude along the crystal length for perfect BPM, QPM, and non-phase-matched conditions are shown in Fig. 2.4. As can be seen, for a given $d_{\text{eff}}$ value, the growth of field amplitude is the highest for perfect phase-matching, and there are periodic oscillations for no-phase-matching. In practice, however, because of access to the highest nonlinear coefficient in QPM, the out-

put intensity can grow more strongly than perfect BPM for the same nonlinear material.

## 2.7 Optical parametric oscillator

As mentioned in section 2.3, an optical parametric oscillator is a device capable of generating tunable coherent radiation over a wide spectral range, and consists of a nonlinear crystal placed within an optical resonator. An input pump beam at $\omega_p$ is parametrically down-converted into the signal at $\omega_s$ and the idler at $\omega_i$ in an OPO. The source of the pump beam is a laser. The general energy conservation and phase-matching equations ((2.7) and (2.8)) for OPO can be written as

$$\omega_p = \omega_s + \omega_i \tag{2.37}$$

$$k_p = k_s + k_i \tag{2.38}$$

The process of optical parametric oscillation is initiated in the nonlinear crystal by conversion of input pump photons into signal and idler photons by spontaneous optical parametric generation due to quantum noise. The generated signal and idler fields resonate within the optical cavity and mix with the pump field inside the nonlinear crystal, where mixing of pump and signal results in the generation of idler, and similarly, mixing of pump and idler results in the generation of signal under phase matching. This results in the macroscopic amplification of the signal and idler fields due to optical parametric amplification. Parametric processes are effectively instantaneous, and no energy is stored in the nonlinear medium. Hence, the gain in an OPO is also instantaneous, and the temporal

properties of the pump beam are transferred to the generated signal and idler beams. Continuous-wave (cw) OPOs are pumped by cw lasers, while pulsed OPOs are typically pumped by pulsed lasers. Depending on the fields that are resonant inside the cavity, an OPO can be classified as a singly-resonant oscillator (SRO), *doubly-resonant oscillator* (DRO) or *triply-resonant oscillator* (TRO) [9]. These will be further explained in section 2.7.1

### 2.7.1 Oscillator configurations

Efficient operation of OPO requires attaining sufficient gain for the parametrically generated waves. This is achieved by resonating the generated waves inside the cavity to provide feedback and facilitate their mixing with the pump wave to convert more pump power into signal and idler power. By controlling the reflectivities of cavity mirrors, one can choose which of the waves should be resonant in the cavity. In a SRO configuration, only one of the generated waves, either the signal or the idler is resonant in the cavity, while the other generated wave is completely extracted from the cavity together with the undepleted pump. If both signal and idler are resonant in the cavity, then this configuration is known as DRO. If all three waves, the signal, idler and pump, are resonant in the cavity, then it is a TRO configuration. Another scheme that is sometimes used is the *pump-enhanced singly resonant oscillator* (PE-SRO), in which the pump is resonant together with one of the generated waves. If output coupling is deployed in the cavity to extract some intracavity power from a SRO, then this configuration is known as *output-coupled singly-resonant oscillator* (OC-SRO). Resonating more than one wave, as is the case in DRO, TRO, and PE-SRO leads to a significantly lower threshold. However, resonating multiple waves leads to instabilities,

and stable operation in the case of DRO and TRO is challenging, as it requires simultaneous fulfilment of cavity resonance conditions at two or three different wavelengths.

### 2.7.2 Gain, amplification, and threshold

The coupled wave equations (2.25) - (2.27) can be solved for a nonlinear crystal of length $L$, to obtain an expression for the generated signal and idler fields. Under the assumption that the pump wave $A_p$ does not significantly deplete as it propagates through the crystal, known as *undepleted pump approximation*, the equations can be solved and results can be expressed as [4]

$$A_s(L) = \left[A_s(0)\left(\cosh gL - \frac{i\Delta k}{2g}\sinh gL\right) + \frac{2id_{\text{eff}}\omega_s^2 A_p}{gk_s c^2}A_i^*(0)\sinh gL\right]e^{i\Delta kL/2} \tag{2.39}$$

$$A_i(L) = \left[A_i(0)\left(\cosh gL - \frac{i\Delta k}{2g}\sinh gL\right) + \frac{2id_{\text{eff}}\omega_i^2 A_p}{gk_i c^2}A_s^*(0)\sinh gL\right]e^{i\Delta kL/2} \tag{2.40}$$

where $g = \left[\Gamma^2 - (\Delta k/2)^2\right]^{1/2}$, and $\Gamma^2$ is the gain factor defined as

$$\Gamma^2 = \frac{4\omega_s\omega_i d_{\text{eff}}^2 |A_p|^2}{c^2 n_s n_i} = \frac{8\pi^2 d_{\text{eff}}^2}{c\epsilon_0 n_p n_s n_i \lambda_s \lambda_i} I_p \tag{2.41}$$

where the definition of pump intensity $I_p = 2n_p\epsilon_0 c|A_p|^2$ has been used. Considering the boundary conditions that there is no idler field initially present, $A_i(0) = 0$, and arbitrary $A_s(0)$, the net fractional gain in the signal intensity in a single pass through the crystal can be expressed as [1]

$$G_s(L) = \frac{I_s(L)}{I_s(o)} - 1 = \Gamma^2 L^2 \frac{\sinh^2\left[\Gamma^2 L^2 - (\Delta kL/2)^2\right]^{1/2}}{\left[\Gamma^2 L^2 - (\Delta kL/2)^2\right]} = \Gamma^2 L^2 \frac{\sinh^2 gL}{g^2 L^2} \quad (2.42)$$

In most situations of practical interest, we have small gains for which $\Gamma^2 L^2 \ll (\Delta kL/2)^2$, and equation (2.42) can be modified to yield a small signal gain as

$$G_s(L) \approx \Gamma^2 L^2 \mathrm{sinc}^2\left(\frac{\Delta kL}{2}\right) \quad (2.43)$$

where the trigonometric identity $\sinh(ix) = i\sin(x)$ has been used. Under perfect phase-matching ($\Delta k = 0$), equation (2.42) becomes

$$G_s(L) = \sinh^2(\Gamma L) \quad (2.44)$$

which for low gains ($\Gamma L \leq 1$) approximates to

$$G_s(L) \approx \Gamma^2 L^2 \quad (2.45)$$

and for high gain ($\Gamma L \gg 1$) becomes

$$G_s(L) \approx \frac{1}{4} e^{2\Gamma L} \quad (2.46)$$

Thus, in the low-gain limit, the gain depends quadratically on $\Gamma L$, and experimentally it corresponds to parametric generation using cw or low- to moderate -peak-power pulsed pump sources, whereas in the high-gain limit, the gain increases exponentially with $2\Gamma L$, and corresponds to using high-intensity pulsed

pump sources. Redefining equation (2.41) in terms of the degenerate wavelength $\lambda_0 = 2\lambda_p$, and defining the degeneracy factor $\delta$ such that $\lambda_s = \lambda_0/(1+\delta)$ and $\lambda_i = \lambda_0/(1-\delta)$, we obtain

$$\Gamma^2 = \frac{8\pi^2 d_{\text{eff}}^2}{c\epsilon_0 n_0^2 n_p \lambda_0^2}(1-\delta^2)I_p \tag{2.47}$$

where $n_0$ is the refractive index for $\lambda_0$ and $n_0 \sim n_s \sim n_i$ is assumed. From equation (2.47) we can see that the parametric gain reduces as we move away from the condition of degeneracy ($\lambda_0 = \lambda_s = \lambda_i = 2\lambda_p$). As mentioned in the previous section, only one of the generated waves is resonant inside the optical cavity for a SRO. The threshold is reached when the fractional round-trip parametric gain experienced by the resonant wave is equal to the fractional round-trip losses due to absorption, reflection and output coupling. As a cw OPO falls under the low-gain regime, the threshold condition for a cw SRO can be obtained by equating equation (2.45) to the loss, expressing as

$$\frac{8\pi^2 L^2 d_{\text{eff}}^2 I_{th}}{c\epsilon_0 n_p n_s n_i \lambda_s \lambda_i} = \alpha_s \tag{2.48}$$

where $I_{th}$ is the pump intensity required to reach threshold, and $\alpha_s$ is the fractional round-trip power loss for the signal wave. A more useful form of the cw SRO threshold in terms of input pump power, and accounting for focussed Gaussian beams, is given by [8, 10]

$$P_{\text{th}} = \frac{\alpha_s}{T_P}\frac{\epsilon_0 c n_s n_i \lambda_p \lambda_s \lambda_i}{64\pi^2 d_{\text{eff}}^2}\frac{1+K}{L h_{sm}} \tag{2.49}$$

where $T_p$ is the transmission of of the pump through the input mirror and crystal surface, $K = k_p/k_s$, and $h_{sm}$ is the focussing factor [10]. The pump intensity threshold for a nanosecond SRO is given by [11, 12]

$$I_{th} = \frac{c\epsilon_0 n_p n_s n_i \lambda_s \lambda_i}{8\pi^2 L_{\text{cav}}^2 d_{\text{eff}}^2} \frac{1.8}{g_s} \left( \frac{25 L_{\text{cav}}}{c\tau} + 2\alpha L + ln \frac{1}{\sqrt{R}} + \ln 2 \right)^2 \tag{2.50}$$

where $g_s$ is the mode coupling coefficient, given by $g_s = w_{0p}^2/(w_{0p}^2 + w_{0s}^2)$, $L_{\text{cav}}$ is the optical cavity length, $2\alpha L$ is the round-trip loss through the crystal, and $R$ is the reflectivity of the output coupler accounting for all discrete cavity losses.

### 2.7.3 Phase-matching bandwidth

As seen from equation (2.42), the gain in parametric interaction is strongly dependent on the phase-mismatch, $\Delta k$, with maximum gain occurring for $\Delta k = 0$. The phase-matching bandwidth is defined as the maximum tolerable phase-mismatch $|\Delta k|$ for which the parametric gain has fallen to half the value of the max gain at $\Delta k = 0$. For the gain given by equation (2.42), $|\Delta k| \approx \pi/L$ is a good approximation for the maximum tolerable phase-mismatch [1, 13, 14], which corresponds to $-\pi/2 \leq \Delta k L/2 \leq \pi/2$, and the full-width-at-half-maximum (FWHM) is $\Delta k \approx 2\pi/L$. The acceptance bandwidth of a given parameter corresponding to the phase-matching bandwidth or giving rise to the phase-matching bandwidth can be calculated by doing a Taylor series expansion of $\Delta k$ about the given parameter [1, 5, 13]. For a SRO with a fixed signal wavelength $\lambda_s$, the pump acceptance bandwidth is given by [5, 14]

$$\Delta\lambda_p = \frac{\lambda_p^2}{L} \left[ (n_p - n_i) + \lambda_i \frac{\partial n_i}{\partial \lambda_i} - \lambda_p \frac{\partial n_p}{\partial \lambda_p} \right]^{-1} \tag{2.51}$$

Thus, $\Delta\lambda_p$ can be considered the maximum allowable pump bandwidth about $\lambda_p$, which is efficiently converted into the signal and the idler for a given crystal length. The signal linewidth of the generated signal for a given pump $\lambda_p$ is given by [5, 14]

$$\Delta\lambda_s = \frac{\lambda_s^2}{L}\left[(n_i - n_s) + \lambda_s\frac{\partial n_s}{\partial\lambda_s} - \lambda_i\frac{\partial n_i}{\partial\lambda_p}\right]^{-1} \tag{2.52}$$

Other bandwidths such as temperature and angular acceptance bandwidths can be calculated in a similar manner. Note that the pump acceptance bandwidth is an important parameter to be considered for ultrafast OPOs where the pump source is a broadband pulsed laser. However, it is not of the same importance for cw OPOs where the pump source is typically a single mode cw laser.

### 2.7.4 Material requirements

The choice of the nonlinear material for the parametric interaction(s) depends on various parameters. The material of choice should be non-centrosymmetric, with sufficient nonlinearity. It should also have a wide transparency range, large acceptance bandwidths, high damage threshold, low spatial walk-off, good mechanical and thermal properties. The availability of high-quality crystals with large apertures and low transmission losses is also very important. In many situations of practical interest, ideal materials are not available and a compromise has to be made depending on the the type of output desired. Another important parameter determining the suitability of the nonlinear material is the nonlinear *figure-of-merit* (FOM)

$$\text{FOM} = \frac{d_{\text{eff}}^2}{n_p n_s n_i} \tag{2.53}$$

The nonlinear figure-of-merit is directly related to the gain factor described in equation (2.42), and thus having a large FOM is desirable for the frequency conversion process.

### 2.7.5 Wavelength tuning

The main motivation for using an OPO as a light source is the possibility to continuously tune the output across a wide wavelength range, often in the range of few hundreds of nanometres or even more. Wavelength tuning is primarily achieved by altering the phase-matching condition of the nonlinear crystal. Depending on the type of phase-matching deployed, wavelength tuning in OPOs can be achieved in many different ways.

- Angle tuning: For BPM under CPM, rotation of the crystal results in change of refractive indices and thus the phase-matching condition, leading to wavelength tuning.

- Temperature tuning: For BPM and QPM systems under NCPM, the phase-matching condition can be changed by changing the temperature of the crystal, thereby varying the refractive indices, leading to wide wavelength tunability. Temperature tuning curves of a QPM system based on MgO:cPPLT under green-pumping, using relevant Sellmeier equations of the material [15], are shown in Fig. 2.5.

- QPM grating tuning: For QPM systems, wavelength tuning can also be achieved by changing the QPM grating period. This is exploited in fan-out grating designs, where the QPM grating period varies continuously across the lateral dimension of the crystal, leading to wide wavelength tuning at

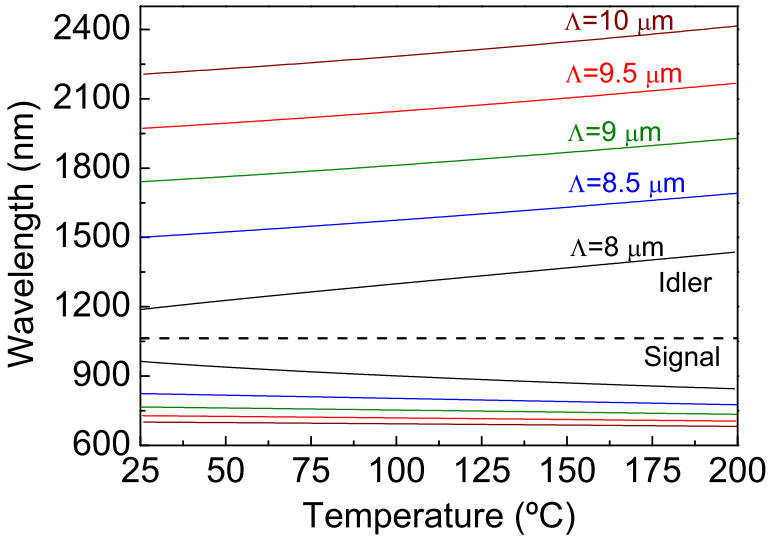


Figure 2.5: Green-pumped QPM temperature tuning curves of MgO:cPPLT.

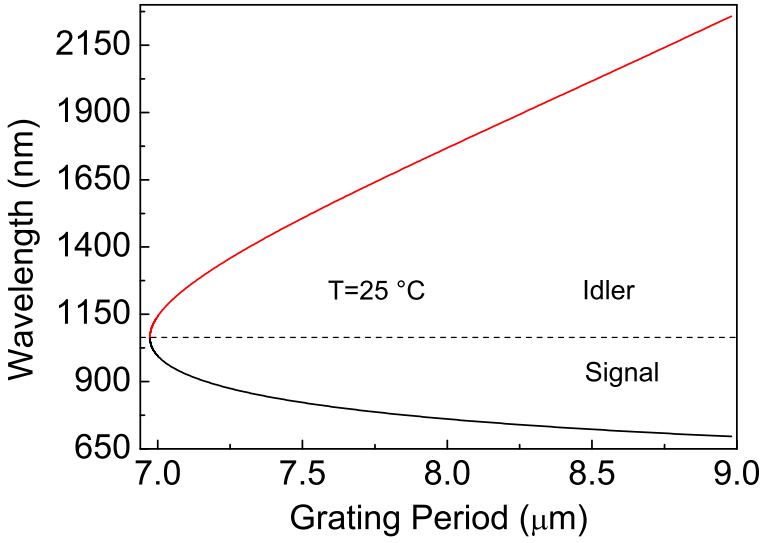


Figure 2.6: Green-pumped QPM grating tuning curve of MgO:PPLN.

a fixed temperature. A grating tuning curve of MgO:PPLN under green pumping, using relevant Sellmeier equations of the material [16], is shown in Fig. 2.6.

Apart from these methods, some other ways of achieving wavelength tuning include pump wavelength tuning and cavity length tuning. However, cavity length tuning is generally deployed in ultrafast OPOs. The work presented in this thesis is exclusively based on QPM nonlinear materials and wavelength tuning is achieved by utilizing temperature tuning and grating period tuning.

### 2.7.6 Cavity Design

The successful operation of an OPO requires an optimum resonator design, along with using a suitable nonlinear crystal and a pump source. The typical cavity configurations used in OPOs are shown in 2.7. The linear cavity, V-cavity and X cavity are standing-wave cavities, while a ring X-cavity is a travelling-wave cavity. X-cavity is typically used in ultrafast OPOs, where long cavity lengths are required to match the round-trip time to the repetition rate of the pump source. This can also be achieved with a V-cavity. For nanosecond OPOs, linear or V-cavities are typically used as they require short cavity lengths to ensure low rise time and high gain by having multiple round trips of the resonating wave within the same pump pulse. For cw OPOs, linear or ring cavities can be used. Despite the different configuration, using a ring cavity is advantageous because light only propagates in one direction, thus eliminating back-reflection into the pump laser and avoiding the need for an optical isolator. Moreover, the single pass of the resonating wave through the nonlinear crystal in each round-trip reduces the losses due to material absorption and crystal coatings. This can reduce

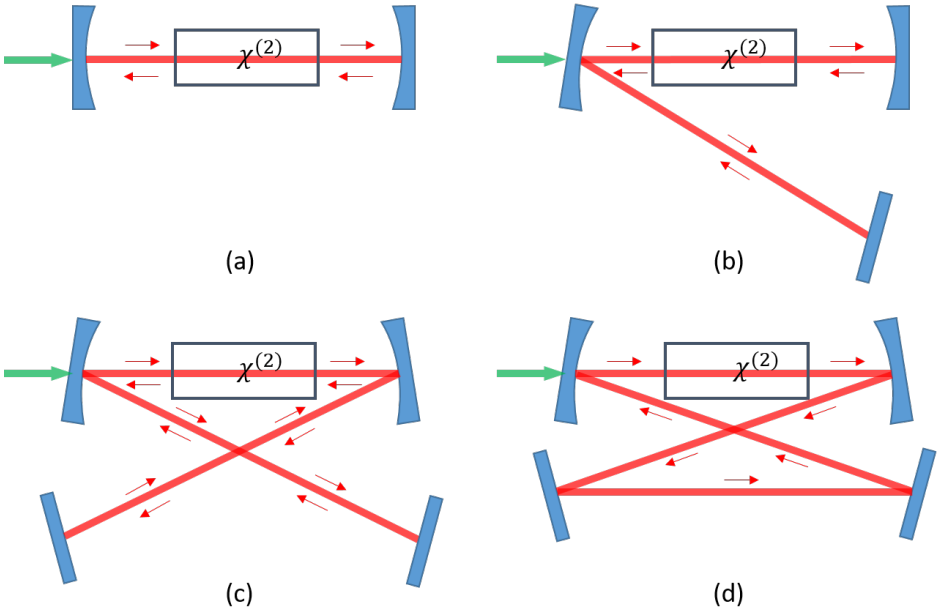


Figure 2.7: Cavity configurations for OPOs: (a) linear cavity, (b) V-cavity, (c) X-cavity, (d) ring cavity.

the threshold and minimize the thermal effects in the nonlinear crystal. This design also makes it easier to deploy resonant wave output coupling. The ring cavity design also offers the possibility of introducing intracavity elements such as an etalon for frequency selection, or suitable nonlinear crystals for intracavity frequency conversion at the second beam waist of the cavity. Gaussian beam transformation matrices, also known as ray matrices or ABCD matrices, are typically used to design the above mentioned cavity configurations. For good performance of the OPO, optimum overlap of pump beam with the resonant beam(s) is required. This is called mode-matching, where the confocal parameter of the pump beam must be equal to the confocal parameter of the resonant

beam(s), with them being focused at the centre of the crystal. The beam waist at any position in the cavity can be calculated using ABCD matrices, which will be described in the next section.

**Gaussian beam transformation matrices**

For a Gaussian beam propagating in a straight line along the $z$ direction with a minimum beam waist $w_0$ at $z = 0$, i.e $w(0) = w_0$, the radius of curvature $R(z)$ and the beam waist $w(z)$ of the wavefront at any position $z$ can be calculated using the following equations [17, 18]

$$R(z) = z\left(1 + \frac{z_0^2}{z^2}\right) \tag{2.54}$$

$$w(z) = w_0\left(1 + \frac{z^2}{z_0^2}\right)^{1/2} \tag{2.55}$$

where $z_0 = \pi n w_0^2/\lambda$ is known as the Rayleigh range, $n$ is the refractive index, and λis the wavelength of the Gaussian beam. The confocal parameter $b$ is twice the Rayleigh range, $b = 2z_o$. The complex $q$ parameter of the Gaussian beam is defined as

$$\frac{1}{q} = \frac{1}{R(z)} - \frac{i\lambda}{\pi n w^2(z)} \tag{2.56}$$

The Gaussian beam transformation matrices allow various optical elements such as lenses, mirrors and different mediums to be represented by corresponding $2 \times 2$ matrix of the form $\begin{pmatrix} a & b \\ c & d \end{pmatrix}$. Some ray matrices for common optical elements are listed in Table 2.2.

The overall ABCD matrix of a composite system is obtained by multiplication of the individual transformation matrices, where the order of matrix multiplication

| | |
|---|---|
| Propagation over distance $d$ | $\begin{pmatrix} 1 & d \\ 0 & 1 \end{pmatrix}$ |
| Refraction at interface<br>$n_a$ : initial refrative index, $n_b$ : final refrative index | $\begin{pmatrix} 1 & 0 \\ 0 & \frac{n_a}{n_b} \end{pmatrix}$ |
| Thin lens of focal length $f$ | $\begin{pmatrix} 1 & 0 \\ \frac{-1}{f} & 0 \end{pmatrix}$ |
| Reflection from a curved mirror<br>$R_e = R\cos\theta$ in tangential plane, $R_e = R/\cos\theta$ in saggital plane | $\begin{pmatrix} 1 & 0 \\ \frac{-2}{R_e} & 0 \end{pmatrix}$ |

Table 2.2: Ray matrices of common optical elements.

is inverse of the order in which the corresponding optical elements are traversed by light. After propagating through an optical element, or a composite system, the initial $q$ parameter, $q_1$ is modified according to

$$q_2 = \frac{Aq_1 + B}{Cq_1 + D} \tag{2.57}$$

Using (2.56) and (2.57), the beam waist radius at any arbitrary position $z$ is given by

$$w(z) = \sqrt{\frac{\lambda}{n\pi}\left(\frac{A^2 z_o^2 + B^2}{z_0(AD - BC)}\right)} \tag{2.58}$$

where, as mentioned before, the minimum beam waist $w_0$ occurs for $z = 0$, and thus the wavefront radius of curvature $R(0) = \infty$. For a stable cavity mode in a resonator, the resonating beam should reproduce itself after one round trip, that is the $q$ parameter is exactly reproduced after one round-trip. Using this condition and solving for $w$, we get [17, 18]

$$w^2 = \frac{|B|\lambda}{n\pi}\sqrt{\frac{1}{1 - \left(\frac{A+D}{2}\right)^2}} \tag{2.59}$$

From (2.59), we can see that for $w$ to be real, the condition of $((A+D)/2)^2 < 1$ must be satisfied. This gives us the resonator stability condition, $-1 < (A+D)/2 < 1$. Therefore, the focal lengths and physical separation of cavity mirrors should be carefully chosen to ensure that the total ABCD matrix for the resonator corresponds to a stable cavity. Using the transformation matrices together with the stability condition, we can calculate the evolution of the beam waist radius in the cavity starting from the center of the nonlinear crystal, and a typical cavity design plot for a ring cavity is shown in Fig. 2.8.

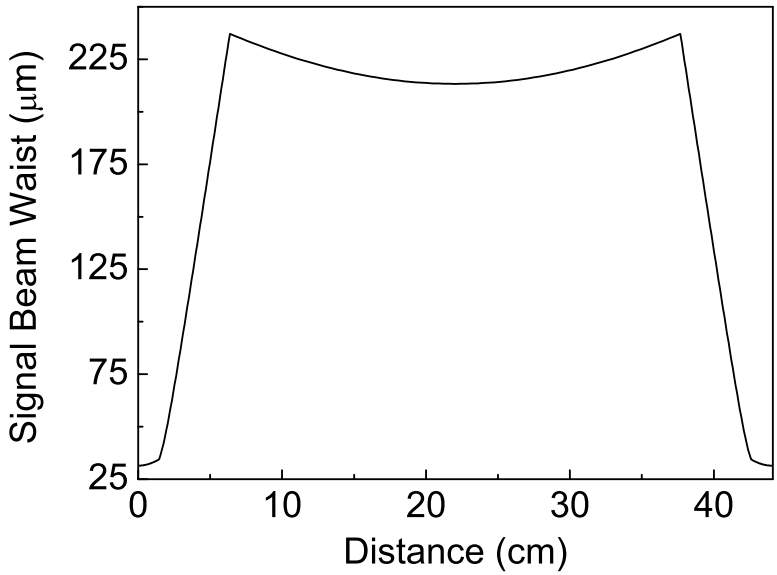


Figure 2.8: Signal beam waist in a ring cavity starting from the centre of the crystal.

## 2.8 Difference-frequency-generation

As mentioned in section 2.3, another second-order nonlinear process that can lead to the generation of new frequencies is DFG. For the process of DFG, an input signal source is also used together with the input pump source, with the output idler frequency being the difference of the two input frequencies. The energy conservation and the momentum conservation equations are identical to those for OPO and can be written as

$$\omega_p = \omega_s + \omega_i \tag{2.60}$$

$$k_p = k_s + k_i \tag{2.61}$$

The general solution of the coupled wave equations (2.25)-(2.27) are analogous to those for OPO (equations (2.39) and (2.40)).
In practice, it is simpler to build a setup for DFG compared to building a setup for an OPO, as DFG is a single pass process, thus eliminating the need of a complex resonant cavity, and does not require the attainment of an oscillation threshold. The output DFG power for a given input pump power $P_p$ and signal power $P_s$ is given by [19]

$$P_{\mathrm{DFG}} = \frac{32\pi^2 d_{\mathrm{eff}}^2 L}{c\epsilon_0 n_p^2 \lambda_i \lambda_s^2} P_s P_P h_1 \tag{2.62}$$

where $h_1$ is the focussing factor given by [19]. As can be seen from equation (2.62), the output DFG power scales linearly with both the input pump power, as well as the input signal power. Wavelength tuning in DFG process can be achieved

by either changing the input pump wavelength or the input signal wavelength, accompanied by the necessary changes (angle, temperature, grating period etc.) in the nonlinear crystal to maintain phase-matching. Given the lack of suitable lasers to pump cw OPOs in the mid-IR region, DFG is a viable alternative to develop high-power cw sources in the mid-IR.

# References

[1] M. Ebrahimzadeh and M. H. Dunn, "Optical parametric oscillators," in *Handbook of Optics* (OSA, 2000), chap. 22, second edn.

[2] P. A. Franken and J. F. Ward, "Optical harmonics and nonlinear phenomena," Reviews of Modern Physics **35**, 23 (1963).
https://link.aps.org/doi/10.1103/RevModPhys.35.23

[3] J. A. Armstrong, N. Bloembergen, J. Ducuing, and P. S. Pershan, "Interactions between light waves in a nonlinear dielectric," Physical Review **127**, 1918 (1962).
https://link.aps.org/doi/10.1103/PhysRev.127.1918

[4] R. W. Boyd, *Nonlinear Optics* (Academic Press, 2007).

[5] R. L. Sutherland, *Handbook of Nonlinear Optics* (Marcel Dekker, 2003).

[6] D. A. Kleinman, "Nonlinear dielectric polarization in optical media," Physical Review **126**, 1977 (1962).
https://link.aps.org/doi/10.1103/PhysRev.126.1977

[7] M. Fejer, G. Magel, D. Jundt, and R. Byer, "Quasi-phase-matched second harmonic generation: tuning and tolerances," IEEE Journal of Quantum Electronics **28**, 2631 (1992).
http://ieeexplore.ieee.org/document/161322/

[8] L. Myers and W. Bosenberg, "Periodically poled lithium niobate and quasi-phase-matched optical parametric oscillators," IEEE Journal of Quantum Electronics **33**, 1663 (1997).
http://ieeexplore.ieee.org/document/631262/

[9] M. Ebrahim-Zadeh, "Continuous-wave Optical Parametric Oscillators." in *Handbook of Optics* (OSA, 2010), Vol. IV, chap. 17, third edn.

[10] S. Guha, F. J. Wu, and J. Falk, "The Effects of Focusing on Parametric Oscillation," IEEE Journal of Quantum Electronics **18**, 907 (1982). http://ieeexplore.ieee.org/document/1071624/

[11] S. Brosnan and R. Byer, "Optical parametric oscillator threshold and linewidth studies," IEEE Journal of Quantum Electronics **15**, 415 (1979). http://ieeexplore.ieee.org/document/1070027/

[12] L. R. Marshall, J. Kasinski, A. D. Hays, and R. Burnham, "Efficient optical parametric oscillator at 1.6 µm," Optics Letters **16**, 681 (1991). https://www.osapublishing.org/abstract.cfm?uri=ol-16-9-681

[13] N. P. Barnes and V. J. Corcoran, "Parametric generation processes: spectral bandwidth and acceptance angles," Applied Optics **15**, 696 (1976). https://www.osapublishing.org/abstract.cfm?uri=ao-15-3-696

[14] M. Ebrahimzadeh, A. Henderson, and M. H. Dunn, "An excimer-pumped β-$BaB_2O_4$ optical parametric oscillator tunable from 354 nm to 2.370 µm," IEEE Journal of Quantum Electronics **26**, 1241–1252 (1990). http://ieeexplore.ieee.org/document/59664/

[15] K. Moutzouris, G. Hloupis, I. Stavrakas, D. Triantis, and M.-H. Chou, "Temperature-dependent visible to near-infrared optical properties of 8 mol% Mg-doped lithium tantalate," Optical Materials Express **1**, 458 (2011). https://www.osapublishing.org/ome/abstract.cfm?uri=ome-1-3-458

[16] O. Gayer, Z. Sacks, E. Galun, and A. Arie, "Temperature and wavelength dependent refractive index equations for MgO-doped congruent and stoichiometric $LiNbO_3$," Applied Physics B **91**, 343–348 (2008). http://link.springer.com/10.1007/s00340-008-2998-2

[17] J. T. Verdeyen, *Laser Electronics* (Prentice Hall, 1995), third edn.

[18] W. T. Silfvast, *Laser Fundamentals* (Cambridge University Press, 2004), second edn.

[19] S. Guha, J. O. Barnes, and L. P. Gonzalez, "Multiwatt-level continuous-wave midwave infrared generation using difference frequency mixing in periodically poled MgO-doped lithium niobate," Optics Letters **39**, 5018 (2014). https://www.osapublishing.org/abstract.cfm?uri=ol-39-17-5018

# 3. Widely tunable continuous-wave PPKTP optical parametric oscillator

This chapter is based on the following publication:

K. Devi, A. Padhye*, **Sukeert*** and M. Ebrahim-Zadeh, "Widely tunable room-temperature continuous-wave optical parametric oscillator based on periodically-poled $KTiOPO_4$," Optics Express **27**, 24093 (2019).

**equal contribution*

## 3.1 Motivation

Continuous-wave (cw) coherent sources capable of providing widely tunable radiation in the near-infrared (near-IR) in single-frequency output with good beam quality are of great importance for many applications including spectroscopy and trace gas sensing [1]. Optical parametric oscillators (OPOs) pumped in the green

are now recognized as viable sources for such radiation. Given the small parametric gain available under low pump intensities in the cw regime, to exploit the highest nonlinear coefficient in the nonlinear crystal, practical cw OPOs are exclusively based on quasi-phase-matched (QPM) nonlinear materials with long interaction lengths under non-critical phase-matching (NCPM). The QPM materials which have so far been explored in green-pumped cw OPOs include periodically-poled $LiNbO_3$ (PPLN), $LiTaO_3$ (PPLT), $KTiOPO_4$ (PPKTP), as well as MgO-doped PPLN (MgO:PPLN) and stoichiometric PPLT (MgO:sPPLT) [2]. To date, the vast majority of cw OPOs pumped at ∼1 µm have been based on PPLN, which are capable of providing spectral output up to ∼4 µm [3]. However, given the photorefractive damage induced by the visible pump or signal radiation below ∼1 µm, the development of green-pumped OPO based on PPLN is challenging. As such, there has been an ongoing quest for the exploitation of alternative nonlinear materials for the realization of viable cw OPOs in the visible and near-IR pumped in the green. By using a frequency-doubled Nd:YAG laser at 532 nm, a pump-enhanced PPLT cw OPO was previously reported [4], but attainment of high output powers was hampered by photorefractive damage in the crystal under green pumping. In PPLN and PPLT, doping with MgO has reduced the photorefractive susceptibility to visible radiation, thus enabling high power generation with wide wavelength tunability using green-pumped cw OPOs [5, 6]. With advances in QPM fabrication technology, cw OPO based on MgO:sPPLT in fan-out grating design have been developed, generating high powers across 734-1929 nm in the near-IR, while operating at room temperature [7]. On the other hand, the nonlinear crystal, PPKTP, having effective nonlinearity, $d_{\text{eff}}$ ∼9 pm/V, high damage threshold [8], and transparency across 0.35-4.5 µm, has higher pho-

torefractive damage threshold and negligible green-induced infrared absorption (GRIIRA) compared to both PPLN and PPLT. As such, it also does not require high temperature operation as in the case of PPLN and PPLT. Previous demonstrations of cw OPOS based on PPKTP include green-pumped doubly-resonant oscillator (DRO) [9, 10], intracavity-pumped singly-resonant ocillator (IC-SRO) [11], pump-enhanced singly-resonant ocillator (PE-SRO) [12], a singly-resonant ocillator (SRO) using a pair of multiple-grating PPKTP [13], and an output-coupled DRO [14]. In all such PPKTP-based cw OPOs reported to date, wavelength tuning has been achieved by using uniform QPM grating structure in combination with temperature tuning. Given that the change in crystal temperature is a slow process, as the crystal needs to be thermally stable at each defined temperature, wavelength tuning under this approach is not rapid. Moreover, damage in PPKTP has been observed at high temperatures when pumped at high green powers [13], thus limiting the tunable spectral range attainable at high powers when using uniform grating periods. On the other hand, wavelength tuning with continuous variation of QPM grating period can be achieved by using a fan-out structure at fixed temperature, which is a relatively fast process, and is potentially capable of providing broad spectral coverage [7]. With progress in QPM fabrication technology, the development of PPKTP in fan-out grating design has now become possible, motivating the exploitation of such structures for the development of cw OPOs capable of wide and rapid wavelength coverage without resort to temperature tuning. In this work, for the first time to our knowledge, we demonstrated a green-pumped cw OPO based on a fan-out grating design in PPKTP, enabling rapid and continuous wavelength tuning with lateral translation of the nonlinear crystal while operating at room temperature. More-

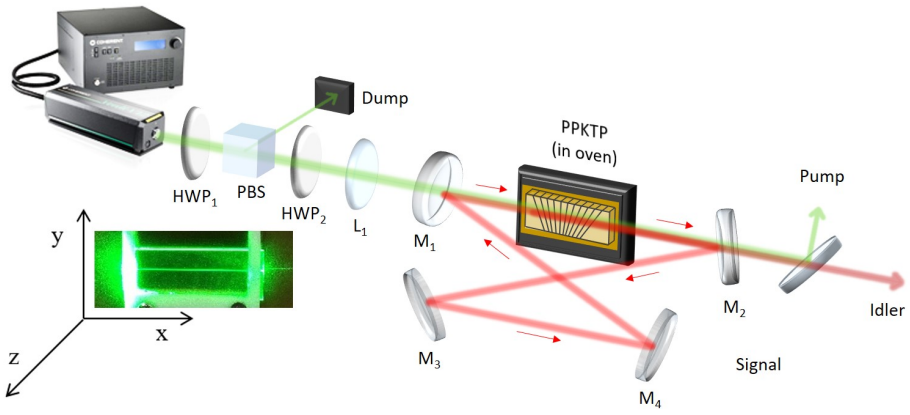


Figure 3.1: Schematic of the fan-out grating design PPKTP-based cw OPO. HWP: half-wave plate, PBS: polarizing beam-splitter, L: lens, $M_{1\text{-}4}$: mirrors, M': dichroic mirror. Inset: laboratory photograph of the PPKTP crystal.

over, by deploying signal output coupling in the PPKTP-based cw SRO, also for the first time, we investigated the performance of the device and demonstrated effective reduction in thermal loading of the crystal, resulting in an enhancement of output efficiency.

## 3.2 Experimental Setup

A schematic of the experimental setup is shown in Fig. 3.1. The OPO is pumped by a cw frequency-doubled Nd:$YVO_4$ solid-state laser delivering up to 10 W of output power at 532 nm in a single-frequency linearly-polarized beam with $M^2$<1.1. The PPKTP crystal has dimensions of $30 \times 11 \times 1$ mm$^3$, in a fan-out grating design with periods varying over $\Lambda$ = 9.00-10.85 µm across its lateral dimension. A laboratory photograph of the crystal is also shown in Fig. 3.1, and some material properties are listed in table 3.1. The crystal is housed in an

| Material | PPKTP |
|---|---|
| Manufacturer | Raicol |
| Effective nonlinear coefficient | ∼9 pm/V [8] |
| Transparency range | 0.35-4.5 µm [15] |
| Coercive field | 2 kV/mm [16] |
| Thermal conductivity (W/m-K) | $k_1$=2<br>$k_2$=3 [8]<br>$k_3$=3.3 |

Table 3.1: Material properties of the nonlinear crystal used for the OPO.

oven, adjustable from room temperature to 200 °C, with a temperature stability of ± 0.1 °C, and mounted on a linear translation stage (resolution of 10 µm) to enable smooth grating tuning across its lateral dimension in ± $y$ direction with fine and continuous translation of the crystal. The end faces of the crystal are antireflection (AR)-coated at 532 nm ($R$<0.5%), 720–990 nm ($R$<0.5%), and 1130–2040 nm ($R$<5%). The OPO is configured in a compact ring cavity comprising two concave mirrors, $M_{1,2}$ ($r$ = -100 mm), one plane mirror, $M_3$, and one plane output coupler, $M_4$. Mirrors, $M_{1\text{-}3}$, are highly reflecting ($R$>99.8%) for the signal (620–1030 nm) and highly transmitting ($T$>97%) for the idler (1078–3550 nm) and pump, while $M_4$ has an output coupling of 1% across 635-1100 nm, ensuring singly-resonant oscillation in the signal and single-pass pump. Mirror, $M_4$, can be replaced with a plane high reflector ($R$>99.8% over 620–1030 nm) for a pure SRO configuration. A dichroic mirror, M', is used to separate the output idler from the transmitted pump.

### 3.2.1 Crystal Characterization

Given the first demonstration of PPKTP in fan-out grating design, and in particular at high green powers, it is important to first characterize the crystal under single-pass pumping condition. To this end, we measured the transmission of the crystal as a function of pump intensity at various temperatures, with the pump beam in phase-matched polarization and orthogonal non-phase-matched polarization. The results are shown in Fig. 3.2(a) and 3.2(b), respectively. The measurements were performed at room temperature (T$\sim$25 ˚C), moderate temperature (T = 50 ˚C), and high temperature (T = 170 ˚C), while keeping the crystal at a fixed position. Transmission of $\sim$89.6%, $\sim$89.6% and $\sim$87% for phase-matched polarization, and $\sim$93.2%, $\sim$93.2% and $\sim$91.7% for orthogonal non-phase-matched polarization were obtained at T$\sim$25 ˚C, 50 ˚C and 170 ˚C, respectively. As evident from Fig. 3.2(a), the variation of crystal transmission with pump intensity at all temperatures remains negligible. We also observe no significant drop in transmission at high pump intensities, thus implying the absence of two-photon absorption. At high temperature, however a drop in transmission by $\sim$2.5% is observed for all pump intensities as compared to low temperatures. The behaviour of the crystal under orthogonal non-phase-matched polarization across the pump intensities, as seen in Fig. 3.2(b), is also similar, although at all temperatures the transmission is $\sim$4% higher than that under phase-matched polarization. The lower transmission under phase-matched polarization as compared to non-phase-matched polarization has been previously observed in uniform grating QPM structure KTP [15].

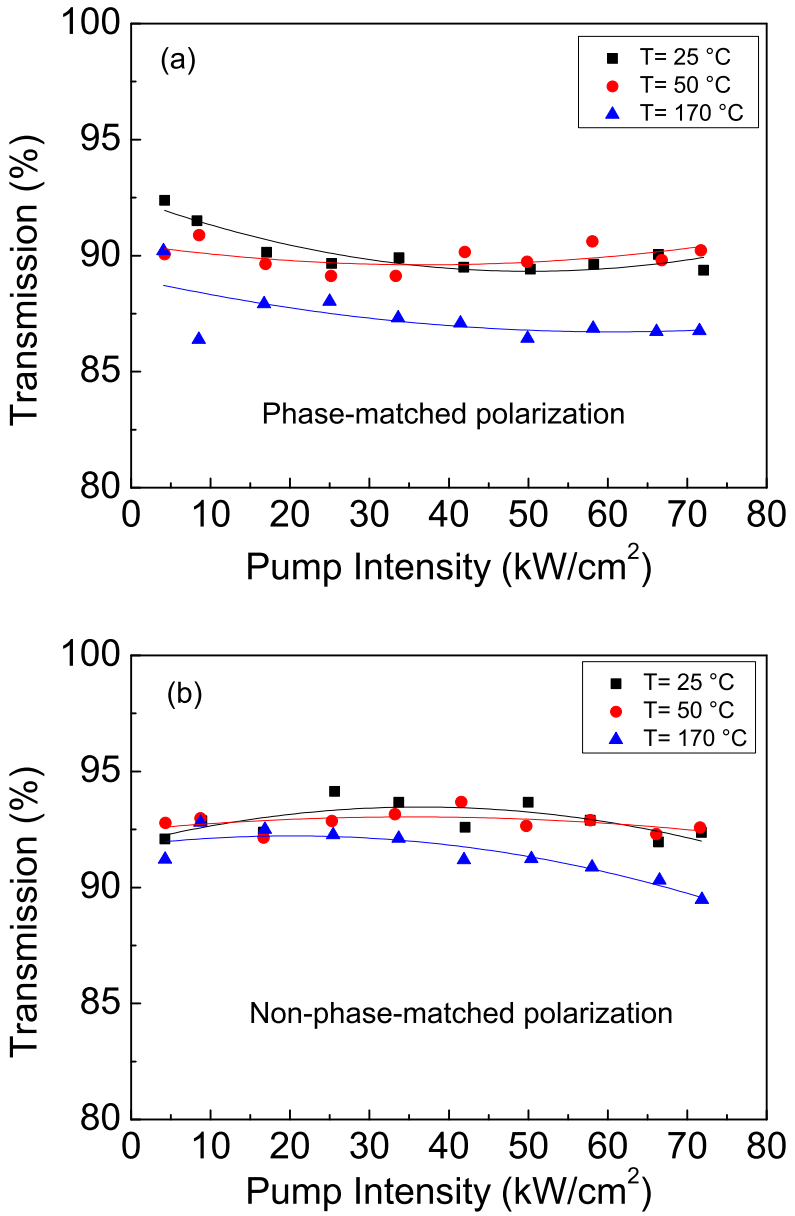


Figure 3.2: Variation of transmission of the fan-out-grating PPKTP crystal with pump intensity at temperature, T∼25 °C, 50 °C and 170 °C under (a) phase-matched polarization and (b) orthogonal non-phase-matched polarization.

## 3.3 Output-coupled SRO

In this section, we describe the characterization of the fan-out grating PPKTP OPO by deploying signal wave output coupling to extract useful signal power, thus increasing the overall extraction efficiency, as well as reducing the thermal load in the crystal due to high intracavity powers.

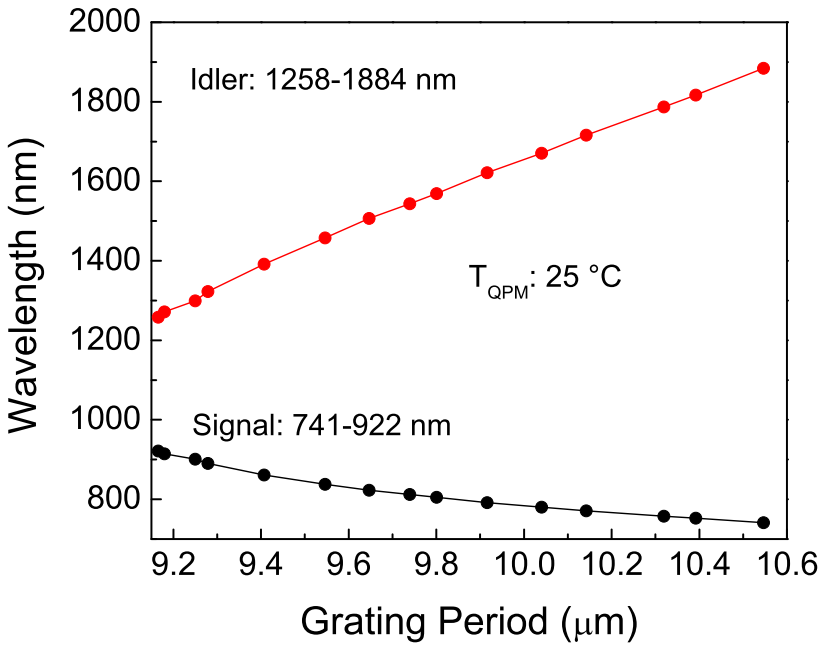


Figure 3.3: Wide wavelength tuning with lateral translation of PPKTP crystal at room temperature.

### 3.3.1 Wavelength tuning

Wavelength tuning in the present OPO can be achieved by lateral translation of the PPKTP crystal to vary the QPM grating period or by changing the crystal temperature, while keeping either parameter fixed. With the OPO in output-coupled SRO (OC-SRO) configuration, we initially varied the crystal position laterally while keeping the crystal at room temperature, and recorded the signal wavelength at optimum pump powers while generating maximum signal powers. Figure 3.3 shows the generated signal and corresponding idler wavelengths as function of crystal position at room temperature. As evident, the OPO is rapidly and continuously tunable across 741-922 nm in signal and 1258-1884 nm in idler. We were able to use 8.08 mm of the 11 mm crystal width, with the OPO ceasing to operate towards the edges of the crystal, accompanied by distortion of the pump beam. The initial operating position of the crystal was considered as the starting point (0 mm), and the gratings periods shown in Fig. 3.3 were estimated from the measured wavelengths by using Sellmeier equations of the material, as described below.

In order to verify our wavelength tuning measurements, we performed theoretical calculations based on the Sellmeier equations and thermo-optic dispersion relations for PPKTP, which have been studied extensively in many earlier reports [17–21]. To determine the grating period at a corresponding crystal position, we calculated the grating period variation across the width of the crystal from the experimentally measured wavelengths using relevant Sellmeier equations, with the results shown in Fig. 3.4. The calculations were performed within the generated spectral range in the OC-SRO configuration under room

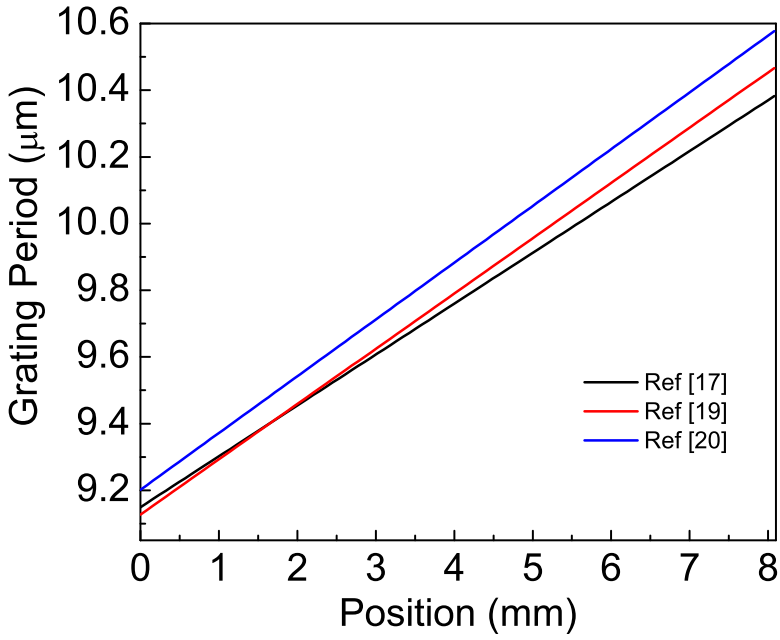


Figure 3.4: Theoretically calculated grating period corresponding to the crystal position at room temperature using Sellmeier equations for PPKTP.

temperature operation, using three Sellmeier equations [17, 19, 20]. As evident, the calculated variation in grating period with crystal position is different for the three Sellmeier equations. Thus, accordingly, signal tuning across 741-922 nm is achieved for calculated grating period variation across $\Lambda$ = 9.14-10.38 µm, $\Lambda$ = 9.12-10.47 µm, and $\Lambda$ = 9.20-10.58 µm, as shown in Fig. 3.4, obtained from [17], [19] and [20], respectively.

At a fixed crystal position of 0.492 mm, we also simulated temperature tuning curves using four different sets of refractive index temperature derivatives and Sellmeier equations, with the results shown in Fig. 3.5. The first and second set include the refractive-index temperature derivatives from [18] , and Sellmeier

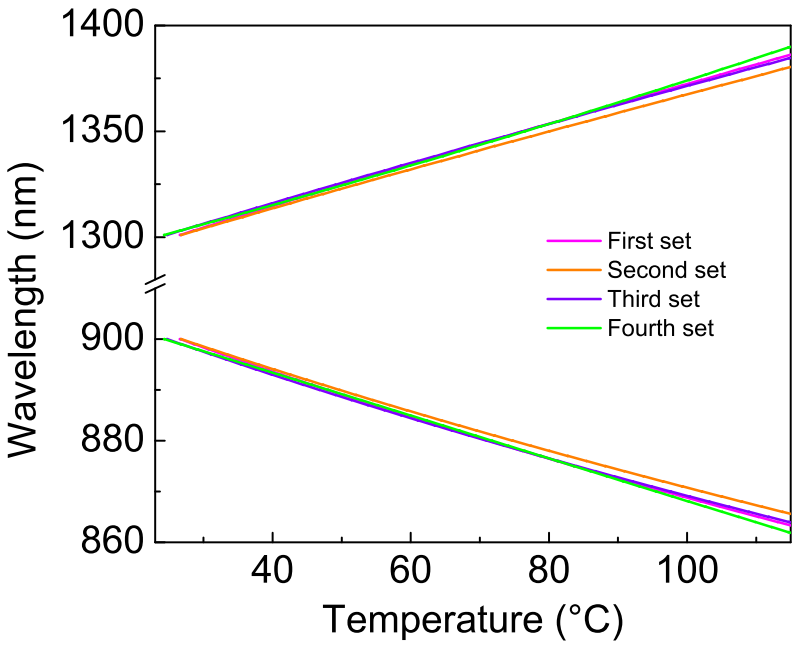


Figure 3.5: Theoretical temperature tuning curves obtained from the calculated grating periods at crystal position of 0.492 mm at room temperature and using thermo-optic dispersion relations in four different sets.

equations from [17] and [19], respectively. The third set includes the refractive index temperature derivatives and Sellmeier equations from [20], while the fourth set includes the refractive-index temperature derivatives from [21] and Sellmeier equations from [19]. Wavelength tuning was also obtained by varying the crystal temperature at the two possible extreme crystal positions. At position of 0.492 mm, as seen in Fig. 3.6, signal tuning across 865-901 nm and idler tuning across 1299-1381 nm was obtained by heating the crystal from room temperature to 112 °C. We further compared the theoretical calculations in Fig. 3.5 with the experimental temperature tuning data in Fig. 3.6, and observed that

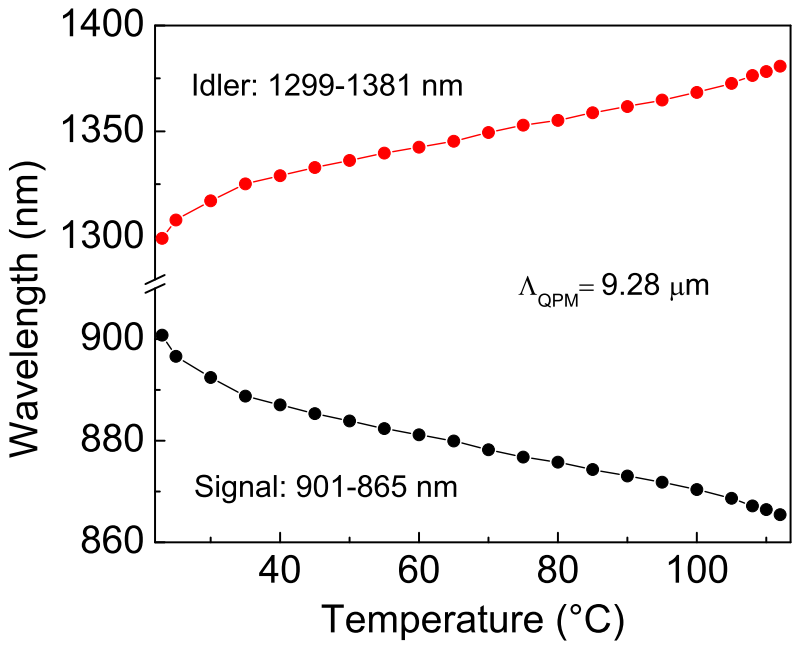


Figure 3.6: Temperature tuning at a fixed grating period of $\Lambda = 9.28$ µm.

the theoretical curves are in good agreement with experimental data at higher temperatures, with the closest agreement between theory and measurement data obtained using the third set. Thus, Sellmeier equations from [20] were used to calculate the grating periods mentioned throughout this chapter, and the crystal position of 0.492 mm corresponds to a calculated grating period of $\Lambda = 9.28$ µm. The wavelength tuning range in signal and idler was further expanded to 739 nm and 1901 nm, respectively, by temperature tuning the crystal at position of 8.08 mm, corresponding to a grating period of $\Lambda = 10.58$ µm, as seen in Fig. 3.7. However, as evident, in both cases the variation of wavelength with temperature is small. In particular, at the grating period of $\Lambda = 10.58$ µm, shown in Fig. 3.7,

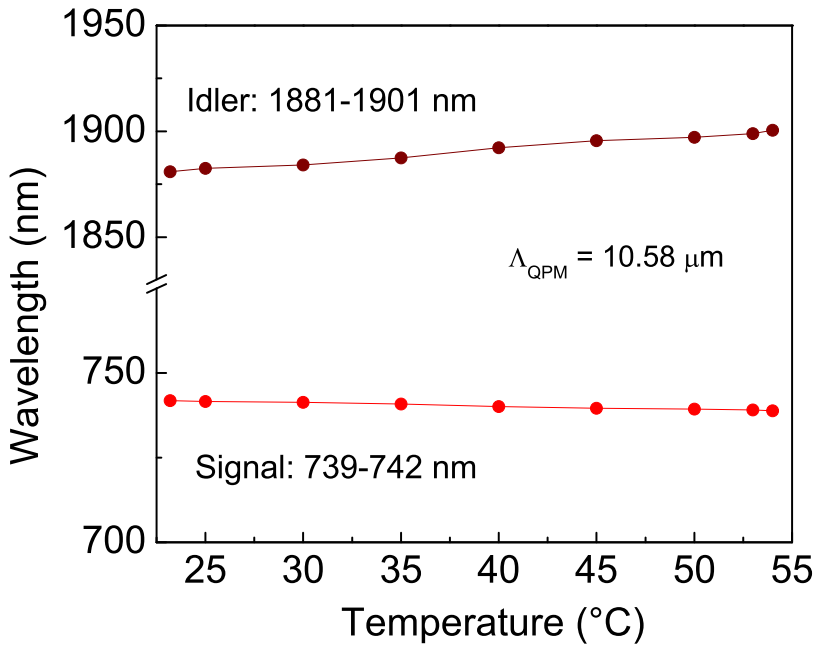


Figure 3.7: Temperature tuning at a fixed grating period of $\Lambda = 10.58$ μm.

as the OPO is tuned further away from degeneracy, the variation in the signal and idler wavelength with temperature is only 3 and 20 nm, respectively, due to the dispersion properties of PPKTP, similar to that in MgO:sPPLT [7]. We further observed that at higher temperatures the OPO would cease to operate, and the maximum temperature at which oscillation could be maintained decreases as we move away from degeneracy along the crystal lateral dimension. The OPO performance at high temperature and variation of wavelength with temperature show similar behavior at other crystal positions. This behavior is consistent with earlier reports, where operation of OPO has also been observed to be challenging above 150 °C, with damage also observed to the PPKTP crystal [13]. These

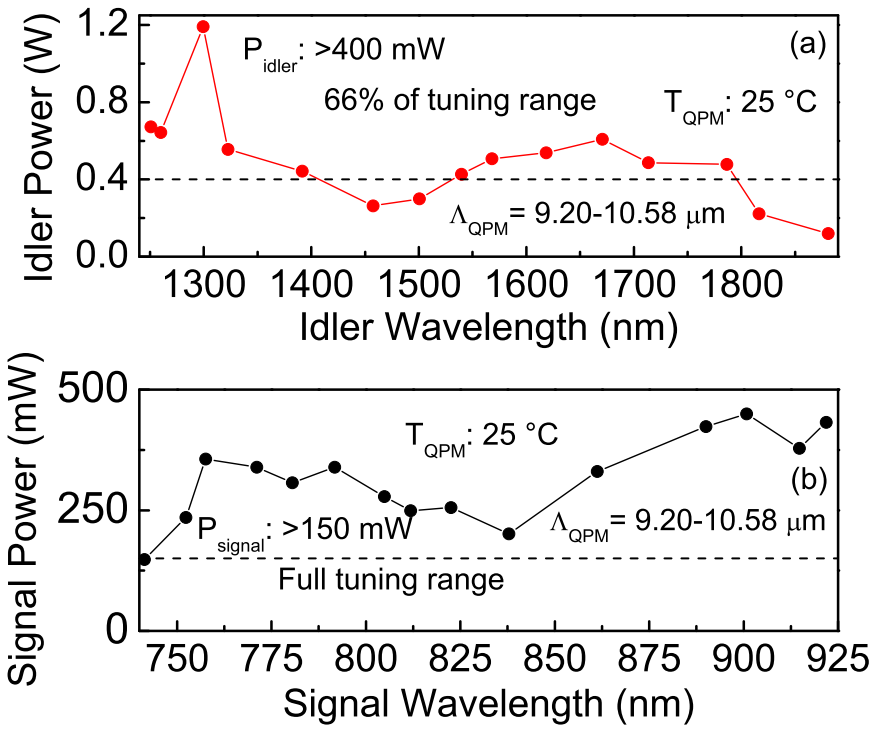


Figure 3.8: Variation of (a) signal, and (b) idler power across the grating period tuning range at room temperature.

limitations, thus, further support the merits of the fan-out grating design in PPKTP as a robust and efficient approach for the attainment of wide wavelength tuning at room temperature, as evident from Fig. 3.3, a more practical device architecture without the need for an oven, as well as higher output stability by avoiding increased thermal fluctuations at higher operating temperatures. We characterized the OPO with regard to output power by recording the extracted signal and idler power across the tuning range. We performed the measurements by grating tuning at room temperature, as well as by temperature tuning at fixed

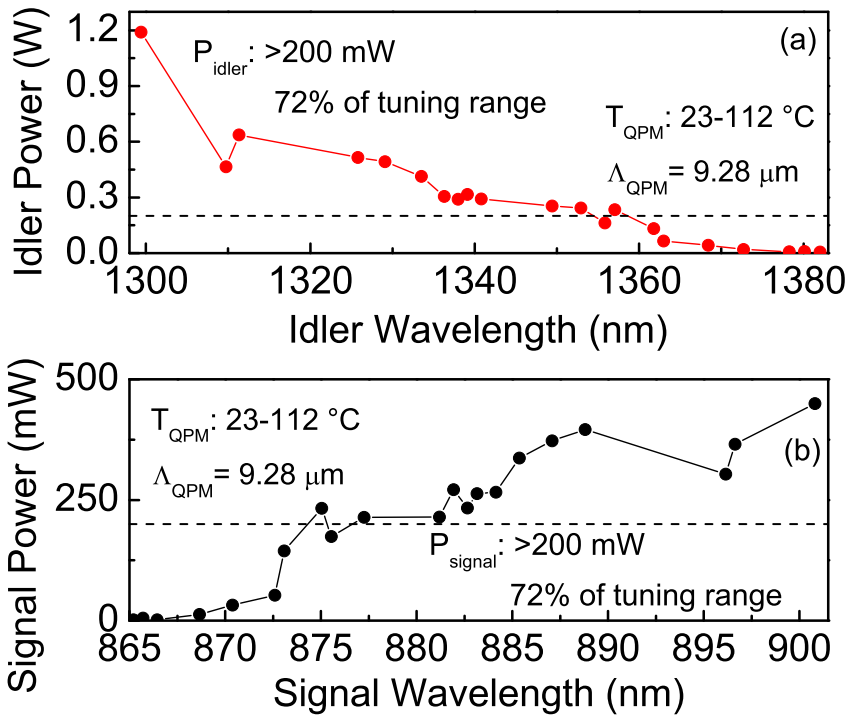


Figure 3.9: Variation of (a) signal, and (b) idler power across the temperature tuning range for grating period of $\Lambda = 9.28$ µm.

grating period for the shorter and longer periods of $\Lambda = 9.28$ µm and $\Lambda = 10.58$ µm. We were not able to use the shortest grating period of $\Lambda = 9.00$ µm and longest period of $\Lambda = 10.85$ µm, because the OPO ceased to operate towards the crystal edges, and the pump beam quality was observed to deteriorate after passing through the crystal at these extreme positions. Fig 3.8 shows the maximum generated power over the signal (741-922 nm) and idler (1258-1884 nm) tuning range at room temperature under optimum pumping, achieved with continuous grating tuning by lateral translation of the crystal across its width. As evident,

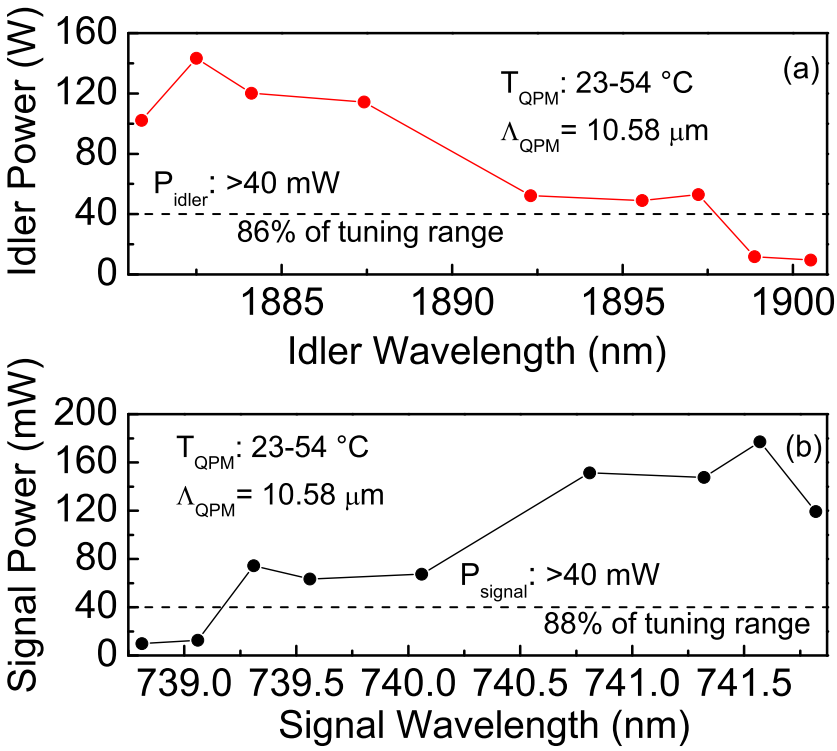


Figure 3.10: Variation of (a) signal, and (b) idler power across the temperature tuning range for grating period of $\Lambda = 10.58$ μm.

the OPO can provide >150 mW of signal power over the entire tuning range with up to 450 mW at 901 nm, and >400 mW of idler power over 66% of the tuning range with up to 1.2 W at 1299 nm, corresponding to total extraction efficiency of 30% for 5.5 W of pump power. We also recorded the maximum generated power at the shortest and longest grating periods of $\Lambda = 9.28$ μm and $\Lambda = 10.58$ μm, respectively, by temperature tuning, with the results shown in Fig. 3.9 and 3.10, respectively. As seen, at the shortest grating period, signal and idler powers of >200 mW over 72% of the tuning range were generated, while at the longest

grating period, signal and idler powers of >40 mW over 88% and 86% of the tuning range were obtained, respectively. The drop in power at shorter signal and longer idler wavelengths with the crystal at lower temperatures, as seen in Fig. 3.8 and 3.10, is attributed to the reduction in parametric gain away from degeneracy. However, the decline in power has also been observed at shorter idler wavelengths when the crystal temperatures are increased, as seen in Fig. 3.9, which is due to the degradation of the pump beam quality observed at higher temperatures. We note that in earlier work it has been reported that the operation of the PPKTP-based OPO ceases at higher temperatures [13], and this could be due to the degradation of the beam quality observed here.

### 3.3.2 Power scaling and stability

To investigate the power scaling capability of the OPO, we recorded the variation of output power in the signal and the corresponding idler with pump power, with the results shown in Fig. 3.11. The measurements were performed at room temperature for a fixed grating period of $\Lambda = 9.21$ µm. As evident, the output power increases with pump power, displaying small sharp transitions in signal and idler power as the pump power is increased, generating maximum idler power of 640 mW at 4.1 W of pump power and a maximum signal power of 367 mW at 4.5 W of pump power. The output powers recorded are the maximum powers observed at the corresponding pump power, with the cavity length kept unchanged throughout the power scaling measurements. As such, we believe the sharp transitions in the output powers observed with the increase in pump power could be due to the temperature fluctuations in the crystal at a given pump power, resulting in mode-hopping. Given that we have not observed any beam quality distortion

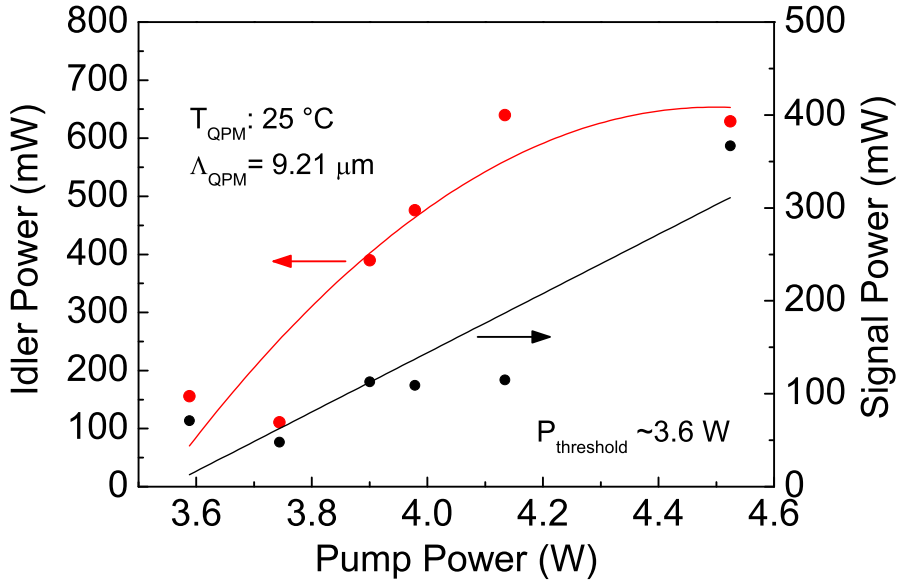


Figure 3.11: Idler and signal output power as a function of pump power at room temperature.

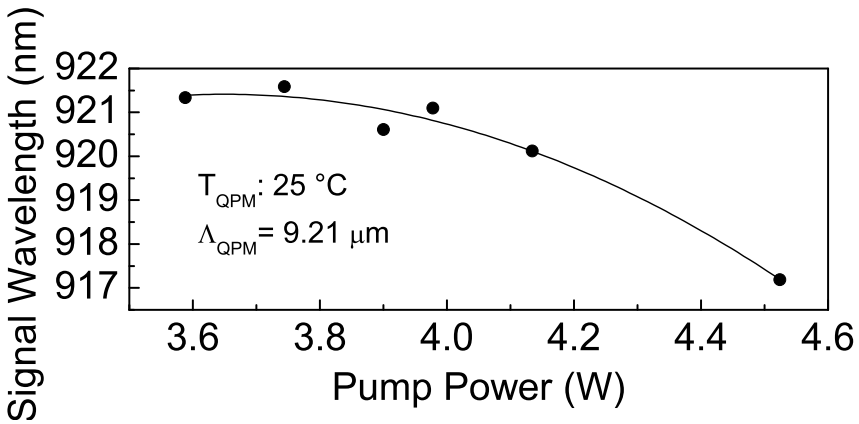


Figure 3.12: Variation of signal wavelength with pump power at room temperature.

after long-term operation at these pump powers, we believe there is negligible thermal lensing, but a stable cavity length is required at each pumping level to minimize output power fluctuations. With the increase in pump power beyond 5 W, under long-term operation, we observed distortion in the output beam profile. As such, to avoid thermal loading in the PPKTP crystal, we limited the maximum pump power to 4.5 W. The threshold pump power was recorded to be 3.6 W. We further investigated the OPO signal wavelength as a function of pump power for the same grating period of $\Lambda = 9.21$ µm at room temperature, with the results shown in Fig. 3.12. As evident, the signal wavelength is observed to undergo sudden transitions with small variations in pump power, also decreasing from 921 nm to 917 nm with the increase in pump power from 3.6 W to 4.5 W. This decrease in signal wavelength is attributed to the increase in crystal temperature with the increase in pump power due to residual absorption of ∼10% at 532 nm (see section 3.2.1). Using the relevant Sellmeier and thermo-optic dispersion relations [20], we have theoretically calculated that for the period of $\Lambda = 9.21$ µm at room temperature, an increase in the crystal temperature by 7.6 °C results in a decrease in signal wavelength by ∼4 nm. We also performed the power stability measurements of the output idler at 1517 nm and corresponding signal at 820 nm, under free-running conditions for a pump power of 5.43 W at the input to the OPO, with the crystal kept at room temperature, and after allowing a few minutes to reach steady-state operation. The results are shown in Fig. 3.13. As can be seen, the idler and signal powers exhibit a passive stability better than 3.2% rms and 5.5% rms, respectively, over 2.6 minutes. The fluctuation in OPO output power could be attributed to mechanical vibrations and in large part to the temperature fluctuations in the PPKTP crystal due to thermal lensing com-

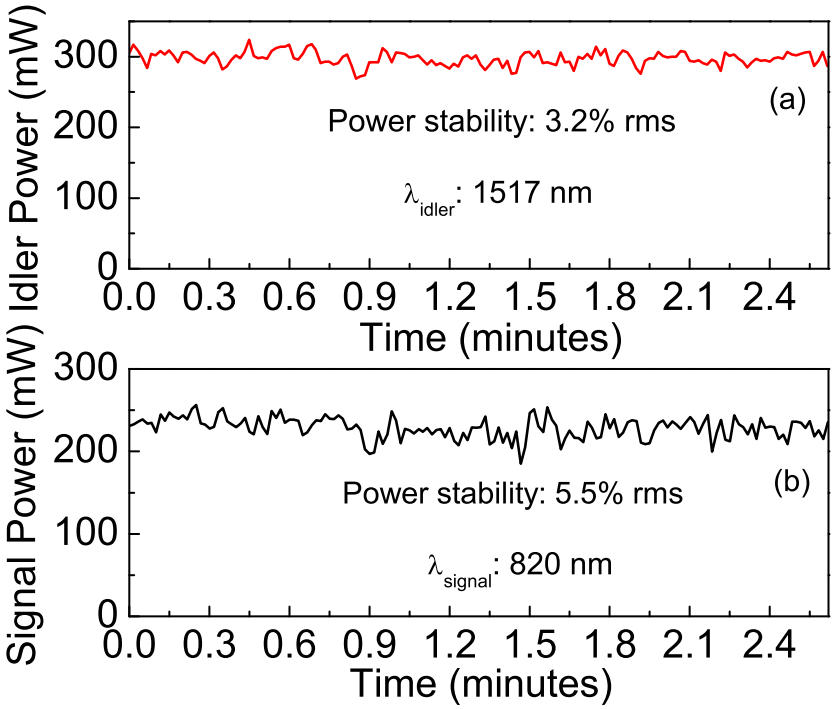


Figure 3.13: Passive power stability of the (a) idler output, and (b) extracted signal over 2.6 minutes.

bined with heating of the crystal at high pump powers >4.5 W. We recorded similar output power stability at a pump power of 4.5 W, which we attribute to temperature fluctuations in the crystal even at pump powers below 5.43 W, as also observed in the power scaling measurements up to 4.5 W of pump power. Further, we also monitored the OPO output power stability while keeping the OPO operating over a few hours, and we observed that the OPO remains stable for about ∼3 minutes, beyond which a sudden sharp fluctuation in powers is observed. However, after a few minutes, the output power becomes stable again and shows low fluctuations. The sudden fluctuation in output power under long-term

operation could be attributed to mechanical vibrations or air current changes in the laboratory.

### 3.3.3 Performance with time

In order to further investigate the temporal behaviour of OPO output power, we recorded the variation of signal and idler power with corresponding variation of pump power, while keeping the crystal under continuous exposure to pump in time. The results are shown in Fig. 3.14. As can be seen, while the pump power was kept constant for initial 5 seconds at 5.35 W, the idler power was observed

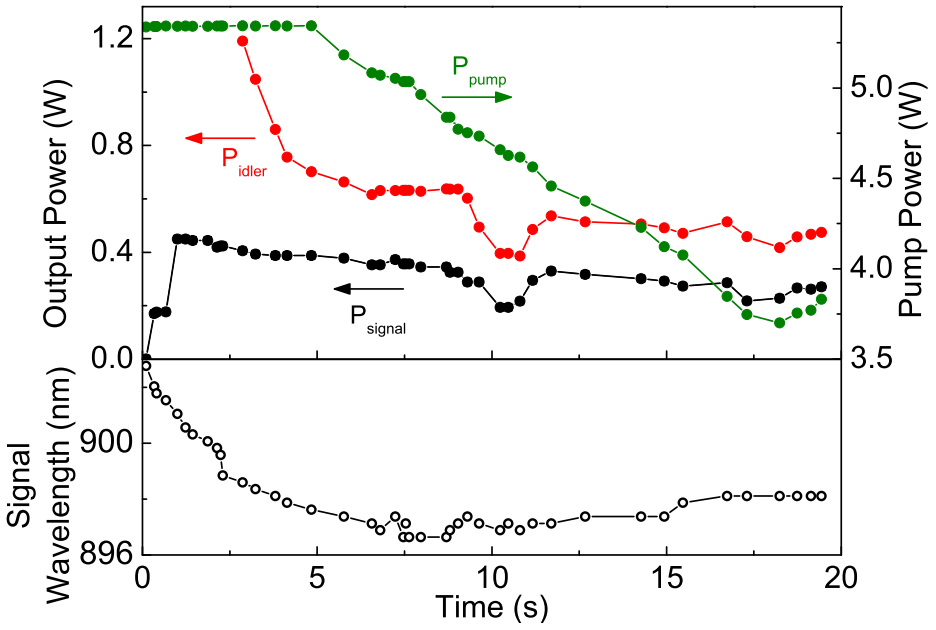


Figure 3.14: Variation of signal and idler power, and corresponding signal wavelength with time when the crystal is exposed to the varying pump power over initial time period of 20 seconds.

to decrease from 1.191 W to 702 mW, and the signal, after a sudden initial rise to 449 mW in 1 second drops to 388 mW in 5 seconds. The abrupt increase in signal power at exposure to pump power and subsequent drop in total OPO output power at a constant input power may be attributed to thermal lensing in the PPKTP crystal at high pump powers beyond 5 W. It is to be noted that while measuring the output power at sudden exposure to high pump power of 5.35 W, we observed thermal lag in the idler power detector, which could be due to sudden increase in the power onto the highly-sensitive thermal power sensor. This resulted in no idler power data for the first 2.8 seconds. After 5 seconds, by decreasing the pump power the OPO output power also begins to decrease to 193 mW in the signal and 386 mW in the idler at 4.6 W of pump power. With further decrease in the pump power, the thermal loading in the crystal becomes negligible and the signal and idler powers start to increase again, reaching more stable values of 330 mW and 537 mW, respectively, at 4.4 W of pump power. The signal and idler power is then observed to decrease gradually to 273 mW and 471 mW, respectively, with further decrease in pump power from 4.4 W to 4 W, beyond which, at low pump powers, the output power curves have similar behaviour as that of pump power. This behaviour indicates that thermal loading in the PPKTP crystal under exposure to green pump can be a limiting factor to OPO operation at high input powers above 4.5 W. However, improvements in the transmission loss of PPKTP (currently $\sim$10% at 532 nm) will enable stable and practical operation of the OPO at increased powers.

Also shown in Fig. 3.14 is the variation of signal wavelength with time under continuous exposure of the crystal to the varying pump power. As can be seen, the signal wavelength decreases over 5 nm, when the pump is kept constant at high

power of 5.35 W for the initial 5 seconds. This is due to the heating of the crystal at high pump power, which results in change in phase-matching temperature, as also noted in section 3.3.2, and observed in Fig. 3.12. The decrease in wavelength continues even when the pump power is gradually reduced to 4.6 W over next 10.8 seconds. By further decreasing the pump power below 4.6 W, the signal wavelength begins to increase again, due to the reduction in the temperature of the crystal at low pump powers. Similar behaviour was observed when the crystal was kept at a temperature of 50 °C.

### 3.3.4 Spectral characteristics

We further performed spectral characterization of OPO output using a confocal Fabry-Perot interferometer (FSR = 1 GHz, finesse = 400) at an input pump power of 5.2 W. The signal transmission spectrum at 831 nm is shown in Fig. 3.15, where an instantaneous linewidth of 7.5 MHz was measured, confirming single-frequency operation at room temperature. Similar behaviour was observed across the signal tuning range. We also investigated the frequency stability of the output signal using a wavemeter (HighFinesse, WS-U 30). The measurements were performed under free-running conditions, and in the absence of any thermal isolation. The results are shown in Fig. 3.16, where it can be seen that the signal exhibits a peak-to-peak frequency deviation of $\Delta\nu\sim$194 MHz over 37 seconds, measured at a central wavelength of 831.17005 nm. Figure 3.17 shows the signal spectrum across the tuning range at room temperature, measured using a spectrometer (Ocean Optics HR4000) at stable output powers. Given the detector sensitivity of the spectrometer across 190-1100 nm, we were not able to record the spectrum across the idler tuning range.

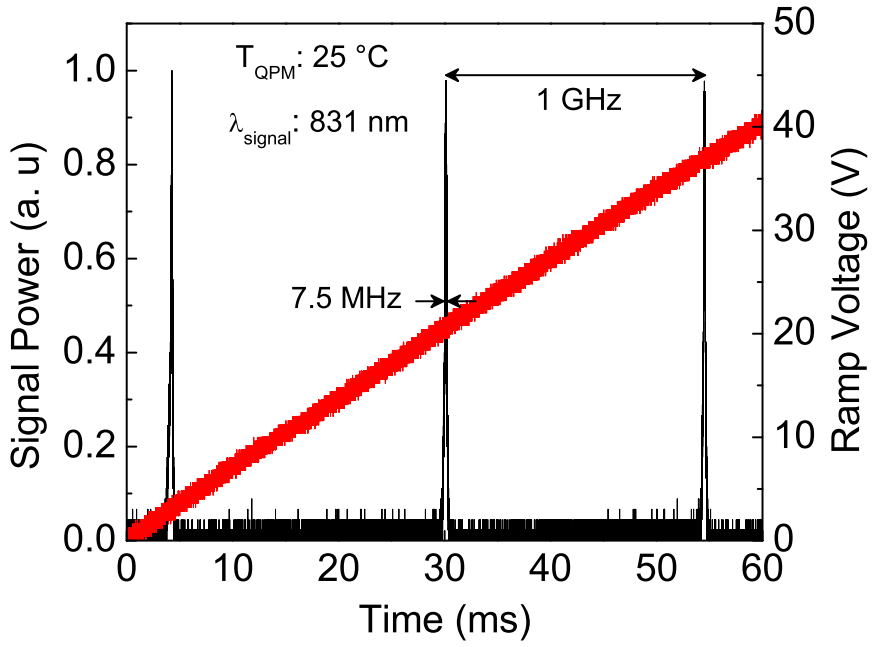


Figure 3.15: Single-frequency spectrum of the extracted signal at 831 nm.

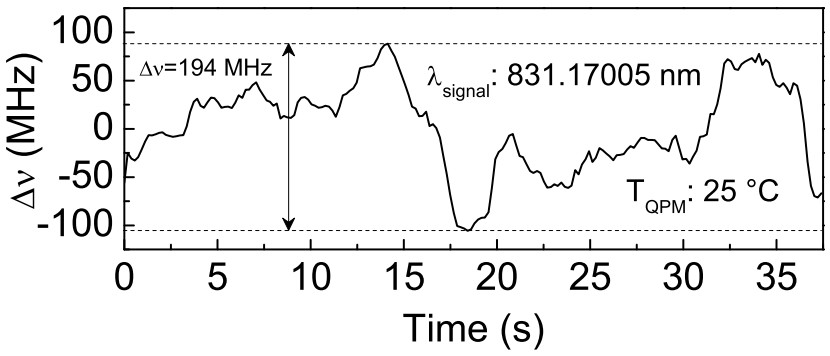


Figure 3.16: Frequency stability of the extracted signal beam at 831 nm.

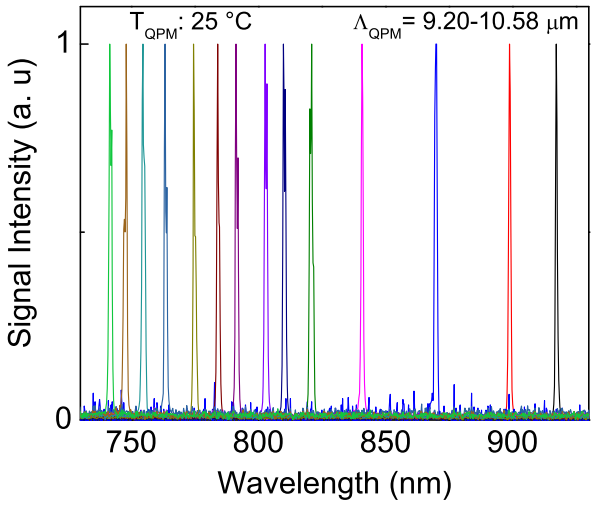


Figure 3.17: Signal spectra across the widely-tunable room temperature spectral range.

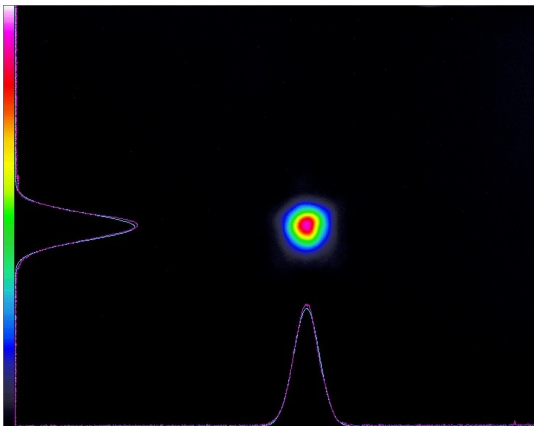

Figure 3.18: Far-field energy distribution of the extracted signal beam at 831 nm at room temperature.

### 3.3.5 Spatial beam profile

The far-field energy distribution together with orthogonal intensity profile of the signal beam at 831 nm obtained at maximum power is shown in Fig. 3.18. As can be seen, a Gaussian profile with circularity >95% was recorded, confirming high spatial beam quality.

## 3.4 SRO

In order to investigate the performance of the fanout PPKTP OPO under pure SRO configuration, we replaced the output coupling mirror, $M_4$ in Fig. 3.1, with a plane high reflector ($R$>99.8% over 620–1030 nm) for the signal, and characterized the OPO to understand its performance at high intracavity powers, with the results discussed below.

### 3.4.1 Wavelength tuning

As in the case of OC-SRO, wavelength tuning under pure SRO configuration could also be achieved by lateral translation of the PPKTP crystal to vary the QPM grating period or by changing the crystal temperature, while keeping either parameter fixed. With the OPO in SRO configuration, we initially varied the crystal position laterally while keeping the crystal at room temperature (22.4 ˚C), and recorded the signal wavelength for a pump power of 5.2 W. The signal wavelengths were recorded using a spectrometer (Ocean Optics HR4000), and the idler wavelengths were inferred from energy conservation. The generated signal and corresponding idler wavelengths as function of crystal position at room

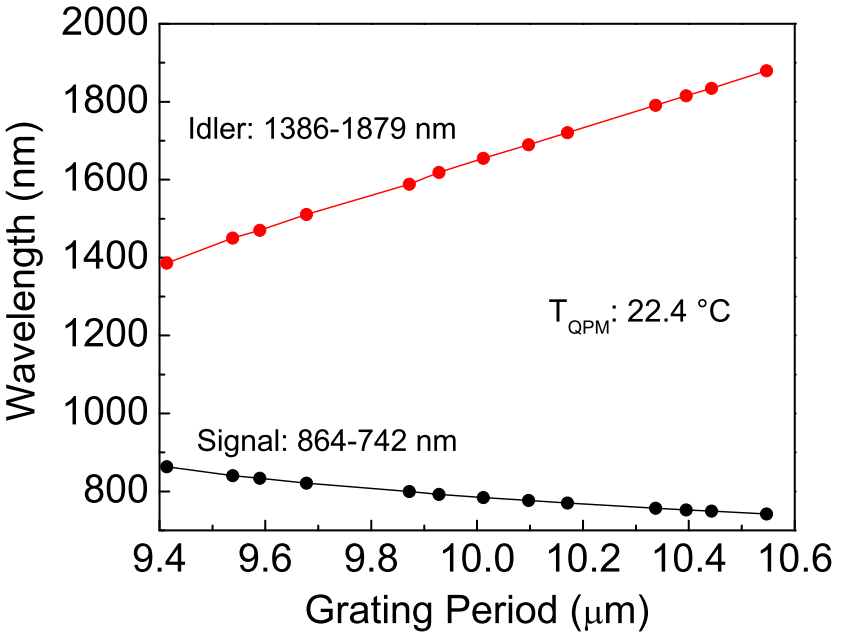


Figure 3.19: Signal and idler wavelength tuning range at room temperature in SRO configuration.

temperature are shown in Fig. 3.19. As evident, the OPO is rapidly and continuously tunable across 742-863 nm in signal and 1386-1879 nm in idler. The grating periods were calculated from measured wavelengths by using the relevant Sellemier equations [20]. As mentioned in section 3.3.1, we were able to use 8.08 mm of the crystal width as pump beam distortion was observed towards the edges of the crystal, which ceased OPO operation. To further extend the tuning range, we carried out grating tuning by keeping the crystal temperature fixed at 50 °C, with the results shown in Fig. 3.20. As evident, the OPO could be tuned across 745-908 nm in the signal, and 1284-1860 nm in the idler, thus demonstrating that using a fan-out grating at a fixed crystal temperature is an

efficient approach to achieve wide wavelength tunability. The idler output power across the room temperature tuning range, for a fixed pump power of 5.2 W is shown in 3.21(a). As can be seen, the maximum idler power recorded was 210 mw at 1588 nm, and >80 mW of output power over 62% of the tuning range was obtained. The idler output powers across the tuning range for grating tuning at 50 °C are shown in 3.21(b), where >200 mW of output power was measured over 48% of the tuning range, with the maximum idler power of 365 mW at 1284 nm. Wavelength tuning could also be achieved by varying the crystal temperature at a fixed crystal position. At a crystal position of 1.45 mm, corresponding to the calculated grating period of $\Lambda$=9.41 µm, signal tuning across 825-863 nm and

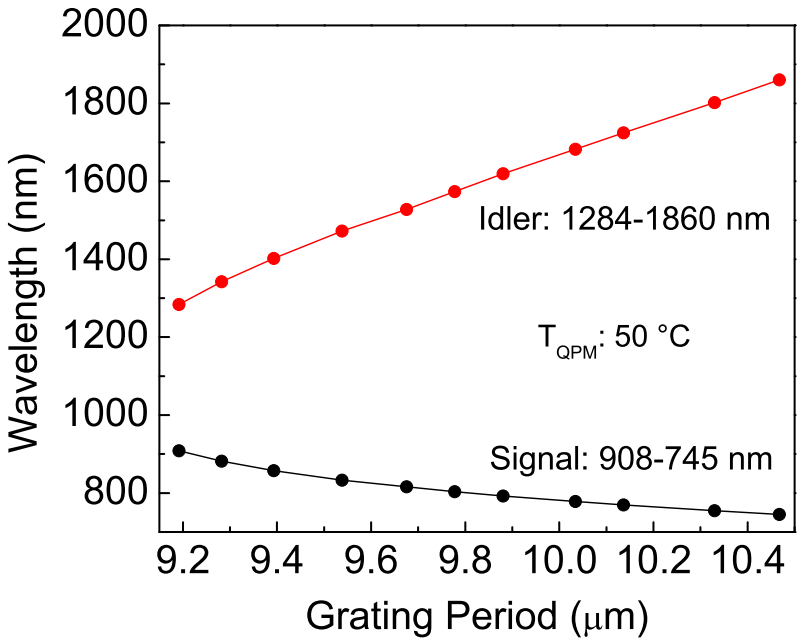


Figure 3.20: Signal and idler wavelength tuning range at T= 50 °C in SRO configuration.

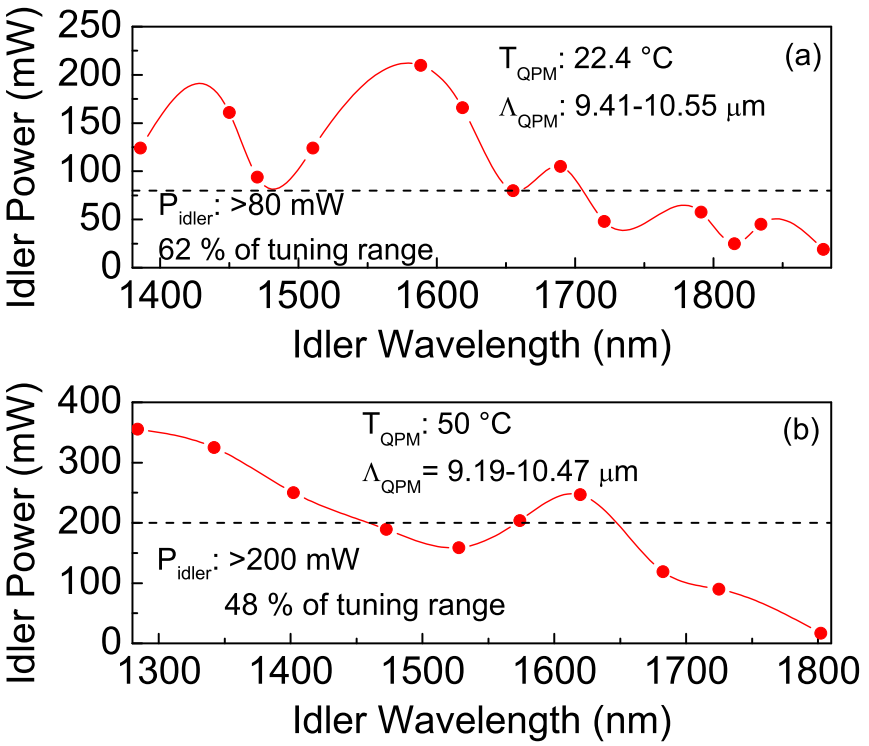


Figure 3.21: Idler output power across the grating tuning range at (a) room temperature, and (b) T=50 °C in SRO configuration.

idler tuning across 1385-1498 nm was obtained by heating the crystal from room temperature to 165 °C, as shown in Fig. 3.22. To achieve the shortest signal and the longest idler wavelength, we also carried out temperature tuning at the longest grating period of $\Lambda$=10.55 µm. By changing the crystal temperature from room temperature to 75 °C, the OPO could be tuned across 738-743 nm in the signal, and 1874-1910 nm in the idler, as shown in Fig. 3.23. However, as the OPO is tuned further away from degeneracy, the variation in the signal and idler wavelength with temperature is relatively small, due to the dispersion properties

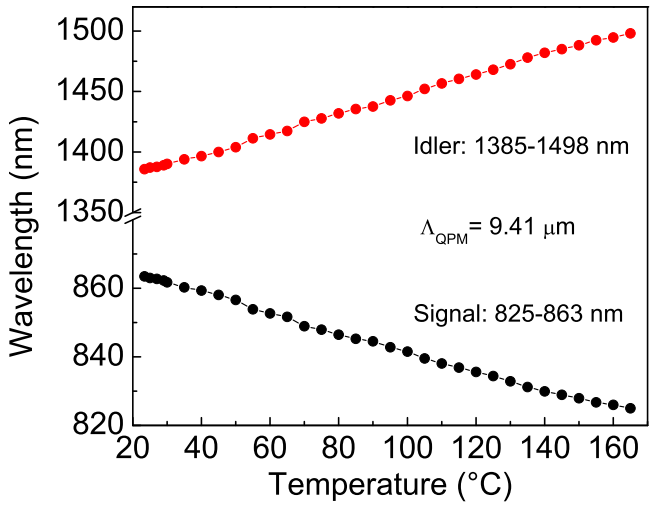


Figure 3.22: Temperature tuning at a fixed grating period of $\Lambda = 9.41$ μm in SRO configuration.

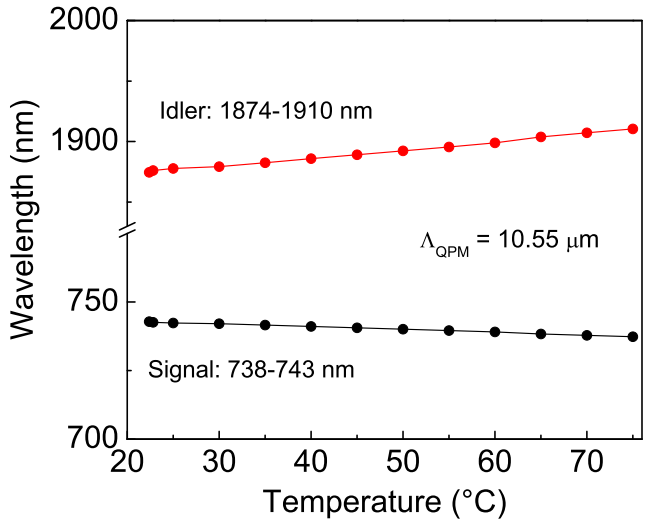


Figure 3.23: Temperature tuning at a fixed grating period of $\Lambda = 10.55$ μm in SRO configuration.

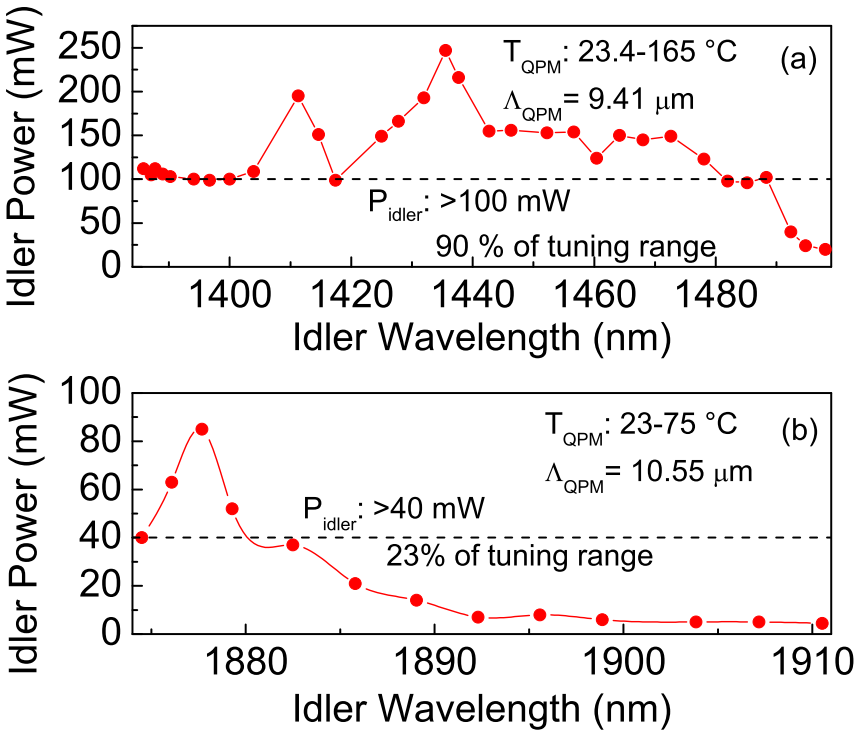


Figure 3.24: Variation of idler power across the temperature tuning range for grating period of (a) $\Lambda = 9.28$ µm, and (b) $\Lambda = 10.55$ µm in SRO configuration.

of PPKTP, as discussed before. The idler output power across the tuning range for $\Lambda$=9.41 µm is shown in Fig.3.24(a), where we measured >100 mW of idler output power over 90% of the tuning range, with maximum idler power of 247 mW at 1436 nm. The idler output power across the tuning range for $\Lambda$=10.55 µm is shown in Fig. 3.24(b). The maximum idler power recorded was 85 mW at 1878 nm, with >40 mW output power was obtained over 23 % of the tuning range. The drop in idler power at longer idler wavelengths in both grating tuning as well as temperature tuning is attributed to reduction in parametric gain away

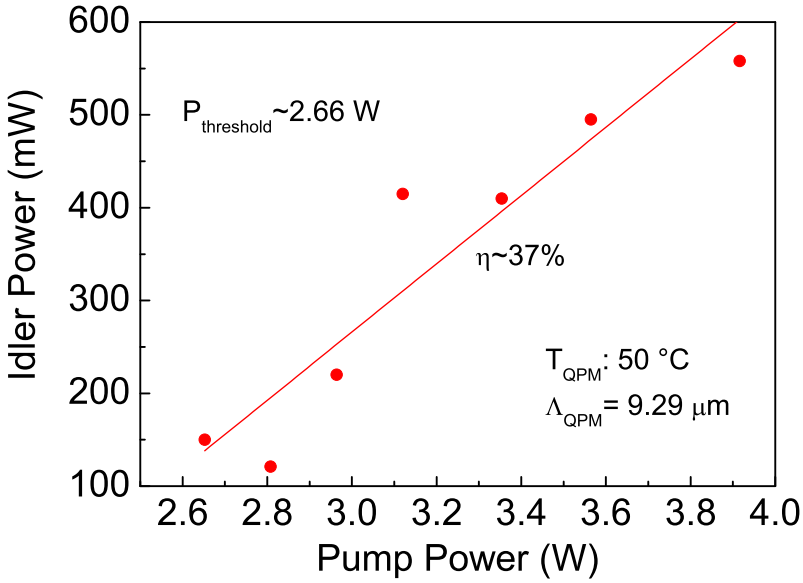


Figure 3.25: Idler output power as a function of pump power at T=50 ˚C in SRO configuration.

from degeneracy, along with the deterioration of pump beam observed at higher temperatures.

### 3.4.2 Power scaling and stability

To investigate the power scaling capability of the OPO in pure SRO configuration, we recorded the variation of output power with pump power, with the results shown in Fig. 3.25. The measurements were performed at 50 ˚C for a fixed grating period of $\Lambda = 9.29$ µm. As evident, the output power increases with pump power, displaying small sharp transitions as the pump power is increased, generating a maximum idler power of 558 mW for a pump power of 3.92 W. The threshold for SRO was recorded to be ∼2.66 W, slightly lower than of OC-

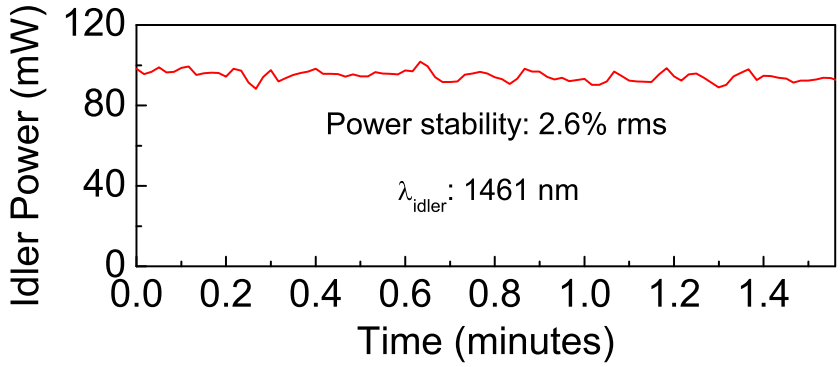


Figure 3.26: Passive power stability of the output idler in SRO configuration.

SRO. From the OC-SRO extracted power, we estimate the intracavity power in the pure SRO configuration to be of the order of ∼45 W. However, the overall extraction efficiency of the OPO under pure SRO configuration is lower than that of OC-SRO configuration. We also performed the power stability measurements of the output idler at 1461 nm, under free-running conditions for an input pump power of 3.1 W, with the results shown in Fig. 3.26. The crystal was kept at room temperature for these measurements. As can be seen, the idler exhibits a passive power stability better than 2.6% rms over 1.6 minutes. The long-term OPO output power stability behaviour was similar to that of OC-SRO configuration, discussed in section 3.3.2.

### 3.4.3 Spatial and spectral characteristics

We also recorded the far-field energy distribution along with the orthogonal intensity of the signal beam. The beam profile was recorded at the signal wavelength of 838 nm, shown in Fig. 3.28. As can be seen, the signal beam exhibits a

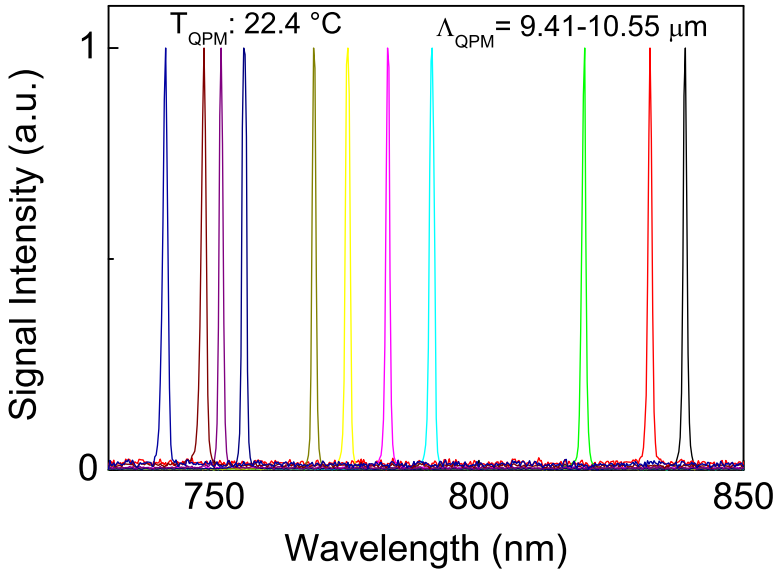


Figure 3.27: Some signal spectra across the room temperature tuning range in SRO configuration.

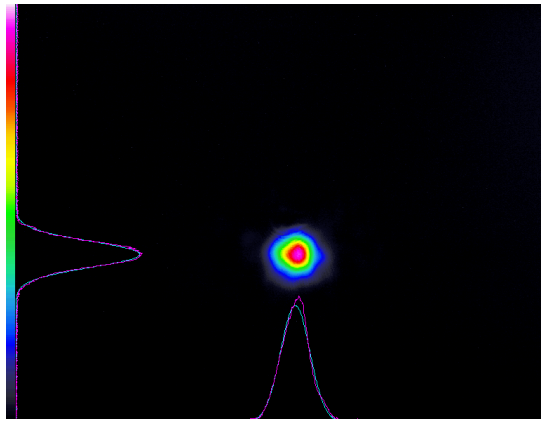

Figure 3.28: Far-field energy distribution of the signal beam at 838 nm.

Gaussian profile, with a circularity >93%, confirming high spatial beam quality. Similar beam profiles were observed across the signal tuning range. The signal spectra across the room temperature tuning range is shown in Fig. 3.27. As can be seen, the spectra across the tuning range in SRO configuration look similar to the spectra across the tuning range in OC-SRO configuration, shown in Fig. 3.17, as they are limited by the resolution of the spectrometer (0.5 nm).

## 3.5 Conclusion

We have demonstrated a cw OPO based on fan-out grating design PPKTP crystal at room temperature, providing wide and rapid wavelength tunability across 741-922 nm in signal and 1258-1884 nm in idler providing a maximum total power of 1.65 W, with >150 mW of extracted signal power over the entire tuning range and >400 mW of idler power over 66% of the tuning range. The idler and signal powers exhibit passive stability better than 3.2% rms and 5.5% rms, respectively, over 2.6 minutes. The OPO has single-frequency operation with good spatial beam quality. With improvements in the transmission loss of the PPKTP crystal in the green, proper thermal management and temperature control, the performance of the OPO in providing high and stable output powers can be further enhanced. In addition, the superior performance of the OPO in OC-SRO configuration compared to the pure SRO scheme suggests that further improvements in output power, stability, and power scaling can be obtained by optimization of output coupling and intracavity signal power.

# References

[1] C. W. Freudiger, W. Min, B. G. Saar, S. Lu, G. R. Holtom, C. He, J. C. Tsai, J. X. Kang, and X. S. Xie, "Label-Free Biomedical Imaging with High Sensitivity by Stimulated Raman Scattering Microscopy," Science **322**, 1857 (2008).
http://www.sciencemag.org/lookup/doi/10.1126/science.1165758

[2] M. Ebrahim-Zadeh, "Continuous-wave Optical Parametric Oscillators." in *Handbook of Optics* (OSA/McGraw-Hill, 2010), Vol. IV, chap. 17, third edn.

[3] M. Ebrahim-Zadeh, S. Chaitanya Kumar, and K. Devi, "Yb-Fiber-Laser-Pumped Continuous-Wave Frequency Conversion Sources from the Mid-Infrared to the Ultraviolet," IEEE Journal of Selected Topics in Quantum Electronics **20**, 350–372 (2014).
http://ieeexplore.ieee.org/document/6746032/

[4] U. Strössner, A. Peters, J. Mlynek, S. Schiller, J.-P. Meyn, and R. Wallenstein, "Single-frequency continuous-wave radiation from 0.77 to 1.73 µm generated by a green-pumped optical parametric oscillator with periodically poled $LiTaO_3$," Optics Letters **24**, 1602 (1999).
https://www.osapublishing.org/abstract.cfm?uri=ol-24-22-1602

[5] G. K. Samanta and M. Ebrahim-Zadeh, "Continuous-wave singly-resonant optical parametric oscillator with resonant wave coupling." Optics Express **16**, 6883–6888 (2008).
https://www.osapublishing.org/oe/abstract.cfm?uri=oe-16-10-6883

[6] S. Zaske, D.-H. Lee, and C. Becher, "Green-pumped cw singly resonant optical parametric oscillator based on MgO:PPLN with frequency stabilization to an atomic resonance," Applied Physics B **98**, 729–735 (2010).
http://link.springer.com/10.1007/s00340-009-3871-7

[7] K. Devi and M. Ebrahim-Zadeh, "Room-temperature, rapidly tunable, green-pumped continuous-wave optical parametric oscillator," Optics Letters **42**, 2635 (2017).
https://www.osapublishing.org/abstract.cfm?uri=ol-42-13-2635

[8] J. D. Bierlein and H. Vanherzeele, "Potassium titanyl phosphate: properties and new applications," Journal of the Optical Society of America B **6**, 622 (1989).
https://www.osapublishing.org/abstract.cfm?uri=josab-6-4-622

[9] A. Garashi, A. Arie, A. Skliar, and G. Rosenman, "Continuous-wave optical parametric oscillator based on periodically poled $KTiOPO_4$," Optics Letters **23**, 1739 (1998).
https://www.osapublishing.org/abstract.cfm?uri=ol-23-22-1739

[10] G. M. Gibson, M. Ebrahimzadeh, M. J. Padgett, and M. H. Dunn, "Continuous-wave optical parametric oscillator based on periodically poled $KTiOPO_4$ and its application to spectroscopy," Optics Letters **24**, 397–399 (1999).
https://www.osapublishing.org/abstract.cfm?uri=ol-24-6-397

[11] M. Ebrahimzadeh, G. A. Turnbull, T. J. Edwards, D. J. M. Stothard, I. D. Lindsay, and M. H. Dunn, "Intracavity continuous-wave singly resonant optical parametric oscillators," Journal of the Optical Society of America B **16**, 1499 (1999).
https://www.osapublishing.org/abstract.cfm?uri=josab-16-9-1499

[12] D. R. Weise, U. Strößner, A. Peters, J. Mlynek, S. Schiller, A. Arie, A. Skliar, and G. Rosenman, "Continuous-wave 532-nm-pumped singly resonant optical parametric oscillator with periodically poled $KTiOPO_4$," Optics Communications **184**, 329–333 (2000).
https://linkinghub.elsevier.com/retrieve/pii/S0030401800009500

[13] U. Strö$\beta$ner, J.-P. Meyn, R. Wallenstein, P. Urenski, A. Arie, G. Rosenman, J. Mlynek, S. Schiller, and A. Peters, "Single-frequency continuous-wave optical parametric oscillator system with an ultrawide tuning range of 550 to 2830 nm," Journal of the Optical Society of America B **19**, 1419 (2002). https://www.osapublishing.org/abstract.cfm?uri=josab-19-6-1419

[14] C. Liu, X. Guo, Z. Bai, X. Wang, and Y. Li, "High-efficiency continuously tunable single-frequency doubly resonant optical parametric oscillator," Applied Optics **50**, 1477 (2011).
https://www.osapublishing.org/abstract.cfm?uri=ao-50-10-1477

[15] G. Hansson, H. Karlsson, S. Wang, and F. Laurell, "Transmission measurements in KTP and isomorphic compounds," Applied Optics **39**, 5058 (2000). https://www.osapublishing.org/abstract.cfm?uri=ao-39-27-5058

[16] H. Karlsson and F. Laurell, "Electric field poling of flux grown $KTiOPO_4$," Applied Physics Letters **71**, 3474 (1997).
https://doi.org/10.1063/1.120363

[17] T. Y. Fan, C. E. Huang, B. Q. Hu, R. C. Eckardt, Y. X. Fan, R. L. Byer, and R. S. Feigelson, "Second harmonic generation and accurate index of refraction measurements in flux-grown $KTiOPO_4$," Applied Optics **26**, 2390 (1987).
https://www.osapublishing.org/abstract.cfm?uri=ao-26-12-2390

[18] W. Wiechmann, S. Kubota, T. Fukui, and H. Masuda, "Refractive-index temperature derivatives of potassium titanyl phosphate." Optics letters **18**, 1208–1210 (1993).
https://www.osapublishing.org/abstract.cfm?URI=ol-18-15-1208

[19] K. Fradkin, A. Arie, A. Skliar, and G. Rosenman, "Tunable midinfrared source by difference frequency generation in bulk periodically poled

$KTiOPO_4$," Applied Physics Letters **74**, 914–916 (1999).
http://aip.scitation.org/doi/10.1063/1.123408

[20] K. Kato and E. Takaoka, "Sellmeier and thermo-optic dispersion formulas for KTP," Applied Optics **41**, 5040 (2002).
https://www.osapublishing.org/abstract.cfm?uri=ao-41-24-5040

[21] S. Emanueli and A. Arie, "Temperature-dependent dispersion equations for $KTiOPO_4$ and $KTiOAsO_4$." Applied Optics **42**, 6661–6665 (2003).
https://www.osapublishing.org/ao/abstract.cfm?uri=ao-42-33-6661

# 4. Green-pumped nanosecond optical parametric oscillator based on MgO:cPPLT

This chapter is based on the following publication:

**Sukeert**, S. Chaitanya Kumar, and M. Ebrahim-Zadeh, "Green-pumped optical parametric oscillator based on fan-out grating periodically-poled MgO-doped congruent $LiTaO_3$," Optics Letters **44**, 5796 (2019).

## 4.1 Motivation

Tunable laser sources in different regions of the optical spectrum are of great interest for a variety of applications in spectroscopy, photochemistry, medical diagnostics, LIDAR, and material processing. Green-pumped optical parametric oscillators (OPOs) provide a viable approach for the generation of tunable radiation in the visible and near-infrared (near-IR). Such OPOs have been previously demonstrated by exploiting quasi-phase-matched (QPM) nonlinear crystals such as periodically-poled $LiNbO_3$ (PPLN), stoichiometric $LiTaO_3$ (sPPLT), and

$KTiOPO_4$ (PPKTP) [1–3]. Doping with MgO increases resistance to photorefractive damage and green-induced infrared absorption (GRIIRA) in $LiNbO_3$ and $LiTaO_3$, enabling green pumping of OPOs based on MgO-doped PPLN (MgO:PPLN) and sPPLT (MgO:sPPLT) [4, 5]. $LiTaO_3$ has a shorter absorption edge in the ultraviolet (UV) and lower nonlinear coefficient compared to $LiNbO_3$, making it suitable for QPM devices pumped by high-power laser sources [6]. In particular, MgO:sPPLT has proved to be the most viable QPM material for green-pumped OPOs due to a high photorefractive damage threshold [5, 7]. However, the stoichiometric composition, growth, and fabrication of this material continues to be challenging. Congruent $LiTaO_3$ (cLT), on the other hand, can be grown by a conventional Czochralski method. Doping with MgO improves material properties in cLT, such as increased optical damage resistance, transparency range, thermal conductivity, and lower coercive field for periodic poling, making it a potential candidate for high-power QPM devices [6, 8]. Because of the congruent composition, stable and mass production of MgO-doped cLT (MgO:cLT) is possible with large substrates and easier to fabricate than stoichiometric substrates, and so the material is now becoming increasingly available commercially [9]. Previous reports on OPOs based on periodically-poled cLT (cPPLT) include a 1.064 µm-pumped nanosecond OPO [10], a green-pumped nanosecond OPO [11], and a nanosecond OPO based on MgO:cPPLT pumped at 1.064 µm [12]. Wavelength tuning in all these QPM OPOs has been achieved by varying the crystal temperature, which is a slow process. Moreover, away from degeneracy, material dispersion in QPM crystals leads to a reduced tuning rate under temperature tuning, thus requiring relatively large temperature changes for small variations in the output wavelengths. Continuous and rapid wavelength tuning can be

| Material | 8 mol % MgO:cPPLT |
|---|---|
| Manufacturer | HC Photonics |
| Effective nonlinear coefficient | ∼9 pm/V |
| Transparency range | 0.27-5 µm [8] |
| Coercive field | 2.2 kV/mm [8] |
| Thermal Conductivity | 4.4 W/m-K [8] |

Table 4.1: Material properties of the nonlinear crystal used for the OPO.

achieved at a fixed temperature by using a fan-out grating structure, in which the grating period varies continuously across the lateral dimension of the crystal. This technique of grating tuning has already been deployed in a waveguide based on PPLN [13] and bulk OPOs based on MgO:PPLN, MgO:sPPLT, and PPKTP [14–16]. To generate wavelengths in the visible to near-IR, where short grating periods are required ($\Lambda \leq 10$ µm), there are significant challenges in QPM fabrication technology to provide the required fan-out grating designs over sufficient interaction length, thickness, and lateral dimension of the nonlinear crystal for wavelength tuning. While MgO:PPLN and MgO:sPPLT have been investigated for green-pumped OPOs, MgO:cPPLT has not been well studied. In this chapter, we describe what we believe to be the first green-pumped OPO based on MgO:cPPLT as the nonlinear material. Pumped at 532 nm by nanosecond pulses, the OPO can be continuously tuned across 689–1025 nm in the signal and 1134–2479 nm in the idler at room temperature by exploiting a fan-out grating structure in the crystal. We have achieved 131 mW of idler average power at 1476.5 nm for 1.8 W of pump power, with a passive stability of 3.9 % rms over 30 min at room temperature. By increasing the crystal temperature to 200 °C,

tuning range can be further extended to 677 nm in the signal and 2479 nm in the idler.

## 4.2 Experimental setup

The experimental setup for the green-pumped nanosecond MgO:cPPLT OPO is shown in Fig. 4.1. A Q-switched Nd:YAG laser at 1064 nm, which can deliver up to 30 W of average power at a 25 kHz pulse repetition rate, is externally frequency-doubled in a $LiB_3O_5$ (LBO) crystal, resulting in pulses with full-width-at-half-maximum (FWHM) duration of 7 ns at 532 nm that are used to pump the OPO. The green pump beam is separated from the fundamental by using two dichroic mirrors ($M_1$, $M_2$), which are highly reflecting at 532 nm and highly transmitting at 1064 nm. The green beam passes through a half-wave plate (HWP) and a polarizing beam-splitter (PBS) for power attenuation, with a second HWP used to control the input polarization for optimum QPM interaction in the crystal. A photograph of the experimental setup is shown in Fig. 4.2. The pump beam is focused to a beam waist radius of $w_0 \sim 120$ µm inside the crystal using a lens ($L_3$). The OPO is configured in a compact linear cavity comprising two plane mirrors ($M_3$, $M_4$), with a physical cavity length of 31 mm. The mirrors are highly reflecting ($R$ >99.8%) for the signal (620–1030 nm), and highly transmitting ($T$ >97%) for the idler (1078–3550 nm) and pump, SRO configuration for the signal. The 8 mol% MgO:cPPLT crystal is 29-mm-long, 15-mm-wide, and 0.5-mm-thick, and has a fan-out grating structure with QPM periods varying continuously over $\Lambda$ = 7.75–10.25 µm across the lateral dimension. Some material properties of this crystal are listed in Table 4.1. The end faces of the crystal are antireflection-

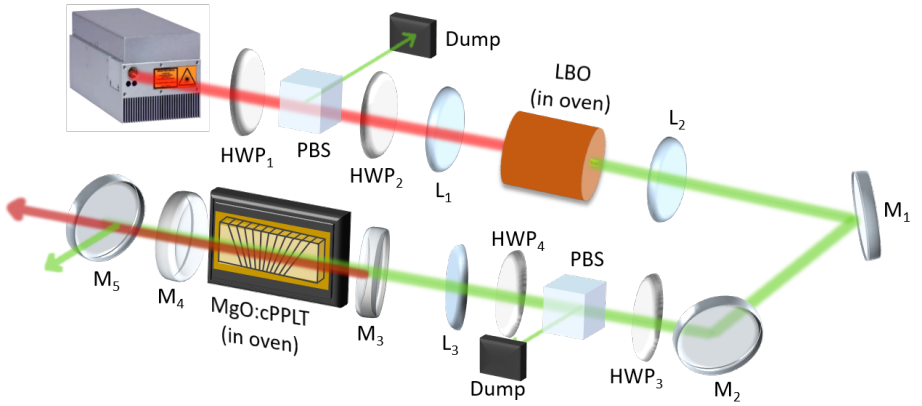


Figure 4.1: Experimental setup of the green-pumped nanosecond OPO based on MgO:cPPLT. HWP, half-wave plate; PBS, polarizing beam splitter; L, lens; M, mirrors.

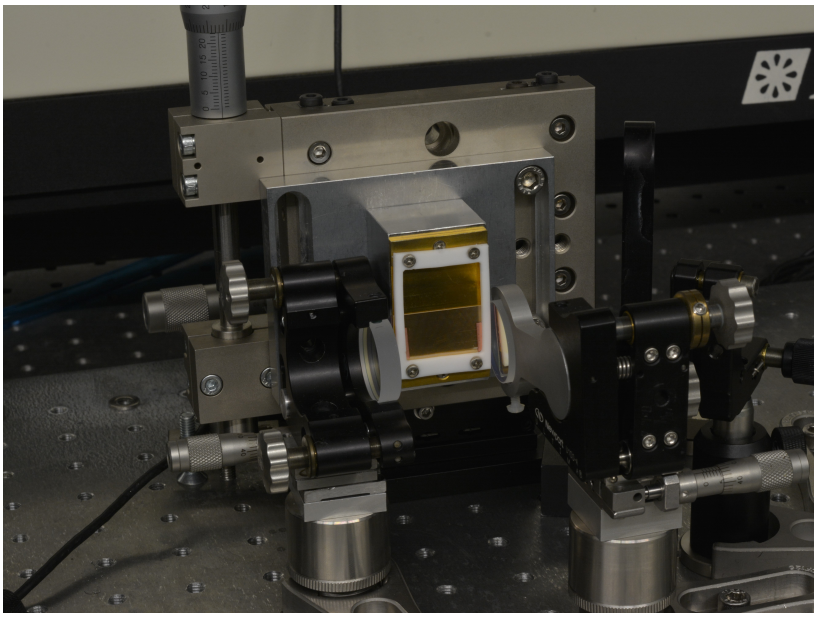

Figure 4.2: Laboratory photograph of the cavity of the MgO:cPPLT nanosecond OPO.

coated at 532 nm ($R$ <1%) and 700–1000 nm ($R$ <1%), with high transmission over 1130–2200 ($T$ >80%). The crystal is mounted on a linear translation stage with a resolution of 10 µm to enable smooth grating tuning across its lateral dimension. To further investigate the temperature tuning characteristics of the OPO, the crystal is also housed in an oven, adjustable from room temperature to 200 °C, with a stability of ± 0.1 °C. The physical length of the OPO cavity in this case was increased to 72 mm, limited by the dimensions of the oven, while maintaining the focusing condition.

## 4.3 Results and discussion

### 4.3.1 Wavelength tuning

Wavelength tuning in the present OPO can be achieved by lateral translation of the MgO:cPPLT crystal across the pump beam to vary the QPM grating period or by changing the crystal temperature, while keeping either parameter fixed. Initially, we investigated the tuning capabilities of the OPO at room temperature (22.5 °C), by varying the crystal position laterally to continuously change the QPM grating period. The results are shown in Fig. 4.3, where the signal wavelengths were measured using a spectrometer (Ocean Optics HR4000), the idler wavelengths were inferred from energy conservation, and the grating periods were theoretically calculated from the measured wavelengths by using relevant Sellmeier equations [9]. By varying the crystal position, and correspondingly the grating period over $\Lambda$ = 7.94–10.27 µm, and at an average pump power of 1.35 W, we were able to tune the OPO across 689–1025 nm in the signal and 1106–2336 nm in the idler. The idler average power across the tuning range at

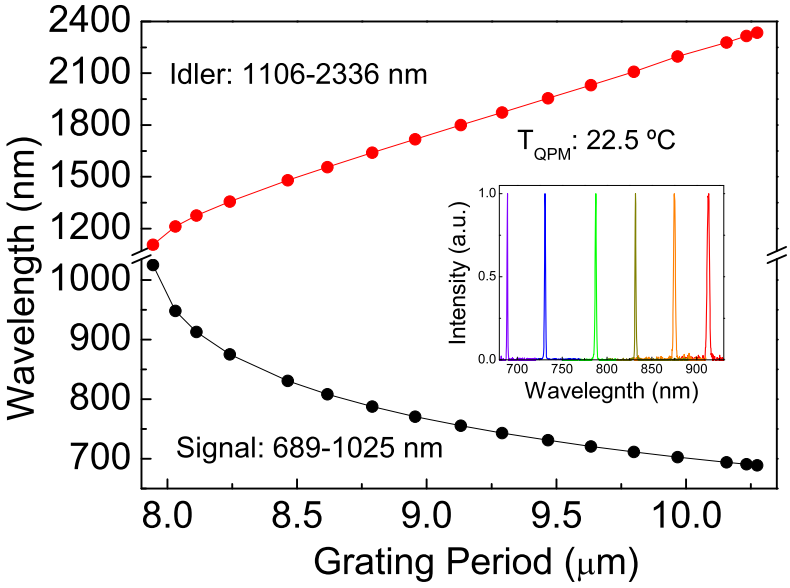


Figure 4.3: Room-temperature tuning range of the green-pumped nanosecond MgO:cPPLT OPO. Inset: measured signal spectra across the tuning range.

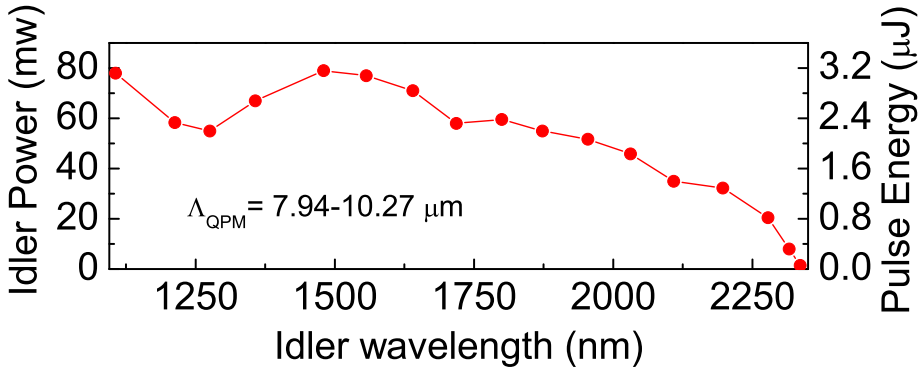


Figure 4.4: Idler average power across the tuning range of the MgO:cPPLT nanosecond OPO while operating at room temperature.

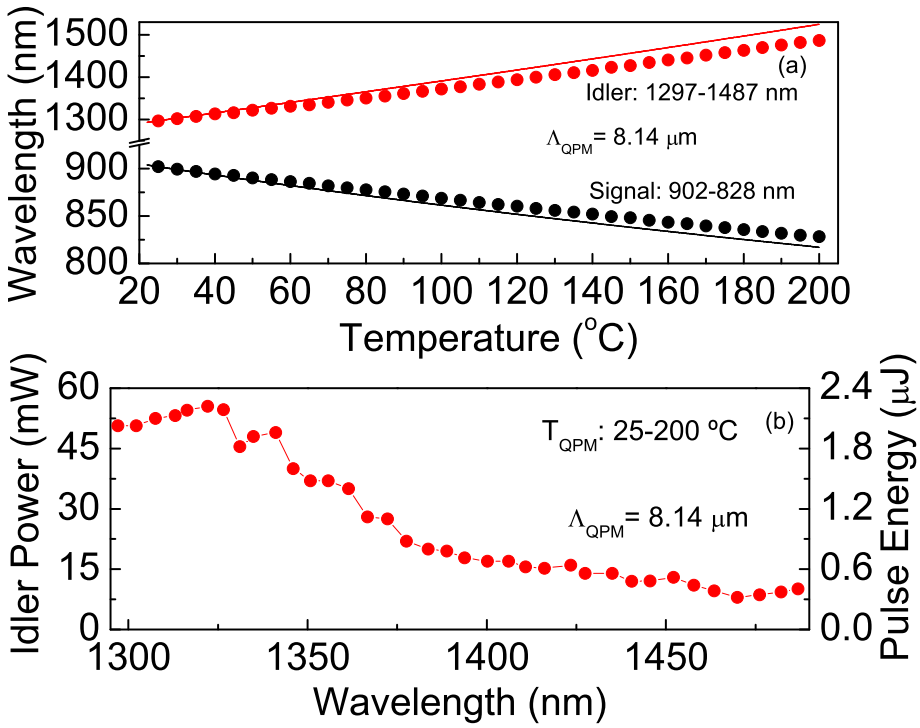


Figure 4.5: (a) Temperature tuning, and (b) variation of idler power across the tuning range for the short grating period of $\Lambda = 8.14$ µm.

room temperature is shown in Fig. 4.4. The idler power varies from 78 mW at 1106 nm to 1.5 mW at 2336 nm, with the highest average power of 79 mW recorded at 1480 nm. We also studied the temperature tuning characteristics of the OPO at a fixed grating period of $\Lambda = 8.14$ µm. By varying the crystal temperature from 25 °C to 200 °C, we were able to tune the OPO across 828–902 nm in the signal and 1297–1487 nm in the idler, as shown in Fig. 4.5(a), together with the theoretical calculations using the relevant Sellmeier equations [9]. The measured output power across the idler tuning range is shown in Fig. 4.5(b).

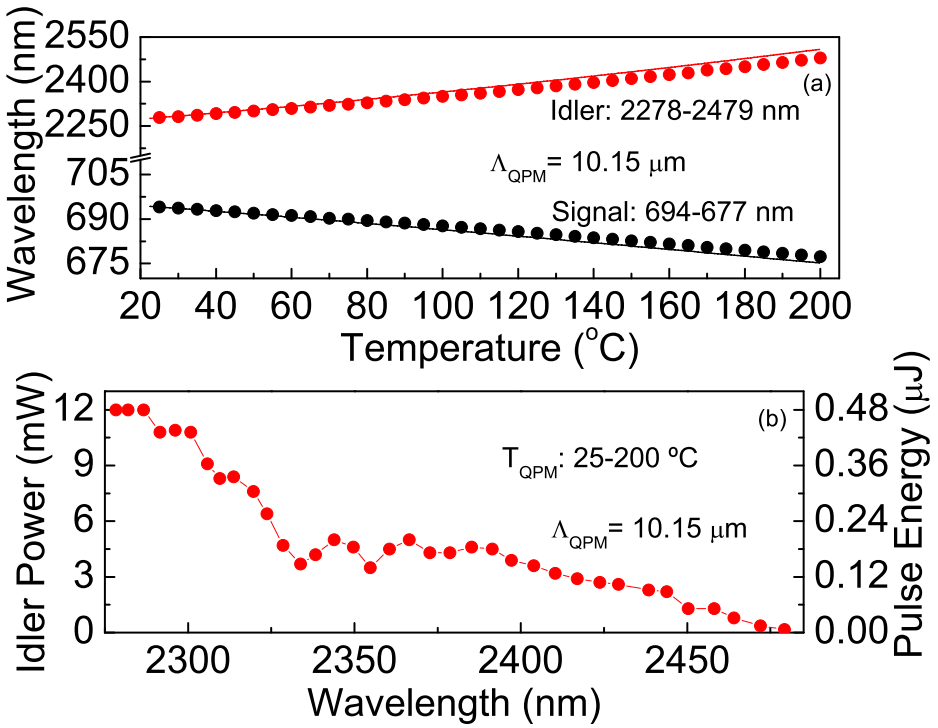


Figure 4.6: (a) Temperature tuning, and (b) variation of idler power across the tuning range for the long grating period of $\Lambda = 10.15$ µm.

The idler power varies from 51 mW at 1297 nm to 10 mW at 1487 nm, with a maximum of 55 mW at 1322 nm. To generate the shortest wavelength, we performed temperature tuning for nearly the longest grating period, at $\Lambda = 10.15$ µm, with the results shown in Fig. 4.6. In this case, the OPO could be tuned across 677–694 nm in the signal by varying the crystal temperature from 25 °C to 200 °C, with the corresponding idler tunable over 2278–2479 nm, as shown in Fig. 4.6(a). Also shown in Fig. 4.6(a) is the theoretically calculated temperature tuning data using the relevant Sellmeier equations [9]. The idler power varies

from 12 mW at 2278 nm to 0.16 mW at 2479 nm, as shown in Fig. 4.6(b). At higher temperatures, we observed some scattering of the pump beam inside the crystal. The lower idler output power across the tuning range under temperature tuning in Figs. 4.5(b) and 4.6(b), compared to that under grating tuning at fixed room temperature in Fig. 3, is due to the longer cavity length imposed by the dimensions of the oven, resulting in increased rise time loss for the OPO. The drop in idler power at longer wavelengths is attributed to the reduction in parametric gain further away from degeneracy.

### 4.3.2 Power scaling

We also performed power scaling measurements of the OPO at an idler wavelength of 1476.5 nm, while also simultaneously monitoring the temperature of the crystal. The results are shown in Fig. 4.7. Each data point was obtained after a 15 seconds exposure to pump for the crystal to reach a stable temperature, and each power value was averaged over 15 seconds. The crystal was also allowed to return to room temperature before each measurement. As evident from the plot, the idler output power increases almost linearly with a slope efficiency of ∼11.3 %, reaching 131 mW for an input pump power of 1.8 W, with evidence of saturation of idler output power at higher pump powers above ∼1 W. Beyond ∼ 1.8 W of input average power, we observed optical damage toward the output facet of the crystal, thus limiting power scaling to higher pump powers. In addition, we observed optical damage formation through appearance of a spot under long-term exposure at input powers above ∼ 1.4 W, as shown in the inset of Fig. 4.9. This corresponds to a pulse energy of 56 µJ and fluence of 0.12 J/cm$^2$ at 532 nm. To identify the origin of the damage, we carried out transmission measurements of

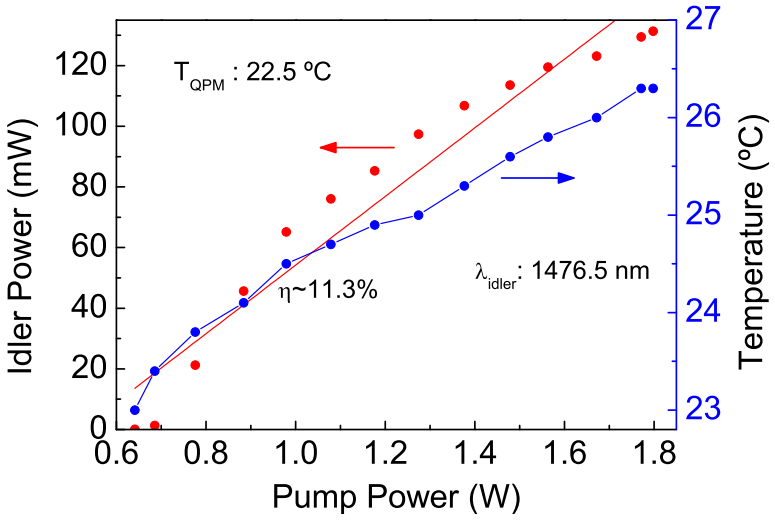


Figure 4.7: Idler average power scaling as a function of pump power for the MgO:cPPLT nanosecond OPO.

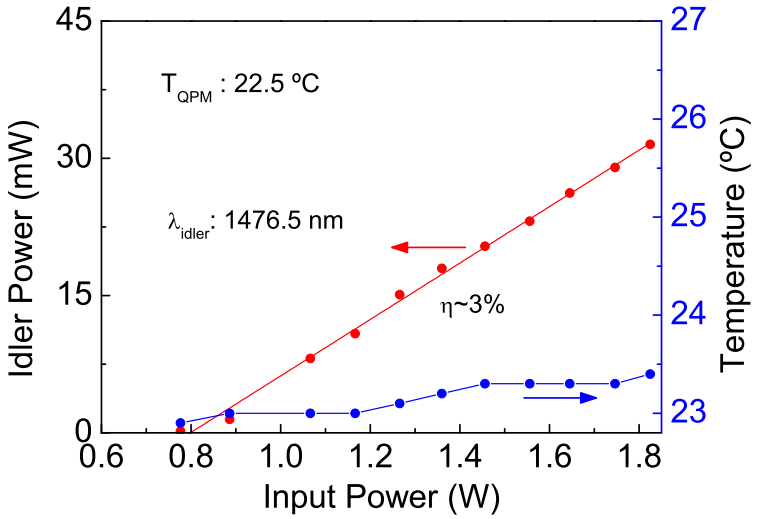


Figure 4.8: Idler power scaling as a function of pump power modulated by a chopper for the MgO:cPPLT nanosecond OPO. Note: Pump power was measured before the chopper.

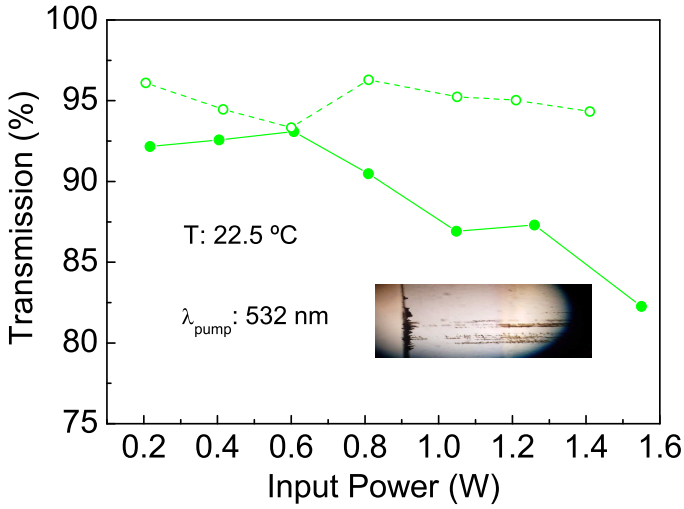


Figure 4.9: Transmission of the crystal at the pump wavelength as a function of the input pump power. Solid circles represent phase-matched polarization, while hollow circles denote polarization orthogonal to phase-matched polarization. Inset: Picture of crystal after long term operation at high pump powers.

the crystal for the pump at 532 nm in linear polarization corresponding to optimum phase-matching as well as polarization orthogonal to the phase-matched direction, with the results shown in Fig. 4.9. For the case of phase-matched polarization, the transmission was found to be 93% up to 0.6 W of input power, decreasing to $\sim$ 82% at an input power of 1.55 W, causing the onset of damage in the crystal. On the other hand, for polarization of the pump orthogonal to the phase-matched direction, we measured a transmission >94 % even at 1.4 W. We have previously observed similar polarization-dependent transmission behavior in PPKTP [16]. As can also be seen in Fig. 4.7, the temperature of the crystal rises with increasing pump power. To investigate the role of thermal effects in the observed saturation of OPO output power, we repeated the power scaling mea-

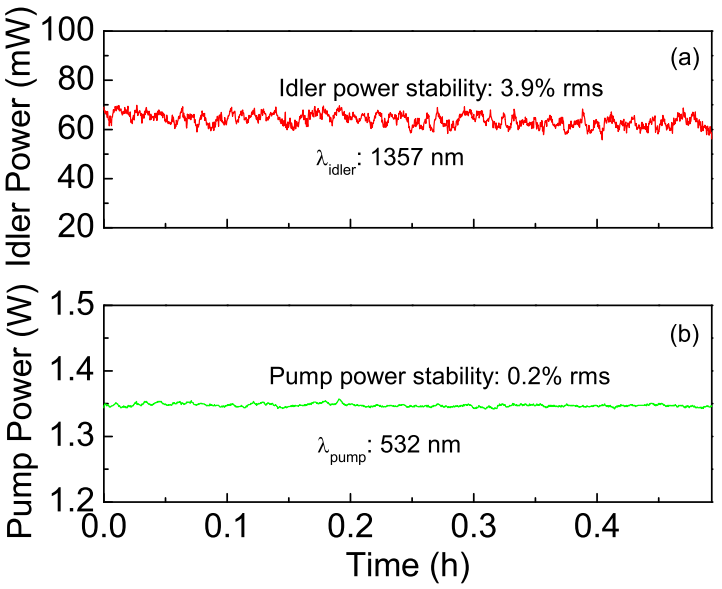


Figure 4.10: Power stability of the (a) idler output from the MgO:cPPLT nanosecond OPO, and (b) pump over 30 min.

surements after modulating the pump power using a mechanical chopper (500 Hz, 50% duty cycle, 0.94 ms time window). Under this condition, we observed that the output power scaled linearly with input power up to the maximum 1.8 W, as seen in Fig. 4.8, with only a small rise in the crystal temperature, thus confirming thermal effects as the cause of the saturation of output power at higher pump powers.

### 4.3.3 Power stability

We further carried out long-term power stability measurements of the output idler at 1357 nm, at an average pump power of 1.35 W at room temperature,

with the results shown in Fig. 4.10(a). The idler power from the OPO exhibits a passive stability of 3.9 % rms with a mean value of 63.8 mW over $\sim$ 30 min. For comparison, the power stability of the input green pump is displayed in Fig. 4.10(b), showing a fluctuation of 0.2% rms over the same period.

### 4.3.4 Spatial and temporal characteristics

The idler output beam, measured at a wavelength of 1495 nm and at a distance of $\sim$15 cm from the OPO output using a pyroelectric camera, is shown in Fig. 4.11. As can be seen, the beam has a Gaussian profile, with a circularity >98%, confirming high spatial quality. Temporal measurements of the OPO output signal pulses together with the input pump pulses were also performed by using a fast Si detector with 150 ps rise time and 2 GHz bandwidth (Thorlabs, DET025 A/M) and a digital oscilloscope with a bandwidth of 3.5 GHz. The results are shown in Fig. 4.12. The measurements were performed at room temperature for a grating period of $\Lambda$ = 8.24 µm, corresponding to a signal wavelength of 875 nm. As can be seen, the generated signal pulses have a duration of 6.5 ns, shorter than the input pump pulses of 7 ns duration, typical of pulsed nanosecond OPOs. The periodic modulation in the pump pulse, also seen in the signal pulse profile, is due to longitudinal mode beating in the pump laser. It should be noted that the temporal pulse profiles presented in Fig. 4.12 have been averaged over many shots.

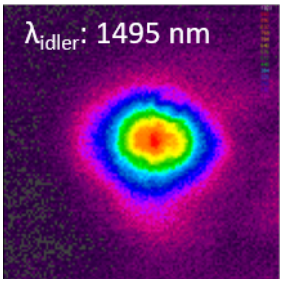


Figure 4.11: Idler beam profile from the OPO.

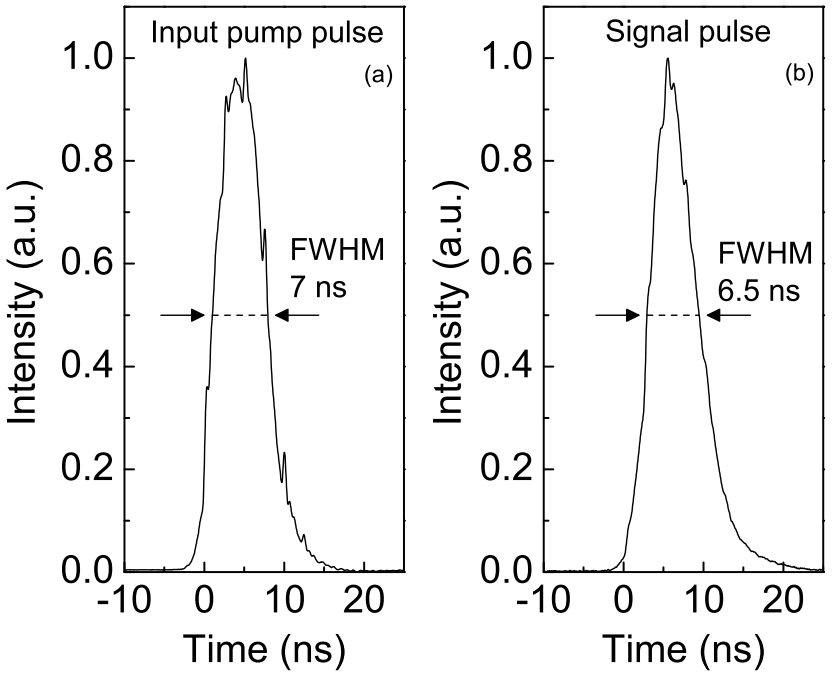


Figure 4.12: Temporal profile of the (a) pump pulse at 532 nm, and (b) signal pulse at 875 nm.

## 4.4 Conclusion

In conclusion, we have demonstrated what is to our knowledge the first green-pumped OPO based on MgO:cPPLT. Pumped by 7 ns pulses at 532 nm at 25 kHz, the OPO generates continuously tunable radiation across 677–1025 nm in the signal and 1106–2479 nm in the idler, with rapid and continuous tuning made possible across 689–1025 nm in the signal and 1106–2336 nm in the idler at a fixed temperature by using a fan-out grating structure. The continuous tuning range can be further extended to shorter signal and longer idler wavelengths by exploiting longer grating periods in the fan-out grating design in the MgO:cPPLT crystal and using the same green pumping scheme. The OPO has been shown to provide idler average powers of up to 131 mW at 1476.5 nm for a pump power of 1.8 W, with power stability better than 3.9% rms over 30 minutes. The signal pulses at 875 nm have typical duration of 6.5 ns, shorter than the pump pulses of 7 ns, as expected. We have observed bulk damage in the crystal for pump powers above ∼1.8 W. Damage in the crystal was also observed under long-term operation for pump powers above ∼1.4 W. Because of the easier growth and fabrication of the congruent material, coupled with the advantages of $LiTaO_3$ over $LiNbO_3$ for green pumping, MgO:cPPLT could be an attractive alternative for OPOs operating in the visible and near-IR. Long-term OPO operation and transmission measurements of the crystal suggest early onset of optical damage at low average powers and poor bulk quality of the present sample currently limit power scaling of the OPO. Improvements in the growth and fabrication of crystals with higher optical quality, better uniformity, and a larger aperture size of the grating layer are expected to lead to further enhancements in the

performance of green-pumped OPOs based on MgO:cPPLT. This will further enable the widespread use of this crystal as a viable candidate for the development of OPOs in the visible and near-IR, where alternative nonlinear materials for green pumping are not readily available.

# References

[1] V. Pruneri, J. Webjörn, P. S. J. Russell, and D. C. Hanna, "532 nm pumped optical parametric oscillator in bulk periodically poled lithium niobate," Applied Physics Letters **67**, 2126 (1995).
http://aip.scitation.org/doi/10.1063/1.114741

[2] S.-Y. Tu, A. H. Kung, Z. D. Gao, and S. N. Zhu, "Efficient periodically poled stoichiometric lithium tantalate optical parametric oscillator for the visible to near-infrared region," Optics Letters **30**, 2451 (2005).
https://www.osapublishing.org/abstract.cfm?uri=ol-30-18-2451

[3] V. Pasiskevicius, H. Karlsson, F. Laurell, R. Butkus, V. Smilgevicius, and A. Piskarskas, "High-efficiency parametric oscillation and spectral control in the red spectral region with periodically poled $KTiOPO_4$," Optics Letters **26**, 710 (2001).
http://www.osapublishing.org/abstract.cfm?uri=ol-26-10-710

[4] I.-H. Bae, H. S. Moon, S. Zaske, C. Becher, S. K. Kim, S.-N. Park, and D.-H. Lee, "Low-threshold singly-resonant continuous-wave optical parametric oscillator based on MgO-doped PPLN," Applied Physics B **103**, 311 (2011).
http://link.springer.com/10.1007/s00340-010-4297-y

[5] S.-Y. Tu, A. H. Kung, Z. D. Gao, S. N. Zhu, S. Kurimura, and K. Kitamura, "Green-pumped high-power optical parametric oscillator based on periodically poled MgO-doped stoichiometric $LiTaO_3$," Optics Letters **31**, 3632 (2006).
https://www.osapublishing.org/abstract.cfm?uri=ol-31-24-3632

[6] H. Ishizuki and T. Taira, "Mg-doped congruent $LiTaO_3$ crystal for large-aperture quasi-phase matching device," Optics Express **16**, 16 963 (2008).
https://www.osapublishing.org/oe/abstract.cfm?uri=oe-16-21-16963

[7] G. K. Samanta, G. R. Fayaz, Z. Sun, and M. Ebrahim-Zadeh, "High-power, continuous-wave, singly resonant optical parametric oscillator based on MgO:sPPLT," Optics Letters **32**, 400 (2007).
https://www.osapublishing.org/abstract.cfm?uri=ol-32-4-400

[8] H. Ishizuki and T. Taira, "Characterization of 8 mol % Mg-doped congruent $LiTaO_3$ for high-energy quasi-phase matching device," in *Advanced Solid-State Lasers Congress* p. AM4A.15 (2013).
https://www.osapublishing.org/abstract.cfm?uri=ASSL-2013-AM4A.15

[9] K. Moutzouris, G. Hloupis, I. Stavrakas, D. Triantis, and M.-H. Chou, "Temperature-dependent visible to near-infrared optical properties of 8 mol % Mg-doped lithium tantalate," Optical Materials Express **1**, 458 (2011).
https://www.osapublishing.org/ome/abstract.cfm?uri=ome-1-3-458

[10] T. Hatanaka, K. Nakamura, T. Taniuchi, H. Ito, Y. Furukawa, and K. Kitamura, "Quasi-phase-matched optical parametric oscillation with periodically poled stoichiometric $LiTaO_3$." Optics letters **25**, 651 (2000).
https://www.osapublishing.org/ol/abstract.cfm?uri=ol-25-9-651

[11] V. Sharma, S. C. Kumar, A. Aadhi, H. Ye, G. K. Samanta, and M. Ebrahim-Zadeh, "Tunable vector-vortex beam optical parametric oscillator," Scientific Reports **9**, 1 (2019).
https://www.nature.com/articles/s41598-019-46016-y

[12] H. Ishizuki and T. Taira, "High energy quasi-phase matched optical parametric oscillation using Mg-doped congruent $LiTaO_3$ crystal," Optics Express **18**, 253 (2010).
https://www.osapublishing.org/oe/abstract.cfm?uri=oe-18-1-253

[13] Y. Ishigame, T. Suhara, and H. Nishihara, "$LiNbO_3$ waveguide second-harmonic-generation device phase matched with a fan-out domain-inverted

grating," Optics Letters **16**, 375 (1991).
https://www.osapublishing.org/abstract.cfm?uri=ol-16-6-375

[14] A. Henderson and R. Stafford, "Low threshold, singly-resonant CW OPO pumped by an all-fiber pump source," Optics Express **14**, 767 (2006).
https://www.osapublishing.org/abstract.cfm?uri=oe-14-2-767

[15] K. Devi and M. Ebrahim-Zadeh, "Room-temperature, rapidly tunable, green-pumped continuous-wave optical parametric oscillator," Optics Letters **42**, 2635 (2017).
https://www.osapublishing.org/abstract.cfm?uri=ol-42-13-2635

[16] K. Devi, A. Padhye, Sukeert, and M. Ebrahim-Zadeh, "Widely tunable room-temperature continuous-wave optical parametric oscillator based on periodically-poled $KTiOPO_4$," Optics Express **27**, 24 093 (2019).
https://www.osapublishing.org/abstract.cfm?uri=oe-27-17-24093

# 5. Green-pumped continuous-wave optical parametric oscillator based on fan-out grating MgO:PPLN

This chapter is based on the following publication:
**Sukeert**, S. Chaitanya Kumar, and M. Ebrahim-Zadeh, "Green-pumped continuous-wave parametric oscillator based on fanout–grating MgO:PPLN," Optics Letters **45**, 6486 (2020).

## 5.1 Motivation

Tunable continuous-wave (cw) single-frequency light sources are of interest for a diverse range of applications, from spectroscopy and trace gas sensing to biomedicine [1]. In particular, OPOs pumped in the green represent an attractive approach for the generation of tunable visible and the near-infrared (near-IR) radiation. Because of the small parametric gain available under low pump intensities in the

cw regime, practical operation of cw OPOs relies almost exclusively on quasi-phase-matched (QPM) nonlinear materials [2], exploiting the highest nonlinear tensor coefficients combined with long interaction lengths under non-critical phase-matching (NCPM). Such cw OPOs have been previously demonstrated using well-established oxide-based QPM nonlinear materials [3–5]. However, detrimental photorefractive effect and green-induced infrared absorption (GRIIRA) have hampered further development of green-pumped cw OPOs based on periodically-poled $LiNbO_3$ (PPLN) and $LiTaO_3$ (PPLT), while strong thermal effects hinder the performance of green-pumped OPOs based on $KTiOPO_4$ (PPKTP). These deleterious effects have been significantly alleviated by doping with MgO in PPLN and PPLT, enabling development of cw green-pumped OPOs based on MgO-doped PPLN (MgO:PPLN) [6–10] and stoichiometric PPLT (MgO:sPPLT) [11–13]. The growth and fabrication of MgO:sPPLT, however, remains challenging, resulting in limited availability of this material. On the other hand, because of a mature growth and poling technology, together with high nonlinearity, MgO:PPLN can now be readily fabricated in multi-grating as well as fanout grating designs for the development of near-IR to mid-IR cw OPOs pumped at ∼1.064 µm. Such OPOs are now well established, providing widely tunable radiation from ∼1.45 to ∼4 µm at watt-level powers [14, 15]. However, as a material with different linear and nonlinear optical properties compared to MgO:sPPLT and PPKTP, MgO:PPLN presents a different set of challenges for the development of green-pumped cw OPOs. Previous reports of cw green-pumped OPOs based on MgO:PPLN include singly-resonant oscillators (SROs) for the signal [6–9] and idler [10] in linear [6, 8, 9] as well as ring [7, 10] cavity configurations using uniform grating structures. Such OPOs deploy single- or

multi-grating crystal designs, where wavelength tuning is typically achieved by changing the temperature of the nonlinear crystal. This significantly reduces the wavelength tuning rate in these crystals, particularly away from degeneracy, where material dispersion requires relatively large change in the phase-matching temperature for a small variation in the output wavelength. Under these circumstances, using fanout structures in which the grating period varies continuously across the lateral dimension of the crystal, provides continuous and rapid wavelength tuning at a fixed temperature. However, the development of green-pumped OPOs for the generation of visible to near-IR wavelengths require short grating periods ($\Lambda \leq 10$ µm), which present significant challenges in the fabrication of QPM structures in a fanout design with a large enough length and clear aperture. Nevertheless, with progress in QPM crystal growth and fabrication technology, the use of fanout grating designs has already been demonstrated in green-pumped cw OPOs based on MgO:sPPLT and PPKTP [16, 17]. However, to the best of our knowledge, such OPOs based on fanout grating MgO:PPLN have not been previously demonstrated. In this chapter, we describe the first green-pumped cw OPO based on fan-out grating MgO:PPLN, continuously tunable over 813–1032 nm in the signal and 1098–1539 nm in the idler at a fixed temperature, by simple mechanical translation of the crystal across its lateral dimension. Moreover, by deploying signal output coupling, we demonstrate simultaneous extraction of useful output in both parametric waves at a total external efficiency of 30%, with maximum signal powers up to 339 mW and idler powers up to 400 mW across the tuning range.

## 5.2 Green-pumped cw OPO based on MgO:PPLN

### 5.2.1 Experimental setup

The schematic of the experimental setup for the green-pumped cw OPO based on fan-out grating MgO:PPLN is shown in Fig. 5.1. The pump source is a cw frequency-doubled Nd:$YVO_4$ laser (Coherent Verdi V10) delivering up to 10 W of output power at 532 nm in a single-frequency, linearly polarized beam with $M^2 < 1.1$. The nonlinear crystal for the OPO is 25-mm-long, 12-mm-wide, and 0.5-mm-thick 5 mol% MgO:PPLN, incorporating a fanout grating structure with a continuously varying period over $\Lambda$ = 6.9-8.1 µm across its lateral dimension. Some material properties of this crystal are listed in Table 5.1. Unlike previous reports on green-pumped cw OPOs which deployed 40–50 mm crystals [6–10], here we use a relatively short interaction length of 25 mm. Owing to the 15 times higher linear absorption coefficient of MgO:PPLN at 532 nm compared to 1064 nm [18], the use of shorter crystal minimizes thermal loading due to green pumping, thereby enabling stable long-term operation with excellent beam qual-

| Material | 5 mol % MgO:PPLN |
|---|---|
| Manufacturer | HC Photonics |
| Effective nonlinear coefficient | ∼16 pm/V [19] |
| Transparency range | 0.3-5 µm [20] |
| Coercive field | 3.7 kV/mm [20] |
| Thermal Conductivity | 4.6 W/m-K [19] |

Table 5.1: Material properties of the nonlinear crystal used for the OPO.

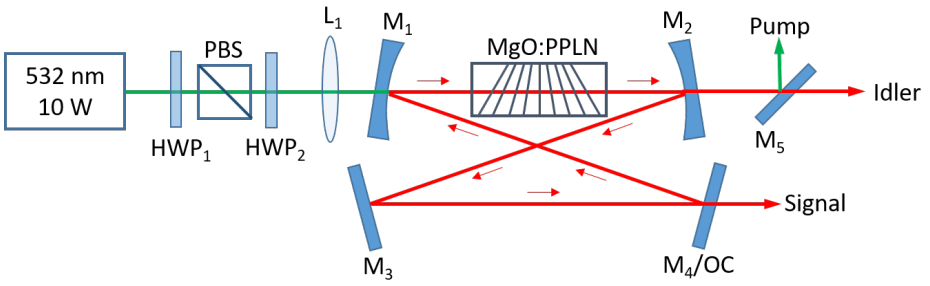


Figure 5.1: Configuration of green-pumped fanout–grating MgO:PPLN cw OPO. HWP, half-wave-plate; PBS, polarizing beam-splitter; L, lens; M, mirrors; OC, output coupler.

ity. The crystal faces are antireflection (AR)-coated at 532 nm ($R$ <1%) and 750–1060 nm ($R$ <1%), and over 1060–1850 nm ($R$ <2%). The crystal is housed in an oven with temperature stability of ± 0.01 °C and mounted on a motorized linear translation stage with a resolution of 0.1 µm to enable fine and continuous grating tuning across its lateral dimension. The OPO is configured in a compact ring cavity comprising two plano-concave mirrors, $M_1$ and $M_2$ ($r$=100 mm), and two plane mirrors, $M_3$-$M_4$. $M_4$ can also be replaced with a plane output coupler (OC). Before implementation of the OPO, we measured the transmission of the MgO:PPLN crystal to be $T$∼93% at the pump wavelength for $e$-polarization, as shown in Fig. 5.2, corresponding to type-0 ($e \rightarrow ee$) QPM parametric interaction. Given the many practical challenges that are required to be overcome to make a cw SRO operational, especially in the green-pumped regime, we decided to initially construct a doubly-resonant oscillator (DRO), for ease of operation, alignment and optimisation, and then eventually transform the DRO into a SRO configuration.

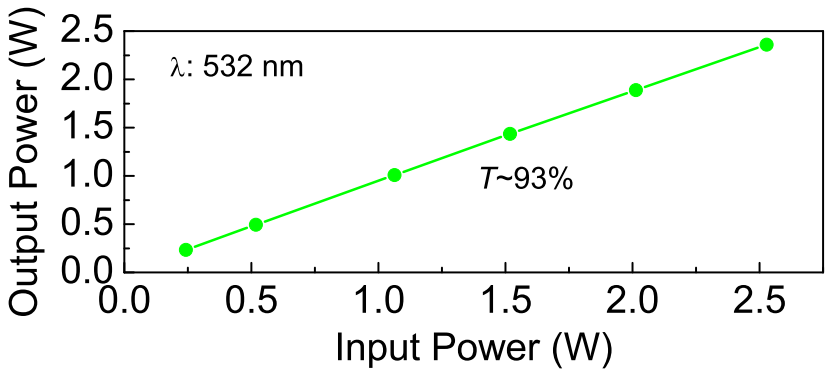


Figure 5.2: Transmission of MgO:PPLN crystal at 532 nm in the phase-matched polarisation.

### 5.2.2 MgO:PPLN DRO

For the DRO, all mirrors ($M_1$-$M_4$) were highly reflecting ($R$>99.8%) over 850-1200 nm for signal and idler, and highly transmitting at the pump wavelength. The pump beam was focussed using a $f$=175 mm lens to a waist radius of $w_{0p}$ ~35 µm initially at the center of the crystal. Once the DRO was operational, we carried out wavelength tuning by changing the temperature of the crystal at a fixed grating period as well as varying the grating period at fixed temperature to assess the functionality of our nonlinear crystal. After optimising the 4-mirror ring cavity, we began transforming the DRO into a SRO.

### 5.2.3 MgO:PPLN SRO

To transform the DRO into a SRO, we replaced $M_4$ with another mirror that was highly reflecting ($R$>99.8%) over 620-1030 nm for the signal, and highly transmitting ($T$>97%) across 1078-3550 nm for the idler and at 532 nm for the

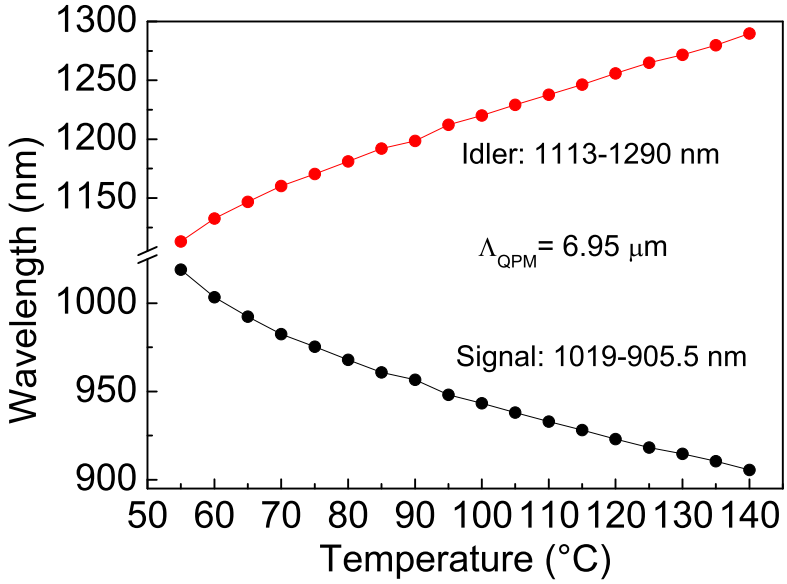


Figure 5.3: Temperature tuning at a fixed grating period of $\Lambda = 6.95$ µm using all highly reflecting mirrors.

pump, ensuring SRO operation in the signal. Once the cavity was carefully and properly aligned and the OPO was operational, the remaining mirrors, $M_3$, $M_2$, and $M_1$ were also replaced with SRO mirrors. We started the characterization of the OPO, and wavelength tuning could be achieved at a fixed temperature by varying the grating period, or by changing the crystal temperature at a fixed grating period, as shown in Fig. 5.3. The signal wavelengths were measured using a spectrometer (Ocean Optics HR4000), the idler wavelengths were infered from energy conservation, and the grating period was estimated from the measured wavelength using the Sellemeier equations of the material [21]. At a fixed grating period of $\Lambda = 6.95$ µm (calculated from the measured signal wavelength by using Sellmeier equations), by varying the crystal temperature from 55 to 140 °C, we

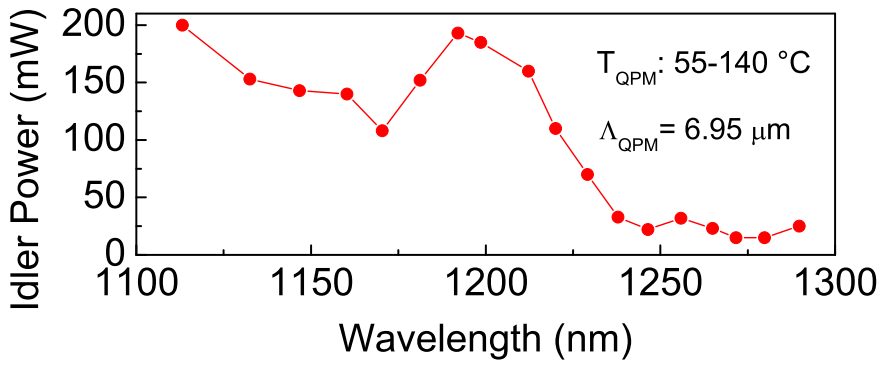


Figure 5.4: Idler power across the temperature tuning range using all highly reflecting mirrors.

were able to tune the OPO across 905.5–1019 nm in the signal, and correspondingly over 1290–1113 nm in the idler. The temperature tuning rate of the OPO for the signal wavelength is ∼1.3 nm/°C. The idler power across the temperature tuning range is shown in Fig. 5.4. The idler power varies from a maximum of 200 mW at 1113 nm to 25 mW at 1290 nm. During the process of optimisation, we noticed that if an aperture placed in the path of the pump beam before the lens was slightly closed, it led to an increase in output power, and improvement in power stability, especially when operating away from degeneracy, as shown in Figs. 5.5 and 5.6. At a temperature of 55 °C, the idler average output power at the wavelength of 1219 nm increased from ∼135 mW with a stability of 3.43% rms over 16 minutes when the aperture was open, to ∼225 mW with a stability of 3.84% rms over 16 minutes when the aperture was closed, as shown in Fig. 5.5. The change in the idler output power and stability was even more drastic at a longer wavelength of 1411 nm, as seen in Fig. 5.6, where the output power and stability over 16 minutes changed from ∼2.5 mW and 25.8% rms, respectively,

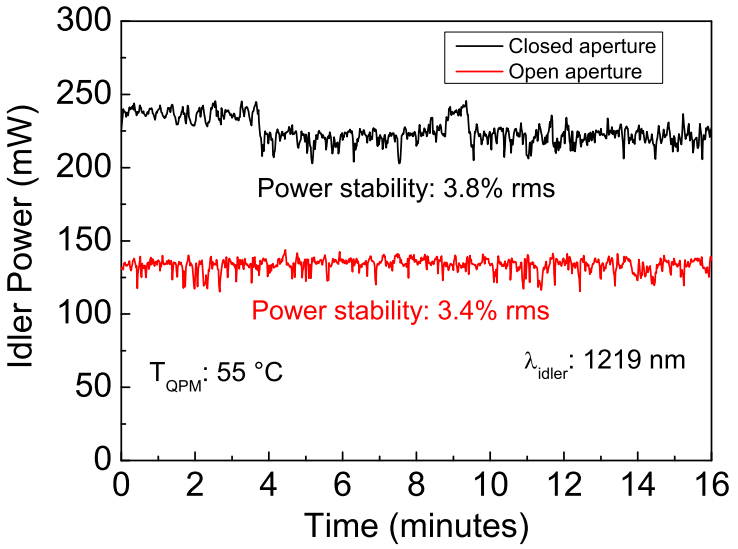


Figure 5.5: Change in idler output power when the aperture is open and closed at the idler wavelength of 1219 nm while using all highly reflecting mirrors.

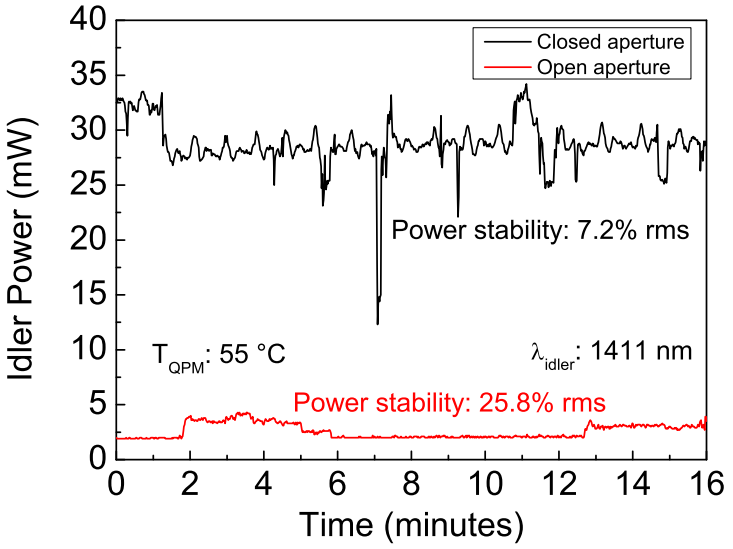


Figure 5.6: Change in idler output power when the aperture is open and closed at the idler wavelength of 1411 nm using all highly reflecting mirrors.

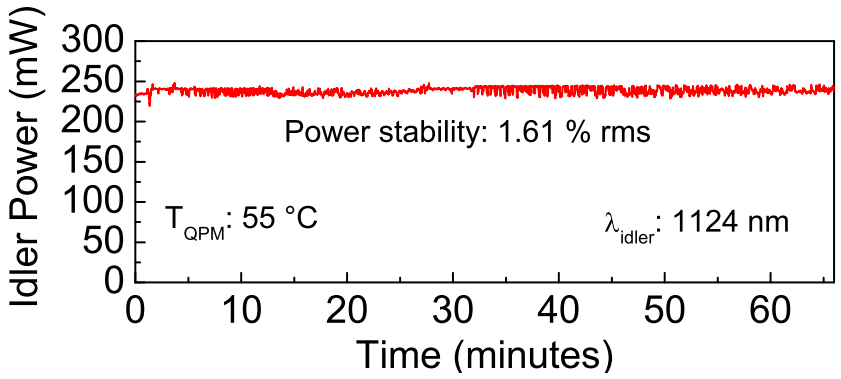


Figure 5.7: Passive power stability of idler after increasing the pump beam waist, using all highly reflecting mirrors.

when the aperture was open, to ∼28 mW and 7.23% rms, respectively, when the aperture was closed. After removing the crystal, we measured the pump beam waist again and found that the previously mentioned beam waist radius of $w_{0p}$ ∼35 µm, when the aperture was open, would change by about 10 µm to a beam waist radius of $w_{0p}$ ∼45 µm when the aperture was closed. This improvement in output average power and stability when the aperture is closed was attributed to the relaxation of the focussing condition upon slightly closing the aperture, leading to optimisation of thermal lens and improved mode-matching in the cavity. Following this observation, the $f$=175 mm lens was replaced with a $f$=200 mm lens, which resulted in a beam waist radius of $w_{0p}$ ∼45 µm, with a corresponding focussing parameter of $\xi_p$ ∼0.47. Changing the focussing condition led to a significant improvement in OPO output power stability, as shown in Fig. 5.7, where the idler at the wavelength of 1124 nm exhibits a passive power stability better than 1.61% rms over >1 hour. In order to extract useful signal power, and optimize the OPO performance, the plane mirror $M_4$ was replaced with a

plane output coupler with variable transmission ($T$=1-2%) across 720–1000 nm. This was the final experimental configuration of the OPO, and in order to avoid catastrophic damage to the crystal, we limited the pump power below 2.5 W for all measurements. This corresponds to a pump intensity of 39.3 kW/cm$^2$ in the MgO:PPLN crystal.

## 5.3 Results and discussion

### 5.3.1 Wavelength tuning

As mentioned earlier, wavelength tuning in our green-pumped cw OPO can be performed by temperature tuning for a fixed grating period or by continuously varying the fanout grating period of the MgO:PPLN crystal at a constant temperature. We characterized the tuning capabilities of the OPO at a fixed crystal temperature of 55 °C by varying the crystal position laterally across the pump beam to continuously change the QPM grating period. The results are shown in Fig. 5.8. The black data points represent the signal wavelengths, measured using a spectrometer (Ocean Optics HR4000), while the red dots represent the corresponding idler wavelengths, inferred from energy conservation. The grating periods were estimated from the measured wavelengths by using relevant Sellmeier equations [21]. By varying the lateral position of the fanout crystal to change the grating period over $\Lambda$ = 6.9-8.1 µm, we were able to tune the OPO across 813–1032 nm in the signal and 1539–1098 nm in the corresponding idler, as shown in Fig. 5.9. Compared to the temperature tuning range of 905.5–1019 nm in the signal and correspondingly 1290–1113 nm in the idler, resulting in a temperature tuning rate of ∼1.3 nm/°C as mentioned in section 5.2.3, a crystal

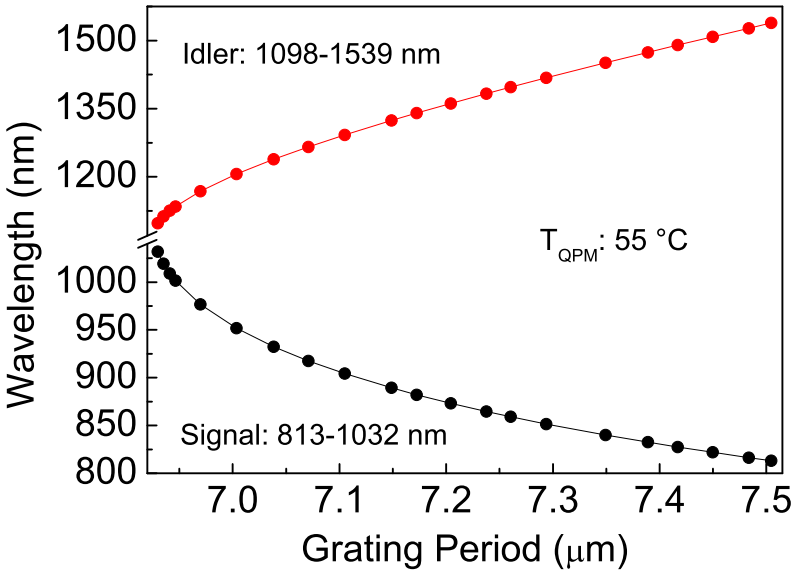


Figure 5.8: Signal and idler wavelength tuning range of the green-pumped cw OPO as a function of the MgO:PPLN fanout grating period at a fixed temperature of 55 °C.

translation of only ∼1.5 mm can provide identical wavelength coverage at a fixed temperature of 55 °C. On the other hand, tuning over the entire OPO operating range can be achieved by translating the crystal over ∼5.15 mm. The OPO can be tuned across 813–1032 nm in ∼2 seconds, while it requires >1 minute for the output power to reach a steady state. Hence, the fanout grating design can provide rapid tuning at a fixed temperature compared to temperature tuning with a uniform grating period, which requires several minutes to cover the same wavelength range. The simultaneously generated signal and idler powers across the OPO tuning range for a maximum input pump power of 2.4 W are shown in Fig. 3. The signal power varies from 278 mW at 1032 nm to 48 mW at 813 nm, with a

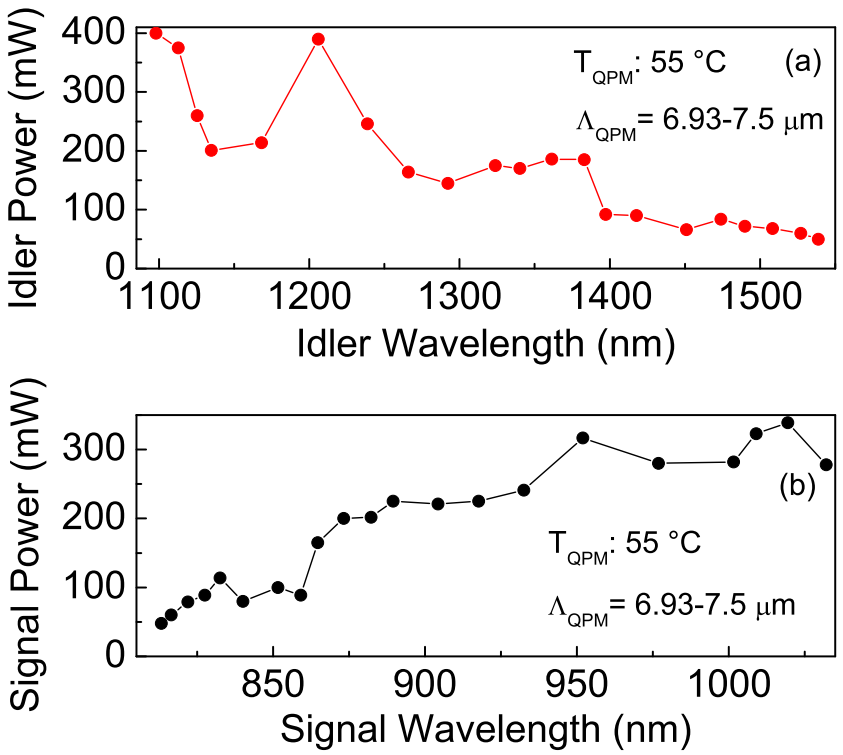


Figure 5.9: (a) Idler, and (b) signal output powers across the tuning range of the green-pumped fanout–grating MgO:PPLN cw OPO.

maximum of 339 mW at 1019 nm, while the idler power varies from a maximum of 400 mW at 1098 nm to 50 mW at 1539 nm. The maximum total simultaneously generated output power is 714 mW, measured at a signal wavelength of 1019 nm and the corresponding idler wavelength of 1113 nm, representing an overall OPO extraction efficiency of 30%. The decline in idler power at longer wavelengths and the corresponding drop in signal power at shorter wavelengths are attributed to the reduction in parametric gain further away from degeneracy. In spite of the short interaction length of the MgO:PPLN crystal compared

to earlier reports [7–9], the performance of our green-pumped OPO in terms of output power and extraction efficiency is superior at identical pumping levels.

### 5.3.2 Power scaling and stability

We carried out simultaneous long-term signal and idler power stability measurements at a signal wavelength of 889 nm and corresponding idler wavelength of 1324 nm for a pump power of 2.4 W, with the results shown in Fig. 5.10. The signal power exhibits a passive power stability better than 2.8% rms over 1 hour, while the simultaneously recorded idler power displays a power stability of 1.8% rms. Similar power stabilities are also observed at other signal and idler wavelengths, as shown in Fig. 5.11, where the signal and idler powers exhibit passive power stabilities better than 2.95% rms and 3.1% rms, respectively, at a signal wavelength of 952 nm and corresponding idler wavelength of 1206 nm. The minimum OPO threshold was recorded to be 2.04 W at an operating signal wavelength of 889.4 nm, as shown in Fig. 5.12. This relatively high threshold compared to previously reported green-pumped MgO:PPLN cw OPOs is attributed to the short interaction length of the crystal used here, in combination with the output coupling. Given the maximum input pump power limit of 2.4 W to avoid any damage to the crystal, the OPO was operated $<2$ times above threshold (2.04 W). However, we also observed severe thermal effects in the MgO:PPN crystal under green pumping. As described earlier, we measure the transmission of the MgO:PPLN crystal to be $\sim$93% at 532 nm. Considering the 1.5%/cm linear absorption, $\sim$4% of the 7% loss is attributed to the absorption at the pump wavelength, resulting in a significant thermal load in the nonlinear crystal. Moreover, considering a thermal conductivity of 4.6 W/m-K [19] and a thermo-optic

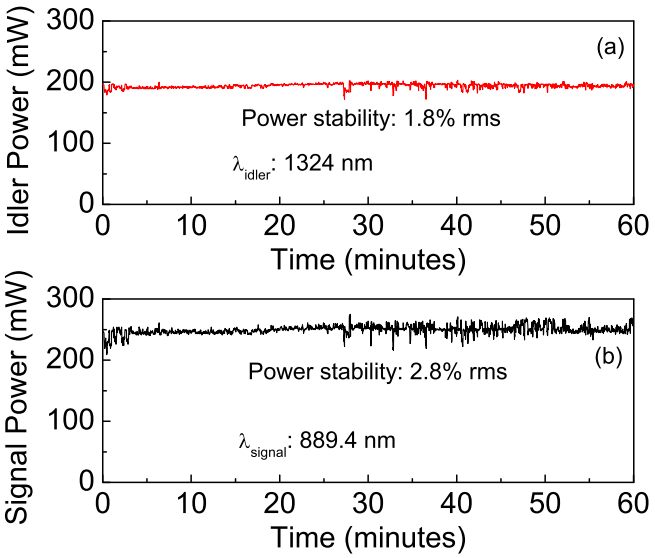


Figure 5.10: Passive power stability of the (a) idler, and (b) extracted signal over 1 hour.

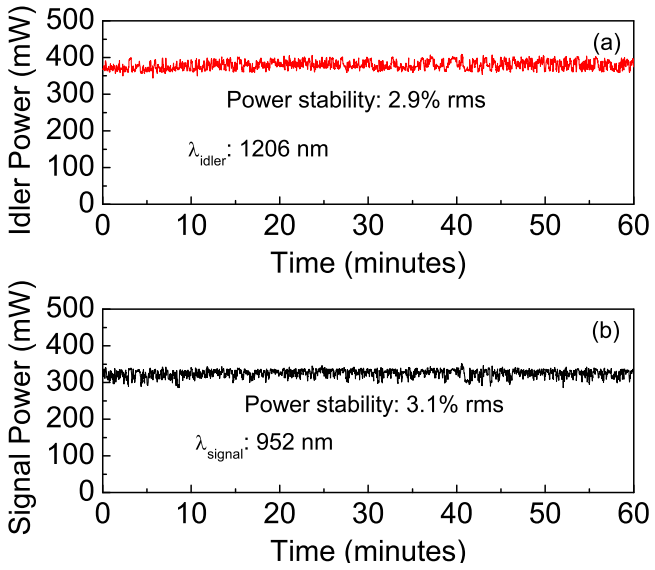


Figure 5.11: Passive power stability of the (a) idler, and (b) extracted signal over 1 hour.

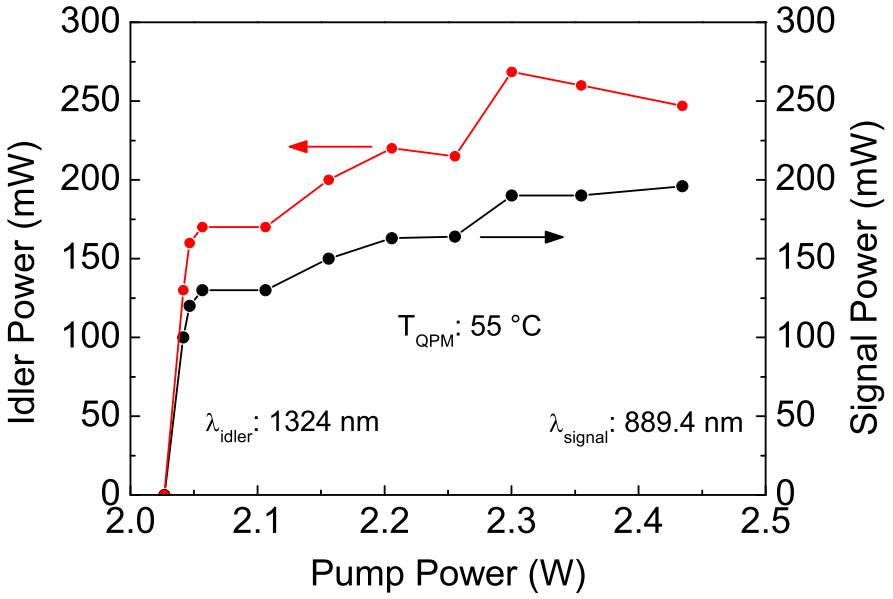


Figure 5.12: Signal and idler power scaling as a function of pump power.

coefficient of $6.5 \times 10^{-5}$ $K^{-1}$, we estimate a thermal lens of focal length, $f_{th}$=20 mm, which is of the same order as the 25 mm length of the MgO:PPLN crystal, implying a strong thermal lens in the material. We attribute the well-defined signal spatial beam profile with a tightly confined mode and the stable output performance of the OPO to the thermal lens in the MgO:PPLN crystal. At the same time, it should also be noted that MgO:PPLN is susceptible to GRIIRA, which is reported to be $1.1 \times 10^{-3}$ $cm^{-1}$ at a green power density of 25 $kW/cm^2$ [22]. This value is significantly higher than that of MgO:sPPLT which exhibits no signature of GRIIRA at the same green power density [22]. While MgO doping is expected to alleviate photorefractive effect in PPLN and reduce GRIIRA, the relatively low thermal conductivity and significantly lower threshold for GRIIRA appear to be the limiting factors for power scaling the green-pumped MgO:PPLN

cw OPO. However, at the current pumping levels below 2.5 W, we have found that our green-pumped cw OPO operates reliably over many hours without any damage to the MgO:PPLN crystal.

### 5.3.3 Spectral characteristics

Using a wavemeter, we recorded the frequency stability of the signal, resulting in a peak–peak deviation of 84.23 MHz over 72 seconds about the mean wavelength of ∼890.89 nm, as shown in Fig. 5.13. Using a confocal Fabry–Perot interferometer, we recorded the output signal spectrum at 889.4 nm, with the result shown in Fig. 5.14. The measurement confirms a single-frequency spectrum with an instantaneous full-width-at-half-maximum (FWHM) linewidth of 3.3 MHz. The signal spectra across the grating tuning range is shown in Fig. 5.15.

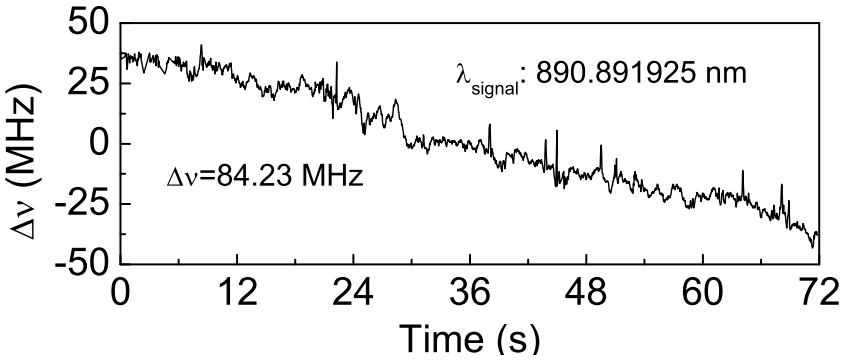


Figure 5.13: Frequency stability of the extracted signal beam at 890 nm.

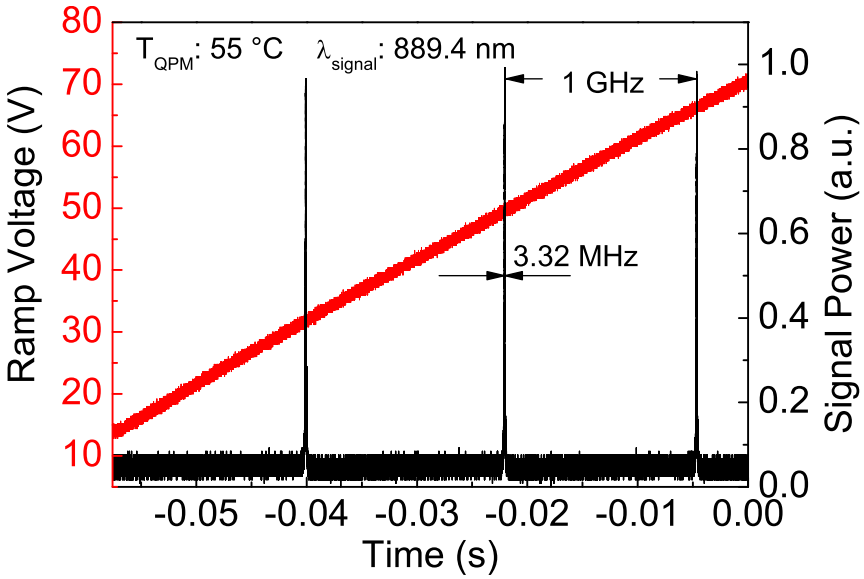


Figure 5.14: Single-frequency spectrum of the extracted signal at 889.4 nm.

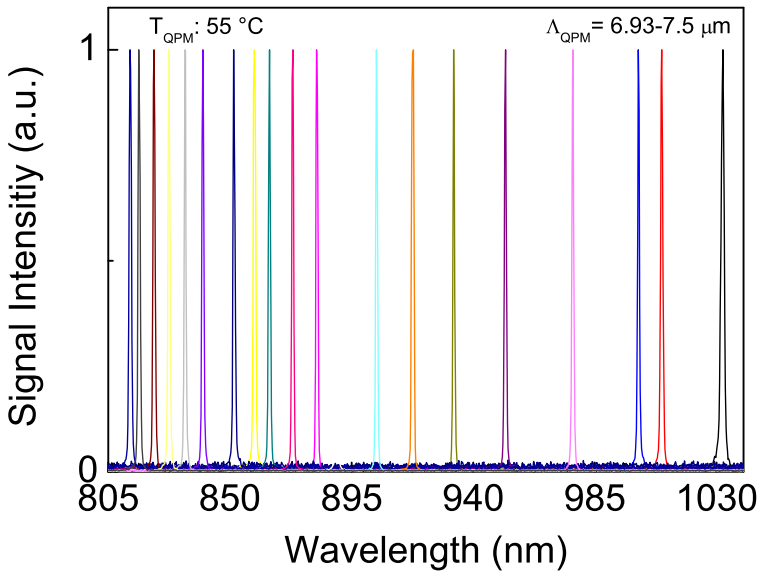


Figure 5.15: Some signal spectra across the grating tuning range.

### 5.3.4 Spatial beam quality

The far-field spatial profile of the signal beam, measured at a distance of ∼25 cm from the OC, and the idler beam, measured at a distance of ∼30 cm from the output mirror, $M_2$, are shown in Fig. 5.16. As can be seen, both signal and idler beams have Gaussian profile, with circularity of 95% and 94%, respectively. We further characterized the beam quality of the signal extracted from the OPO, using a lens of focal length $f$=125 mm and a scanning beam profiler, resulting in a measured value of $M^2 < 1.1$ at a signal wavelength of 952 nm, along both axes, as shown in Fig. 5.17.

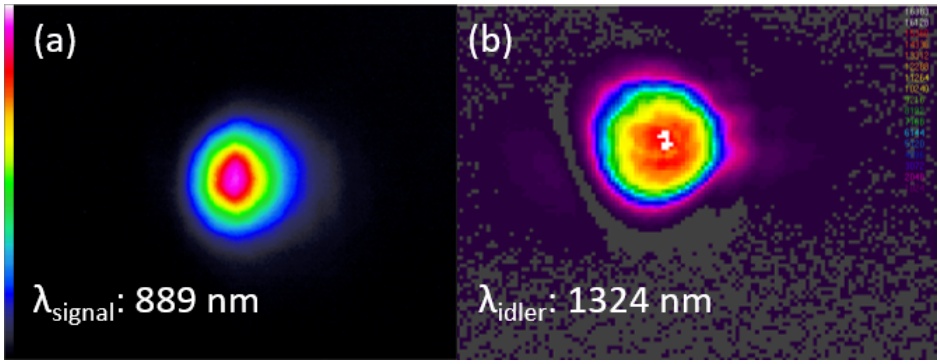


Figure 5.16: Spatial beam profile of (a) signal at 889 nm, and (b) idler at 1324 nm.

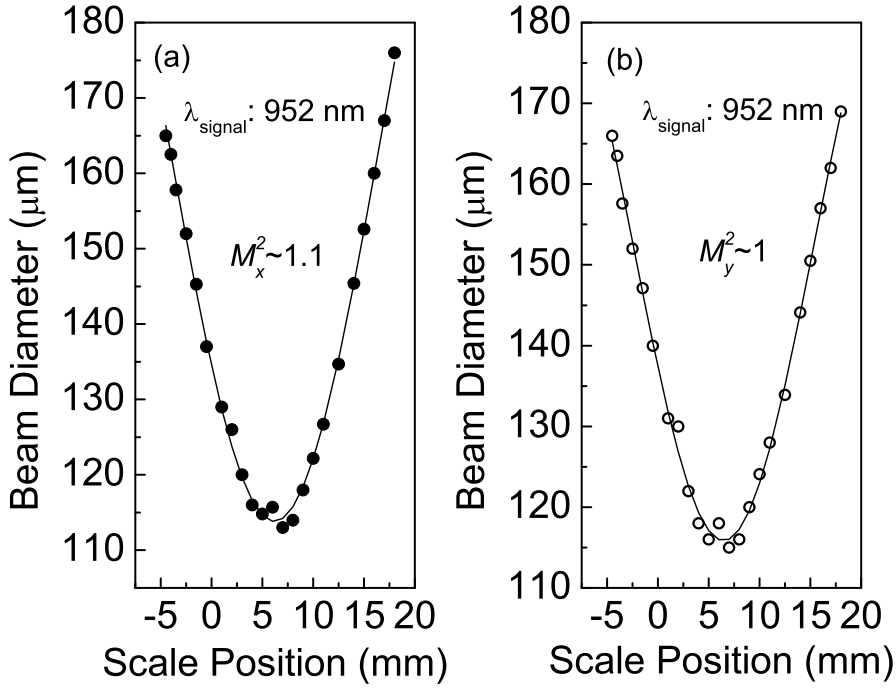


Figure 5.17: Measured signal beam quality at 952 nm in the (a) horizontal, and (b) vertical direction.

## 5.4 Conclusion

In conclusion, we have demonstrated the first green-pumped OPO based on fanned-grating MgO:PPLN. By exploiting the fanout grating structure, the OPO is continuously tunable across 813–1032 nm in the signal and 1098–1539 nm in the idler by lateral translation of the crystal at a fixed temperature. The OPO can deliver a total simultaneous output power of 714 mW at an extraction efficiency of 30%, with signal powers up to 339 mW at 1019 nm and idler powers up to 400

mW at 1098 nm. The signal and idler powers exhibit passive power stability of 2.8% rms and 1.8% rms, respectively, over 1 hour, with excellent spatial beam quality, in a single-frequency signal spectrum with a FWHM linewidth of 3.3 MHz. The exploitation of a fanout grating design, together with signal output coupling, result in not only wide, rapid and uninterrupted wavelength tuning, but also improved output powers and frequency stability. We have not observed any damage to the crystal after long-term operation at pump powers up to 2.5 W. The use of signal output coupling combined with a relatively short interaction length also reduces the thermal load in the MgO:PPN crystal, resulting in increased conversion efficiency, high spatial beam quality, and improved output stability. Strong thermal lensing contributes to the stability of the OPO, while linear absorption, together with GRIIRA, limit the power scalability of the OPO. Because of the mature growth technology and high nonlinearity of MgO:PPLN compared to MgOs:PPLT, it can be a viable material for development of green-pumped cw OPOs at moderate power levels.[1]

[1] The successful development of this OPO led to an industrial internship at Radiantis, which will be described in the next chapter.

# References

[1] D. D. Arslanov, M. Spunei, J. Mandon, S. M. Cristescu, S. T. Persijn, and F. J. M. Harren, "Continuous-wave optical parametric oscillator based infrared spectroscopy for sensitive molecular gas sensing," Laser & Photonics Reviews **7**, 188 (2013).
https://onlinelibrary.wiley.com/doi/10.1002/lpor.201100036

[2] M. Ebrahim-Zadeh, "Continuous-wave Optical Parametric Oscillators." in *Handbook of Optics* (OSA/McGraw-Hill, 2010), Vol. IV, chap. 17, third edn.

[3] R. G. Batchko, D. R. Weise, T. Plettner, G. D. Miller, M. M. Fejer, and R. L. Byer, "Continuous-wave 532-nm-pumped singly resonant optical parametric oscillator based on periodically poled lithium niobate," Optics Letters **23**, 168 (1998).
https://www.osapublishing.org/abstract.cfm?uri=ol-23-3-168

[4] U. Strössner, A. Peters, J. Mlynek, S. Schiller, J.-P. Meyn, and R. Wallenstein, "Single-frequency continuous-wave radiation from 0.77 to 1.73 µm generated by a green-pumped optical parametric oscillator with periodically poled $LiTaO_3$," Optics Letters **24**, 1602 (1999).
https://www.osapublishing.org/abstract.cfm?uri=ol-24-22-1602

[5] U. Strößner, J.-P. Meyn, R. Wallenstein, P. Urenski, A. Arie, G. Rosenman, J. Mlynek, S. Schiller, and A. Peters, "Single-frequency continuous-wave optical parametric oscillator system with an ultrawide tuning range of 550 to 2830 nm," Journal of the Optical Society of America B **19**, 1419 (2002).
https://www.osapublishing.org/abstract.cfm?uri=josab-19-6-1419

[6] D.-H. Lee, S. K. Kim, S.-N. Park, H. Su Park, J. Y. Lee, and S.-K. Choi, "Continuous-wave 532 nm pumped MgO:PPLN optical parametric oscillator with external power regulation and spatial mode filtering," Applied Optics

**48**, 37 (2009).
https://www.osapublishing.org/abstract.cfm?uri=ao-48-1-37

[7] S. Zaske, D.-H. Lee, and C. Becher, "Green-pumped cw singly resonant optical parametric oscillator based on MgO:PPLN with frequency stabilization to an atomic resonance," Applied Physics B **98**, 729 (2010).
http://link.springer.com/10.1007/s00340-009-3871-7

[8] I.-H. Bae, H. S. Moon, S. Zaske, C. Becher, S. K. Kim, S.-N. Park, and D.-H. Lee, "Low-threshold singly-resonant continuous-wave optical parametric oscillator based on MgO-doped PPLN," Applied Physics B **103**, 311 (2011).
http://link.springer.com/10.1007/s00340-010-4297-y

[9] I.-H. Bae, H.-S. Moon, S.-K. Kim, S.-N. Park, and D.-H. Lee, "Self-guided operation of singly resonant continuous-wave optical parametric oscillator based on bulk MgO-doped PPLN," Applied Physics B **106**, 797 (2012).
http://link.springer.com/10.1007/s00340-012-4922-z

[10] P. Groß, I. D. Lindsay, C. J. Lee, M. Nittmann, T. Bauer, J. Bartschke, U. Warring, A. Fischer, A. Kellerbauer, and K.-J. Boller, "Frequency control of a 1163 nm singly resonant OPO based on MgO:PPLN," Optics Letters **35**, 820 (2010).
https://www.osapublishing.org/abstract.cfm?uri=ol-35-6-820

[11] G. K. Samanta, G. R. Fayaz, and M. Ebrahim-Zadeh, "1.59 W, single-frequency, continuous-wave optical parametric oscillator based on MgO:sPPLT," Optics Letters **32**, 2623 (2007).
https://www.osapublishing.org/abstract.cfm?uri=ol-32-17-2623

[12] S. Chaitanya Kumar, K. Devi, G. K. Samanta, and M. Ebrahim-Zadeh, "Fiber-laser-based green-pumped continuous-wave singly-resonant optical

parametric oscillator," Laser Physics **21**, 782 (2011).
http://link.springer.com/10.1134/S1054660X11070140

[13] G. K. Samanta, G. R. Fayaz, Z. Sun, and M. Ebrahim-Zadeh, "High-power, continuous-wave, singly resonant optical parametric oscillator based on MgO:sPPLT," Optics Letters **32**, 400 (2007).
https://www.osapublishing.org/abstract.cfm?uri=ol-32-4-400

[14] A. Henderson and R. Stafford, "Low threshold, singly-resonant CW OPO pumped by an all-fiber pump source," Optics Express **14**, 767 (2006).
https://www.osapublishing.org/oe/abstract.cfm?uri=oe-14-2-767

[15] S. Chaitanya Kumar, R. Das, G. K. Samanta, and M. Ebrahim-Zadeh, "Optimally-output-coupled, 17.5 W, fiber-laser-pumped continuous-wave optical parametric oscillator," Applied Physics B **102**, 31 (2011).
http://link.springer.com/10.1007/s00340-010-4092-9

[16] K. Devi and M. Ebrahim-Zadeh, "Room-temperature, rapidly tunable, green-pumped continuous-wave optical parametric oscillator," Optics Letters **42**, 2635 (2017).
https://www.osapublishing.org/abstract.cfm?uri=ol-42-13-2635

[17] K. Devi, A. Padhye, Sukeert, and M. Ebrahim-Zadeh, "Widely tunable room-temperature continuous-wave optical parametric oscillator based on periodically-poled $KTiOPO_4$," Optics Express **27**, 24 093 (2019).
https://www.osapublishing.org/abstract.cfm?uri=oe-27-17-24093

[18] J. R. Schwesyg, A. Markosyan, M. Falk, M. C. C. Kajiyama, D. H. Jundt, K. Buse, and M. M. Fejer, "Optical loss mechanisms in magnesium-doped lithium niobate crystals in the 300 to 2950 nm wavelength range," in *Advances in Optical Materials* p. AIThE3 (2011).
https://www.osapublishing.org/abstract.cfm?uri=AIOM-2011-AIThE3

[19] O. A. Louchev, N. E. Yu, S. Kurimura, and K. Kitamura, "Thermal inhibition of high-power second-harmonic generation in periodically poled $LiNbO_3$ and $LiTaO_3$ crystals," Applied Physics Letters **87**, 131 101 (2005). http://aip.scitation.org/doi/10.1063/1.2056593

[20] H. Ishizuki and T. Taira, "Mg-doped congruent $LiTaO_3$ crystal for large-aperture quasi-phase matching device," Optics Express **16**, 16 963 (2008). http://www.osapublishing.org/oe/abstract.cfm?uri=oe-16-21-16963

[21] O. Gayer, Z. Sacks, E. Galun, and A. Arie, "Temperature and wavelength dependent refractive index equations for MgO-doped congruent and stoichiometric $LiNbO_3$," Applied Physics B **91**, 343 (2008). http://link.springer.com/10.1007/s00340-008-2998-2

[22] J. Hirohashi, T. Tago, O. Nakamura, A. Miyamoto, and Y. Furukawa, "Characterization of GRIIRA properties in $LiNbO_3$ and $LiTaO_3$ with different compositions and doping," Proc. SPIE **6875**, 687 516 (2008). http://proceedings.spiedigitallibrary.org/proceeding.aspx?doi=10.1117/12.773742

# 6. Industrial internship

This chapter is based on a project done at Radiantis, a leading manufacturer of OPOs based in Barcelona.

## 6.1 Motivation

The manufacture of many instruments requires precise characterization of the constituent components before their incorporation into the final instrument. For example, earth observation satellites require the use of materials and components that demonstrate a high degree of robustness to withstand the extreme operating conditions, typical of outer space. Given the high risks, costs and complexity associated with such aerospace missions, it is crucial to precisely characterize and verify the performance of various components. Some examples of these components include optical amplifiers and modulators, switches, optical fibers, image sensors, optical transceivers and photodiodes. Optical characterization of these components, and evaluation of their response in different regions of the spectrum is an essential part of the entire component characterization process.

Different types of light sources such as LEDs, lasers or white light lamps can be used for component characterization depending on the input wavelength and power requirements. LEDs are commonly used because of their low cost and widespread availability, but for characterization over a wider spectral range, many LEDs of different wavelengths may be required. Thus, the need to constantly use a different input light source can make the component characterization process inefficient for various reasons such as the requirement to manipulate the test rigs every time the light source is changed. Other impediments include the necessary realignment of the test assembly which can be time consuming, and can lead to unwanted variations in measurement, thus reducing the reliability of the results.

Therefore, having a single light source that can cover the entire spectrum of interest is highly desirable for optical characterization of components. Such a light source would typically have a wide tuning range, and should be rapidly tunable to generate all the wavelengths required in the spectral region of interest in a short period of time.

One such spectral region of interest is the near-IR region of 1.1-1.5 µm. This region is useful for characterizing photodiodes and other sensors based on semiconductors such as InGaAs. An existing method to generate all the required wavelengths in this spectral region from a single light source is to use a broadband light source, such as a tungsten-halogen lamp, in combination with a monochromator. However, using such a method has some practical drawbacks, which affect the results of the component characterization process. Using a monochromator on a broadband light source requires a compromise between output power and spectral resolution. Increasing the number of grooves on the grating and narrowing the slit size can improve the spectral resolution, as shown in Fig. 6.1,

but this comes at the cost of reduced output power. In the device characterization setup used for the project described in this chapter, the minimum slit size that could be used to obtain a measurable response from the photodiode was 0.6 mm, along with a grating of 300g/mm. In this configuration, the power of the input light was <1 µW, with FWHM linewidth of each spectra being ∼50 nm, which is significantly broad, and thus not suitable for precise characterization of components. This low power incident on existing commercial InGaAs photodiodes results in a very low photocurrent of the order of nanoamperes (nA), thus requiring the use of sophisticated and expensive nano- and pico-ammeters that can measure such low currents. The low photocurrent output also leads to low signal-to-noise ratio, and poor reproducibility. Using a slit narrower than 0.6 mm results in photocurrent not being measurable even with the high-precision current source measurement unit. Moreover, using a broadband light source on a grating can result in unwanted higher-order diffraction showing up in the spectrum. Thus, the combination of low output power together with broad spectral output makes the existing setup unsuitable for carrying out precise characterization of InGaAs sensors in the near-IR, and there is a need for a light source that is capable of generating wavelengths in the 1.1-1.5 µm region with high output power in narrow linewidth. Existing lasers in the near-IR do not offer such wide tunability required for this component characterization process. Continuous-wave (cw) optical parametric oscillators (OPOs) are capable of providing widely tunable radiation in narrow linewidth down to single-mode output with high beam quality [1]. Such OPOs pumped in the green are viable sources of near-IR radiation. Given the low pump intensities available under cw regime, practical cw OPOs are exclusively based on QPM nonlinear materials, with MgO:PPLN be-

ing a material of choice for developing cw OPOs because of its high nonlinearity together with a mature growth and poling technology, and widespread availability. It is possible to obtain MgO:PPLN in fanned grating design with grating periods of $\Lambda \leq 10$ µm, as required for green pumping. A description of existing green-pumped cw OPOs and different ways of achieving wavelength tuning has already been given in the chapters 1, 3, and . The development of a green-pumped OPO based on fan-out grating MgO:PPLN, described in chapter 5, and the good quality output obtained from it showcased its potential to be used for real industrial and scientific applications. In this chapter, we describe the development of a cw green-fiber-pumped OPO at Radiantis, and using it to optically

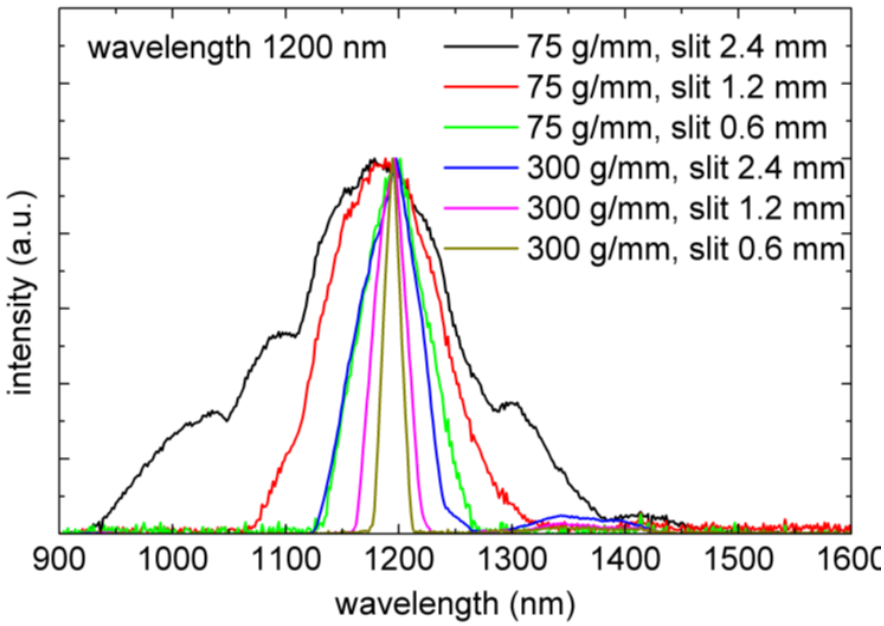


Figure 6.1: Example spectra for different slits and grating configurations of a monochromator used with a tungsten-halogen lamp.

characterize an InGaAs sensor, resulting in orders-of-magnitude improvement in the characterization process over existing methods.

## 6.2 Experimental Setup

A schematic of the experimental setup is shown in Fig. 6.2. A cw green-fiber laser (IPG-GLR-10), capable of delivering up to 10 W of output power at 532 nm in a single-frequency linearly polarized beam with $M^2$ <1.1 is used as the pump source for the OPO. A combination of a half-wave plate and a polarizing beam cube is used for power attenuation and a second half-wave plate is used for adjusting the pump beam polarization. The nonlinear crystal used for the OPO is a 5 mol% MgO:PPLN with a crystal length of 25 mm, and a cross section of $12 \times 0.5$ mm$^2$, in a fanout grating design, with a continuously varying grating period over $\Lambda$ = 6.9-8.1 µm across its lateral dimension. The pump beam is focused to a beam waist radius of $w_0$ ∼38 µm using a lens, and the OPO is configured in a compact ring cavity comprising two concave mirrors $M_{1,2}$ ($r$=−100 mm), and two plane mirrors $M_{3,4}$. All mirrors used initially were highly reflecting ($R$>99.8%) over 850-1200 nm, and highly transmitting for the pump. This DRO configuration was initially used to make the OPO operational. Later, mirror $M_4$ was replaced with another plane mirror, highly reflecting ($R$>99.8%) over 620-1030 nm for the signal, and highly transmitting ($T$>97%) across 1078 nm-3550 nm for the idler and pump, ensuring SRO operation in the signal. This configuration results in mirror $M_4$ being used as the output for the idler. A long-pass filter was used to separate the residual pump and signal from the output idler, and the idler beam was directed to the input of the device characterization setup, used for

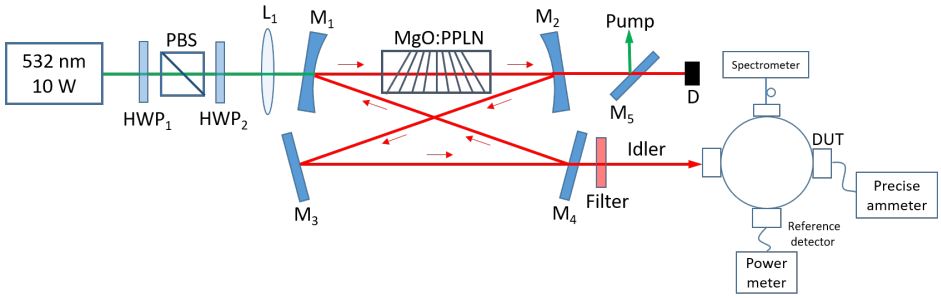


Figure 6.2: Schematic of green-fiber-pumped fan-out grating MgO:PPLN cw OPO with the device characterization setup. HWP, half-wave-plate; PBS, polarizing beam-splitter; L, lens; M, mirrors; D, beam dump; DUT, device under test.

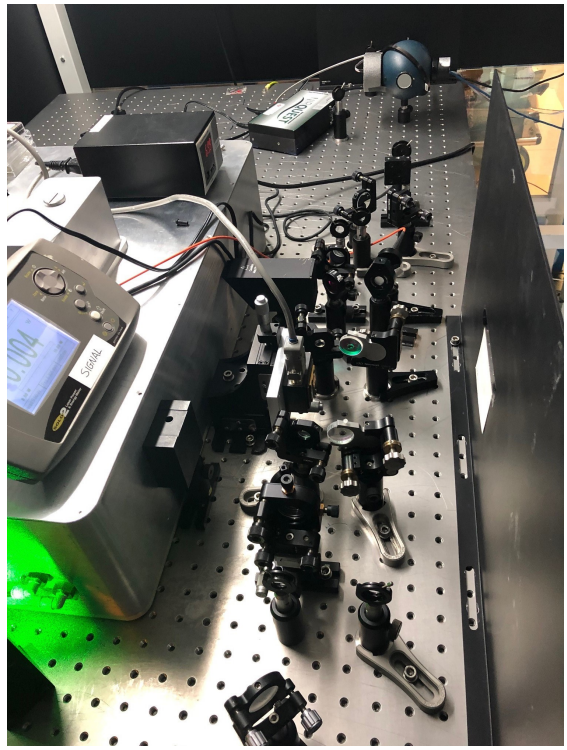

Figure 6.3: Laboratory photograph of the green-pumped cw OPO developed at Radiantis along with the device characterization setup.

characterizing the photodiode. The device characterization setup consists of an integrating sphere with 4 ports in the same plane, one of which is used for the input idler. One port is used to attach the spectrometer (Ocean Optics NIRQ512), while the third and fourth ports are used for the device under test (DUT) and the power meter, respectively. A laboratory photograph of the OPO and the device characterization setup is shown in Fig. 6.3.

## 6.3 Results

### 6.3.1 OPO characterization

#### Wavelength tuning

Wavelength tuning in the OPO was achieved by either varying the crystal grating at a fixed temperature or by changing the crystal temperature at a fixed grating period. We investigated the tuning capabilities of the OPO at fixed temperature of 70 °C by varying the crystal position laterally to continuously change the QPM grating period, with the results shown in Fig. 6.4. As can be seen, the OPO is continuously tunable across 846-963 nm in the signal, and over 1190-1433 nm in the idler. The grating periods shown were theoretically calculated from the measured wavelengths by using Sellmeier equations of the material [2]. Wavelength tuning could also be carried out by changing the crystal temperature for a fixed grafting period, and in order to cover the desired spectral range for component characterization, we also performed temperature tuning at a fixed grating period of $\Lambda = 6.96$ µm. The results are shown in Fig. 6.5, where by changing the crystal temperature from 35 °C to 80 °C, the OPO could be tuned

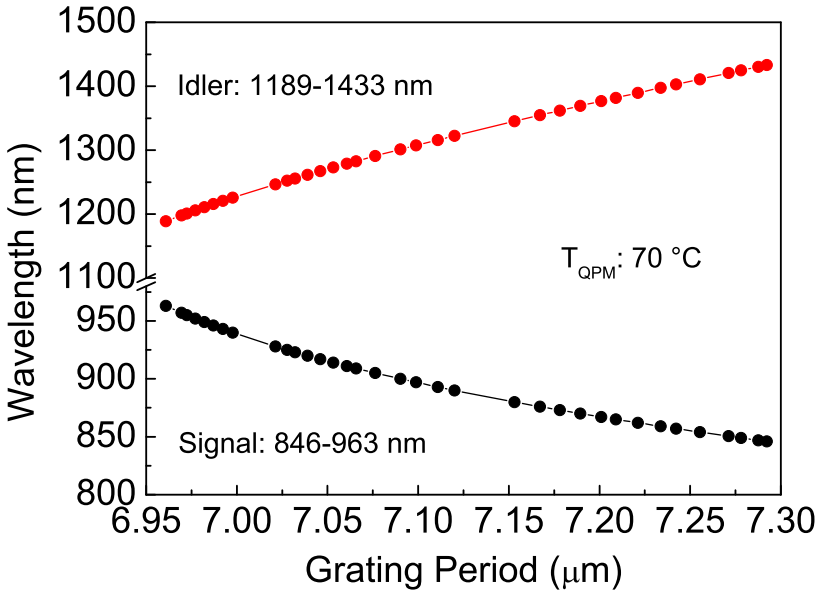


Figure 6.4: Wavelength tuning range of the green-pumped cw OPO as a function of the MgO:PPLN fanout grating period at a fixed temperature of 70 ˚C.

across 952-1030 nm in the signal and over 1100-1205 nm in the idler. Also shown in Fig. 6.5 is the theoretical temperature tuning curve for the corresponding grating period. The OPO ceased to operate at higher temperatures. Thus, by combining grating tuning and temperature tuning, we could get a global tuning range of 1100-1433 nm in the idler, satisfying the requirements of the component characterization process. The idler power across the tuning range is shown in Fig. 6.6. As can be seen, the idler power varies from 560 mW at 1100 nm to 20 mW at 1433 nm. The drop in idler power at longer idler wavelengths is attributed to the reduction in parametric gain away from degeneracy. The idler power at any idler wavelength is significantly higher than what could be achieved by using the monochromator on the tungsten-halogen lamp, and thus

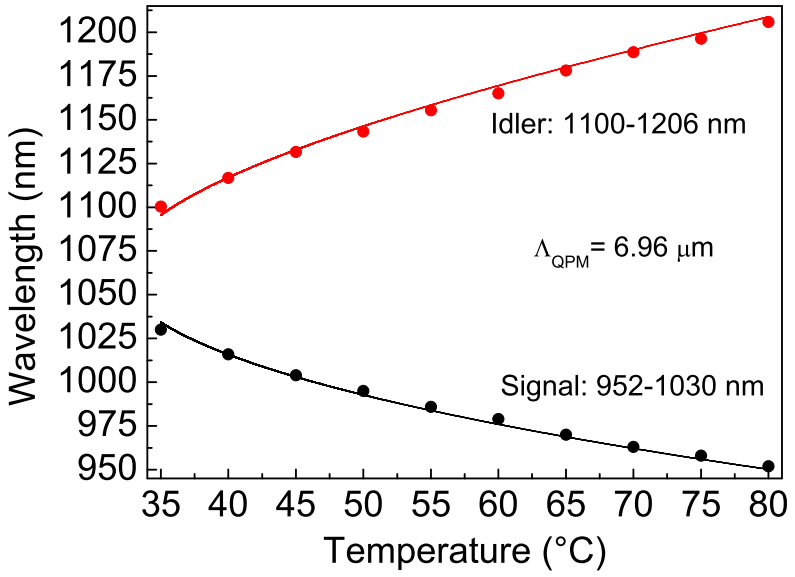


Figure 6.5: Wavelength tuning at a fixed grating period of $\Lambda = 6.96$ µm.

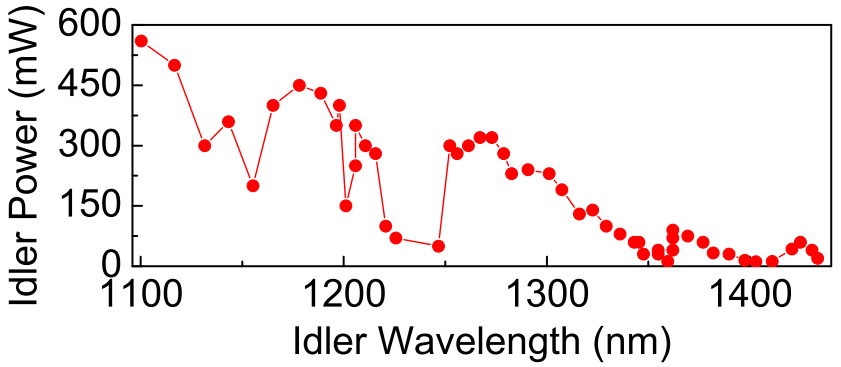


Figure 6.6: Idler output power across the tuning orange of the green-pumped cw OPO.

the cw green-pumped OPO is well suited for use as a light source for the given component characterization process.

### Power stability

We also recorded the passive power stability of the output idler at a few different wavelengths and temperatures, with the results shown in Fig. 6.7. At a crystal temperature of 55 °C, the idler output beam at the wavelength of 1230 nm exhibited a passive power stability of 33.2% rms over more than 2 minutes. The power

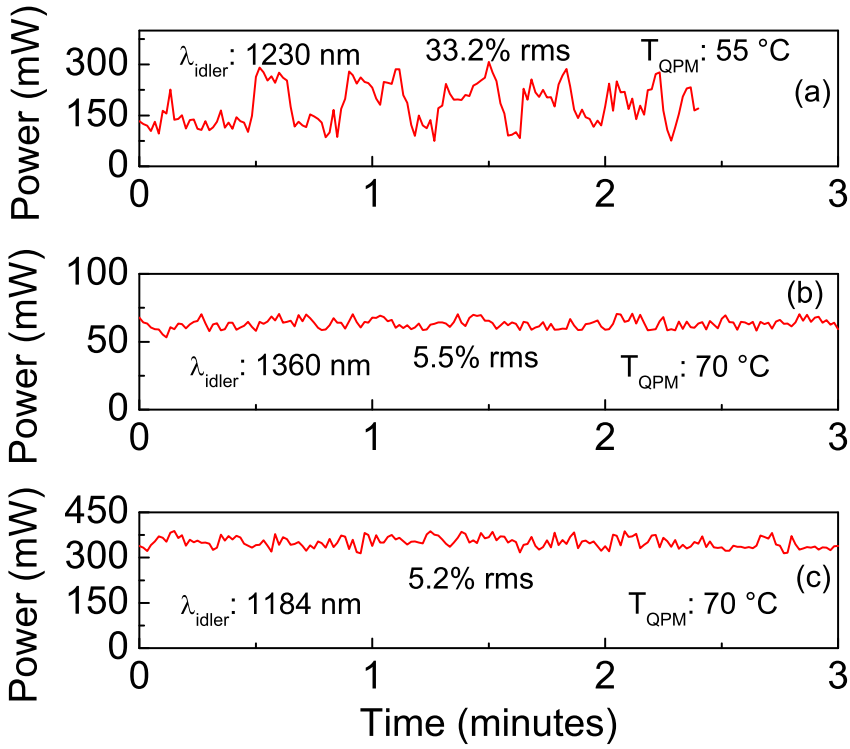


Figure 6.7: Passive power stability of the idler for the idler wavelength of (a) 1230 nm at T=55 °C, (b) 1360 nm at T=70 °C, and (c) 1184 nm at T=70 °C

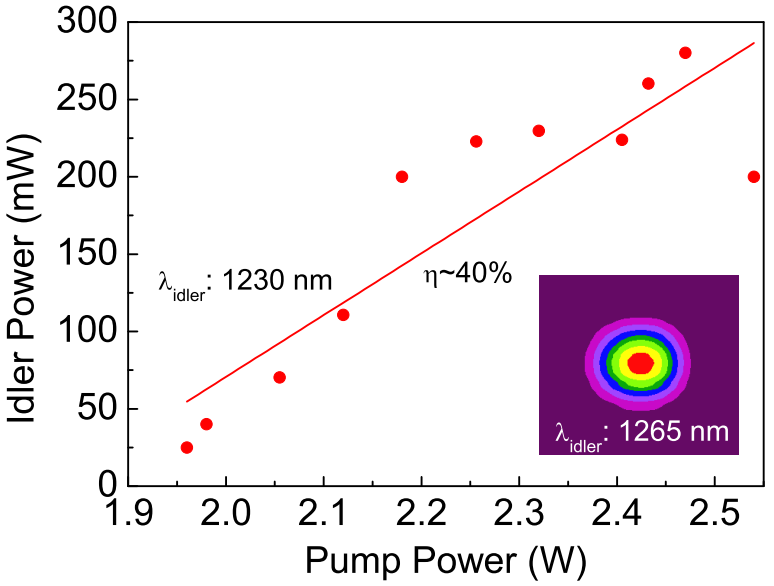


Figure 6.8: Variation of idler power as a function of input pump power for the green-pumped cw OPO. Inset: spatial beam profile of the idler at 1265 nm.

stability, however, significantly improved when the crystal temperature was increased to 70 °C, where the idler output beam exhibited a power stability better than 5.5% rms and 5.2% rms for wavelengths of 1360 and 1184 nm respectively, over 3 minutes. Given the superior performance of the OPO at a temperature of 70 °C compared to lower temperatures, the operating temperature of the OPO was set to 70 °C for the grating tuning range.

### Power scaling

To study the power scaling capabilities of the OPO, we also recorded the variation of output idler power as a function of input pump power, with the results shown in Fig. 6.8. These measurements were carried out at a crystal temperature of 70

°C for an idler wavelength of 1230 nm. As can be seen from Fig. 6.8, the output power scales with the input pump power, with some sudden transitions which could be due to thermal effects in the crystal caused by the pump beam and high intracavity power. The threshold pump power was recorded to be ∼1.9 W at 1230 nm, and we recorded a maximum output power of 280 mW for a pump power of 2.5 W. We limited the pump power to 2.5 W to avoid catastrophic damage to the crystal, as mentioned in the chapter 5.

**Spatial and spectral characterisitics.**

The far-field spatial profile of the idler beam, measured at a distance of ∼45 cm from the output was in a Gaussian $TEM_{00}$ mode with a circularity of ∼87%, shown in the inset of Fig. 6.8. The idler output spectra across the tuning range, measured with a spectrometer (Ocean Optics NIRQ512) are shown in Fig. 6.9. Compared to the spectral output of the monochromator, shown in Fig. 6.10, the output from the OPO has a significantly narrower spectral linewidth, with the measurement limited by the resolution of the spectrometer (∼15 nm), as seen in Fig. 6.11.

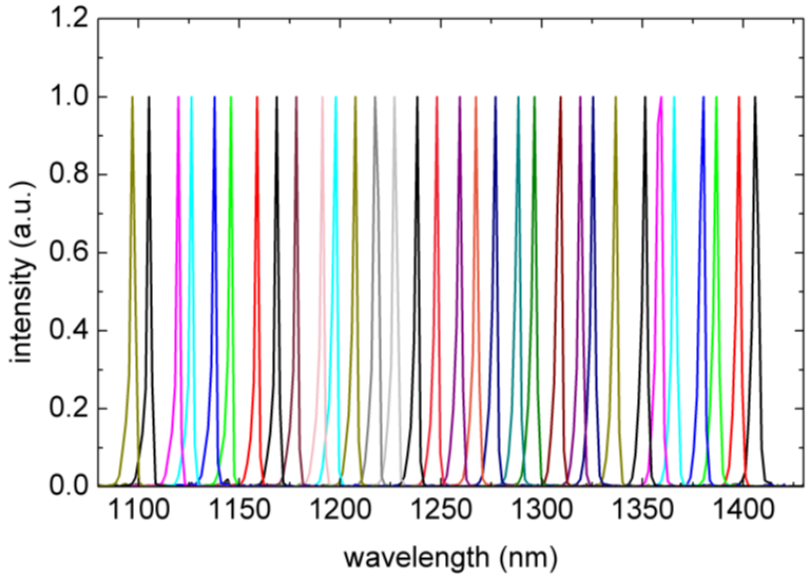


Figure 6.9: Idler spectra across the tuning range of the green-pumped cw OPO.

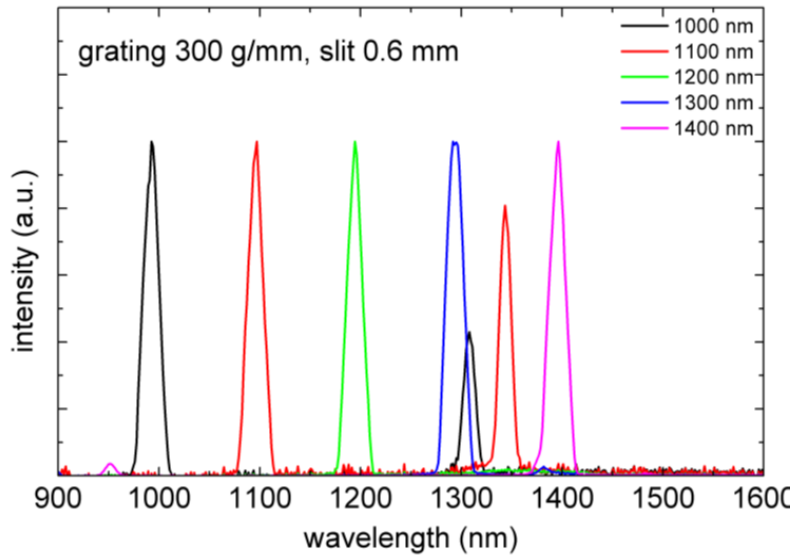


Figure 6.10: Example spectra from the monochromator for grating with 300g/mm and slit of 0.6 mm.

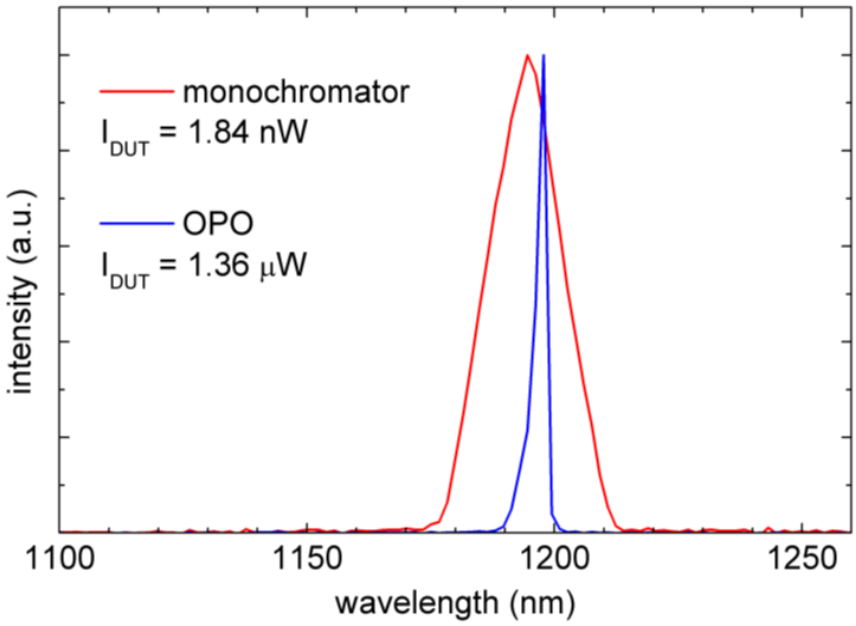


Figure 6.11: Comparison of the idler and monochromator spectra around 1200 nm, along with an example of the corresponding photocurrent measured in DUT.

## 6.4 Testing of components

After characterizing the OPO, the idler output beam was directed to the input of the device characterization setup, in order to characterize the InGaAs sensor. The results of the characterization process using the monochromator on tungsten-halogen lamp as the light source are shown in Fig. 6.12. For comparison, the results obtained by using the green-pumped cw OPO as the input light source are shown in Fig. 6.13. As can be seen, the photocurrent measured in the photodiode while using the OPO is in the µA range, which is 3 orders of magnitude higher than that obtained while using monochromator on tungsten-halogen lamp as light

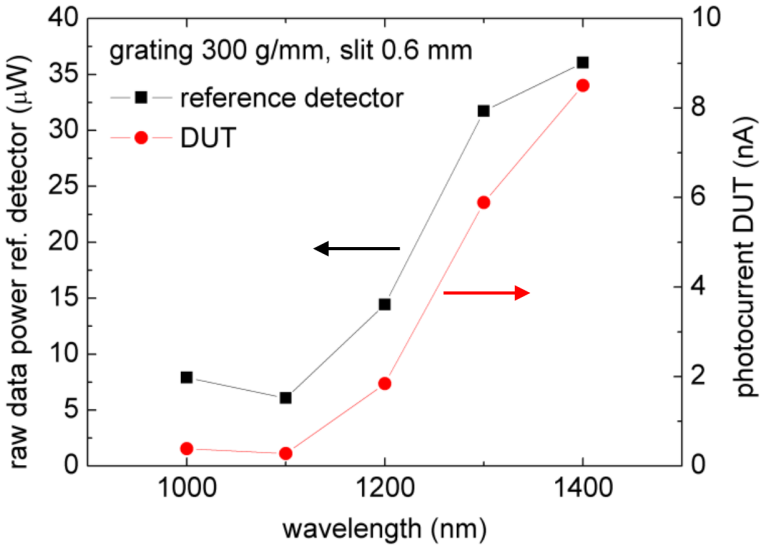


Figure 6.12: DUT photocurrent, and power of reference detector as a function of wavelength when using monochromator on the tungsten-halogen lamp as the input light source.

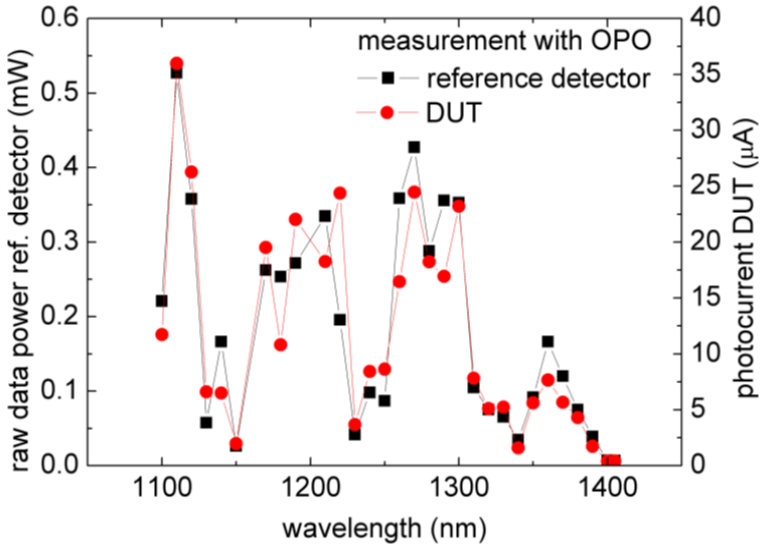


Figure 6.13: DUT photocurrent, and power of reference detector as a function of wavelength when using green-pumped cw OPO as the input light source.

source, which is of the order of nA or even lower. Thus, the high output current in the photodiode while using green-pumped cw OPO results in a more accurate characterization of the detectors and precludes the need for sophisticated and expensive nano- or pico-ammeters. Mid-level multimeters will be sufficient for these measurements. The high output current also leads to exceptionally low measurement error (1%) when using the OPO as compared to using a monochromator on tungsten-halogen lamp as the light source. Moreover, because of the significantly narrower spectra from the OPO, precise characterization of components at different wavelengths, and in small characterization steps, is possible.

## 6.5 Conclusion

In this chapter, we have demonstrated the development of cw green-pumped OPO in an industrial setting and its utility in the optical component characterization process. By exploiting the fan-out grating structure in the MgO:PPLN crystal in combination with temperature tuning, the OPO is continuously tunable across 1100-1433 nm in the idler, satisfying the requirement of the near-IR spectral range for the component characterization process. The OPO can deliver up to 560 mW of output power at 1100 nm. The idler power exhibits a passive power stability of 5.2% rms over 3 minutes at 1184 nm. The idler output beam has a Gaussian profile with circularity better than 87%. The output power of the OPO across the tuning range is significantly higher than that obtained by using a monochromator on a tungsten-halogen lamp, leading to a 3 order of magnitude higher photocurrent in the photodiode, resulting in a more accurate characterization of the detectors with a low measurement error, and eliminating

the need of expensive nano- and pico-ammeters. Compared to the using the monochromator on tungsten-halogen lamp, the output spectra of the OPO are significantly narrower, allowing for a fine and more precise characterization of the detectors. Thus, using a cw green-pumped OPO as a near-IR light source leads to significant improvement in the optical characterization process over existing methods. Further improvements could be achieved by extending the spectral coverage of the OPO, and integrating the OPO with the test assembly, which could lead to commercialization of the system.

# References

[1] M. Ebrahim-Zadeh, "Continuous-wave Optical Parametric Oscillators." in *Handbook of Optics* (OSA/McGraw-Hill, 2010), Vol. IV, chap. 17, third edn.

[2] O. Gayer, Z. Sacks, E. Galun, and A. Arie, "Temperature and wavelength dependent refractive index equations for MgO-doped congruent and stoichiometric $LiNbO_3$," Applied Physics B **91**, 343–348 (2008). http://link.springer.com/10.1007/s00340-008-2998-2

# 7. High-power continuous-wave difference-frequency-generation at 2.26 µm

This chapter is based on the following publications:

**Sukeert**, S. Chaitanya Kumar, and M. Ebrahim-Zadeh, "High-Power, Continuous-Wave, Fiber-Pumped Difference-Frequency-Generation at 2.26 µm," IEEE Photonics Technology Letters **33**, 627 (2021).

S. Chaitanya Kumar, **Sukeert**, and M. Ebrahim-Zadeh, "High-power continuous-wave mid-infrared difference-frequency generation in the presence of thermal effects," Journal of the Optical Society of America B **38**, B14 (2021).

## 7.1 Motivation

High-power, continuous-wave (cw) mid-infrared (mid-IR) sources in the 2-3 µm spectral range are in high demand for variety of applications from spectroscopy [1,2] to material processing [3]. In particular, cw sources at 2.26 µm are attractive

for biomedical applications targeting the 4th biological window, because of the possibility to achieve increased penetration depth in various types of biological tissue [4, 5]. Another important driving force behind the development of mid-IR sources in this wavelength range is the need for high-power pump sources for frequency downconversion based on non-oxide mid-IR nonlinear materials such as $CdSiP_2$ (CSP), $ZnGeP_2$ (ZGP) and orientation-patterned GaAs (OP-GaAs) [6]. The interest is based not only to take advantage of their high nonlinearity and wide mid-IR transparency range compared to their oxide-based counterparts, but also to avoid detrimental effects such as multiphoton absorption [7], thereby enabling spectral coverage beyond 4 µm.

To this extent, various technologies including laser diodes [8,9], as well as bulk solid-state and fiber lasers [10], have been extensively investigated. Although room-temperature operation of cw diode lasers in the 2–2.7 µm wavelength range has been demonstrated [8], providing milliwatt level output powers, high-power cw lasers in this spectral region are often based on solid-state and fiber lasers. Traditionally, access to wavelengths in the vicinity of 2 µm is achieved by Thulium (Tm)-doped solid-state and fiber lasers emitting in the 1.9–2 µm wavelength range, providing multiwatt cw output power [10]. Attempts to extend this range in Tm-doped fiber lasers has resulted in low-power, dual-wavelength operation at 1.9 and 2.3 µm [11]. While solid-state lasers based on Tm-doped crystalline media have been used to generate mid-IR wavelengths in the 2.2-2.4 µm range, their cw output powers is limited to <200 mW [12–14]. Holmium (Ho)-doped lasers, in-band pumped by Tm lasers, provide an ideal route to achieve high output powers, but operation has been limited to 2.1 µm [15]. The use of transition-metal-doped semiconductor gain materials, such as $Cr^{2+}$:ZnS/ZnSe, emitting in the 2–3.5 µm

region, could further extend the operating wavelength range [16, 17], and while high output powers are available [18], the technology has not yet matured for their deployment for some applications, including pumping of mid-IR cw OPOs, which typically exhibit multi-watt operation thresholds [19].

Hence, it is important to investigate alternative strategies for the development of high-power coherent cw sources near 2 µm. To this end, nonlinear frequency conversion sources based on single-pass difference-frequency-generation (DFG) and optical parametric oscillators (OPOs) can readily provide access to the mid-IR spectral region, together with high output power in good spatial beam quality [20]. Using suitable pump lasers in combination with the well-established quasi-phase-matched (QPM) nonlinear materials such a MgO-doped periodically poled $LiNbO_3$ (MgO:PPLN), OPOs can provide unrestricted and gap-free spectral coverage in the 2–3 µm wavelength range [21, 22]. However they also require customised mirrors, intricate cavity designs, precise alignment, careful parameter control for stable operation, and mandatory multi-watt pump powers to reach threshold [23]. On the other hand, as a simple single-pass process, DFG eliminates the need for a resonant cavity and does not require the attainment of an oscillation threshold, making it an attractive alternative for mid-IR generation [24]. Moreover, as a single-pass process, the characteristics of the input pump are directly transferred to the DFG output, enabling high spatial and spectral properties and stability in the mid-IR when using pump sources of high beam quality. With the rapid advances in compact, robust, and high-power cw fiber lasers, together with the widespread availability of MgO:PPLN with high nonlinearity ($d_{\text{eff}}$∼16 pm/V) and long interaction lengths, simple single-pass DFG schemes can now provide a viable and practical solution for the development of

robust multi-watt cw sources in the mid-IR, while preserving a compact form factor.

Previous demonstrations of cw DFG sources based on PPLN and MgO:PPLN include tunable DFG at 2.3 µm in a PPLN ridge waveguide generating ∼4.5 mW of output power at a conversion efficiency of 56%/W [25], and tunable DFG in the 2.9–3.4 µm wavelength range based on bulk MgO:PPLN with ∼3 mW of output power at 3.03 µm at a maximum conversion efficiency of 0.007%/W [26]. In another report, tunable DFG in bulk MgO:PPLN in the 3.1–3.6 µm range was demonstrated, providing >60 mW of output power at a conversion efficiency of ∼0.09%/W [27], and a DFG source based on bulk MgO:PPLN at a fixed wavelength of 3.4 µm with an output power of 3.55 W at a conversion efficiency of ∼0.26%/W has also been reported [28].

In this chapter, we describe a high-power cw source at 2.26 µm based on DFG of a cw ytterbium (Yb)-fiber laser at 1.064 µm with a cw Tm-fiber laser at 2.010 µm in MgO:PPLN. With a maximum available input power of 27.3 W at 1.064 µm and 30 W at 2.010 µm, and using a 50-mm-long crystal, we have generated 3.84 W of cw output power at 2.26 µm in a simple single-pass scheme, with a conversion efficiency of up to 0.57%/W. The DFG output exhibits excellent passive power stability better than 0.6% rms, and a spectral stability better than 0.01% over 1 hour, in $TEM_{00}$ mode profile with $M^2 < 1.2$, and exhibits a beam pointing stability better than 16 µrad over >1 hour. To the best of our knowledge, this work represents the first demonstration of DFG between Yb- and Tm-fiber laser, with highest cw power generated from any single-pass nonlinear frequency conversion scheme in the mid-IR. A summary of cw mid-IR DFG based on bulk MgO:PPLN is given in Table 7.1

| Pump (µm) | Signal (µm) | Crystal length (mm) | QPM grating period (µm) | DFG (µm) | DFG Power (W) | Conversion efficiency (%/W) | Ref |
|---|---|---|---|---|---|---|---|
| 0.78-0.81 | 1.064 | 10 | 21-22.5 µm | 2.9-3.4 | 0.003 (3.03 µm) | 0.007 | [26] |
| 1.04-1.084 | 1.545-1.561 | 40 | 29.98 | 3.1-3.6 | 0.078 ( 3.56 µm) | 0.08 | [27] |
| 1.064 | 1.55 | 50 | 30.5 | 3.4 | 3.55 | 0.27 | [28] |
| 1.064 | 2.01 | 50 | 32.16 | 2.26 | 3.84 | 0.47 | Ch. 7 |

Table 7.1: Mid-IR cw DFG based on bulk MgO:PPLN.

## 7.2 Experimental design

The schematic of the experimental setup for the DFG source is shown in Fig. 7.1. A commercial cw Yb-fiber laser (IPG Photonics, YLR-30-1064-LP-SF), delivering up to 30 W of output power at 1064.1 nm with a nominal linewidth of ∼100 kHz in a single-frequency linearly polarized beam with $M^2 < 1.1$, is used as the pump source for DFG, while a cw Tm-fiber laser (IPG Photonics, TLR-50-2010-LP), delivering up to 37 W of output power in a linearly polarized beam, with a full-width-at-half-maximum (FWHM) spectral bandwidth of ∼0.7 nm centered at 2009.3 nm serves as the input signal. A combination of half-wave plate ($\lambda/2$) and polarizing beam-splitter (PBS) is used for independent power control of the pump and signal sources, and a second half-wave plate is used to control the polarization of pump and signal. The pump and signal beams are independently focused using lenses, $L_1$ and $L_2$, to a beam waist radius of $w_{0p}$∼60 µm and $w_{0s}$∼63 µm, corresponding to the focusing parameter of $\xi_p$∼1.1 and $\xi_s$∼1.9, respectively. The scheme also enables flexible and robust mode-matching as well as optimization of the position of the focal spots in the crystal. A dichroic beam combiner (DBC), antireflection (AR)-coated for high transmission ( $T$ >81%) at 2009.3 nm and high

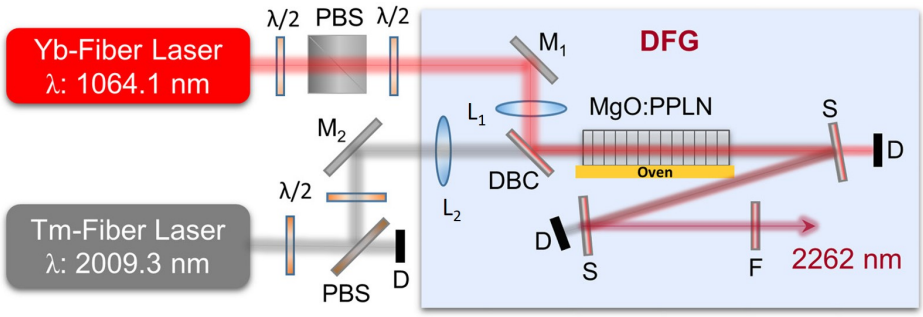


Figure 7.1: Schematic of the experimental setup for cw single-pass DFG based on MgO:PPLN. λ/2, half-wave plate; PBS, polarizing beam-splitter; M, steering mirrors; DBC, dichroic beam combiner; L, lens; S, DFG separator; F, filter; and D, beam dump.

reflection ($R$ >99%) at 1064.1 nm is used to combine the pump and signal beams before entering the nonlinear crystal. After accounting for the AR-coating losses of $L_1$, $L_2$, and DBC, we measured a maximum available pump power of ∼27.3 W and signal power of ∼30 W at the input to the nonlinear crystal, which is a 50-mm-long, 2-mm-wide, 1-mm thick 5 mol% MgO:PPLN with a single grating period of $\Lambda = 32.16$ µm for type-0 ($ee \rightarrow e$) QPM parametric interaction. The end faces of the crystal are AR-coated at 1064 nm ($R$ <1%) and over 2000–2500 nm ($R$ <2%). The crystal is mounted on an oven with a temperature stability of ±0.1 ˚C, to enable optimum phase-matching for DFG. Two identical mirrors (S) and a high-power long-pass filter (F) are used to extract the generated DFG beam at 2262 nm from the transmitted pump and signal beams. The transmission of the crystal was found to be 99.4% for the pump and 95.6% for the signal, as shown in Fig. 7.2. The calculated temperature acceptance bandwidth for DFG between our pump and signal wavelengths to generate 2262 nm, under plane-wave approximation, using the relevant Sellmeier equations [29], is shown

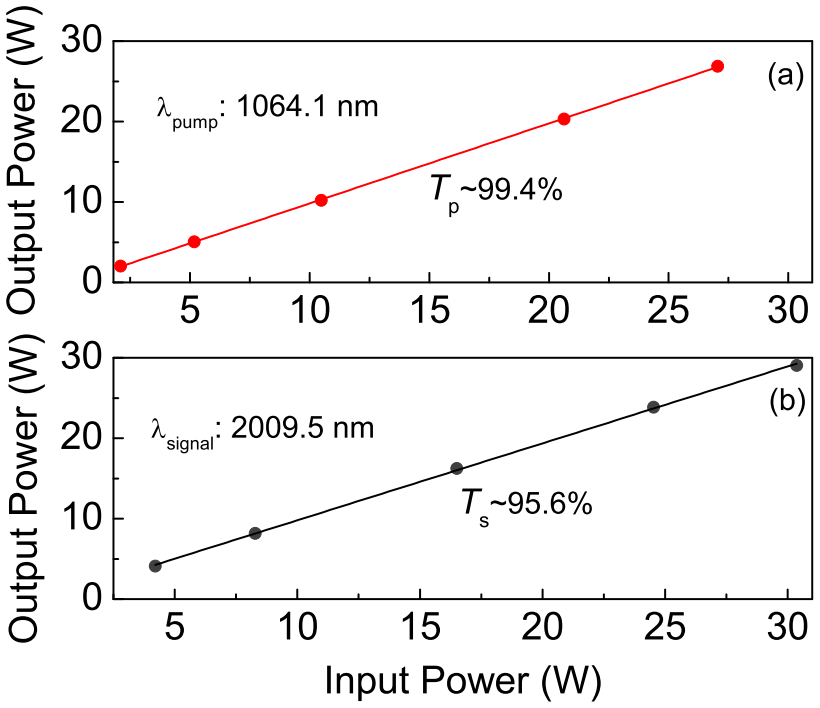


Figure 7.2: Transmission of the 50-mm-long MgO:PPLN crystal at (a) pump, and (b) signal wavelength in phase-matched polarization.

in Fig. 7.3. The phase-matching temperature for DFG between the pump and signal wavelengths to generate 2262 nm, using a grating period of $\Lambda = 32.16$ µm, is estimated to be ∼70.3 ˚C. However, thermal expansion in MgO:PPLN crystal when operating at high temperatures results in a relatively longer effective grating period. The variation of the effective grating period of our MgO:PPLN crystal with an initial grating period of $\Lambda = 32.16$ µm at room temperature, as a function of the operating temperature in the vicinity of our estimated phase-matching temperature for DFG, is shown in the inset of Fig. 7.3. Hence, using a nominal grating period of $\Lambda = 32.18$ µm, the phase-matching temperature is

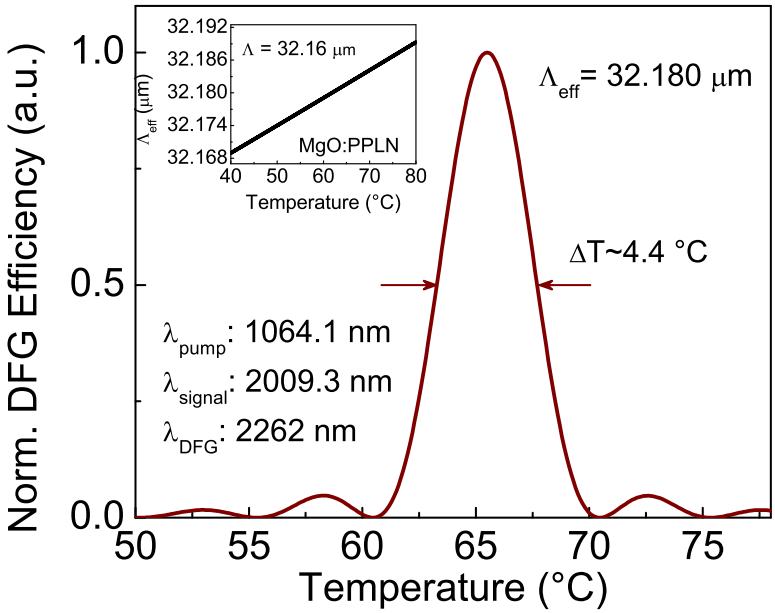


Figure 7.3: Theoretical normalized DFG efficiency as a function of the phase-matching temperature. Inset: variation of the effective MgO:PPLN grating period as a function of temperature in the vicinity of the expected phase-matching temperature.

estimated to be 65.3 ˚C, with a FWHM temperature acceptance bandwidth of ∼4.4 ˚C, as seen in Fig. 7.3. The parametric gain bandwidth as a function of the pump and signal wavelengths under plane wave approximation are shown in Fig. 7.4 and 7.5, respectively. The normalized DFG efficiency as a function of the pump wavelength for a fixed signal wavelength at 2009.3 nm, results in a pump FWHM spectral acceptance bandwidth of ∼0.7 nm, as presented in Fig. 7.4. The pump laser spectrum operating at a central wavelength of 1064.1 nm is also depicted in Fig. 7.4, and the fringe pattern recorded using a Fabry–Perot

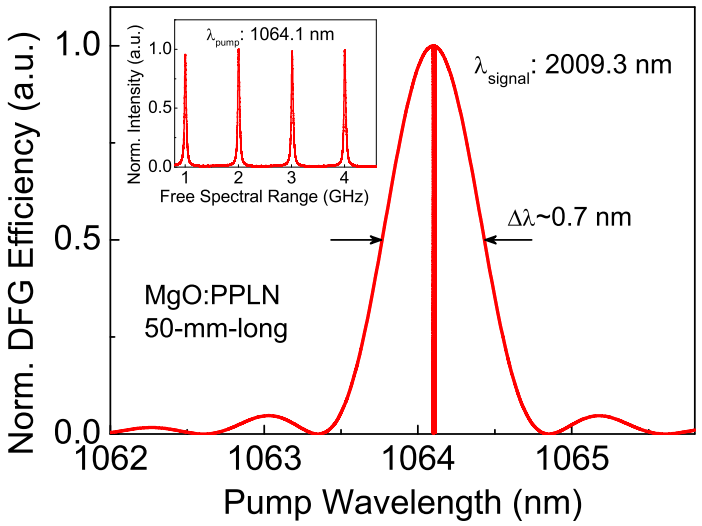


Figure 7.4: Normalized DFG efficiency as a function of pump wavelength together with the pump spectra. Inset: fringe pattern recorded using a Fabry–Perot interferometer, confirming single-frequency operation of the pump laser.

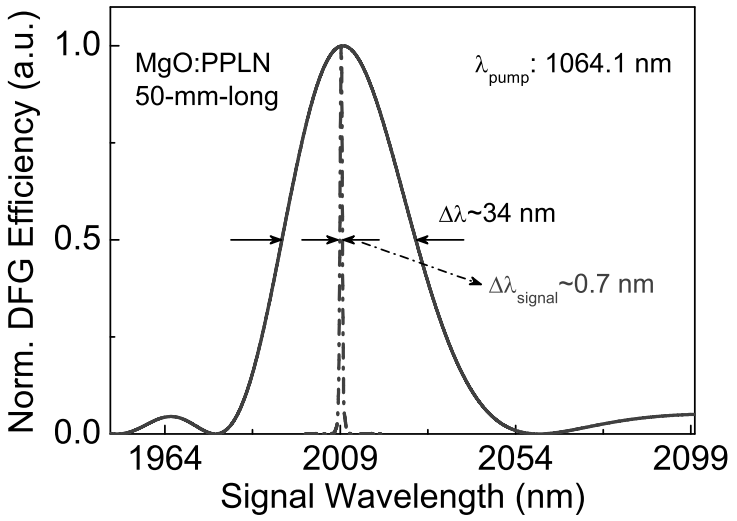


Figure 7.5: Normalized DFG efficiency as a function of signal wavelength together with the signal spectra.

interferometer with a free spectral range (FSR) of 1 GHz, shown in the inset of Fig. 7.4, confirms single-frequency operation of the pump laser. Similar calculations for a fixed pump wavelength at 1064.1 nm result in a signal FWHM spectral acceptance bandwidth of ∼34 nm, as shown in Fig. 7.5, together with the signal spectrum with a measured FWHM spectral bandwidth of ∼0.7 nm. As evident from the calculations presented in Fig. 7.4 and 7.5, the pump and signal spectra lie well within their corresponding spectral acceptance bandwidths, hence enabling efficient DFG.

## 7.3 Results and discussion

### 7.3.1 Temperature acceptance bandwidth

To characterize the DFG source, we initially performed the temperature acceptance bandwidth measurements, both at low input powers, in order to avoid any thermal effects caused by linear absorption at the pump, signal, and DFG wavelengths, as well as under high-power operation. For low-power operation, an input pump power of 5 W and a signal power of 10 W was used, generating ∼158 mW of DFG power at 2.26 µm, and the variation of the normalized DFG power with respect to the phase-matching temperature, together with the theoretical calculations, is shown in Fig. 7.6. The solid circles correspond to the experimental measurements, while the dashed line is the $\text{sinc}^2$ fit to the data. The solid line represents the calculation using focused Gaussian beam theory [28], with real experimental values for the pump and signal beam waists, as well as the input power levels in the MgO:PPLN crystal. As evident from Fig. 7.6, the optimum phase-matching temperature for low-power operation is measured to be 63.1 °C,

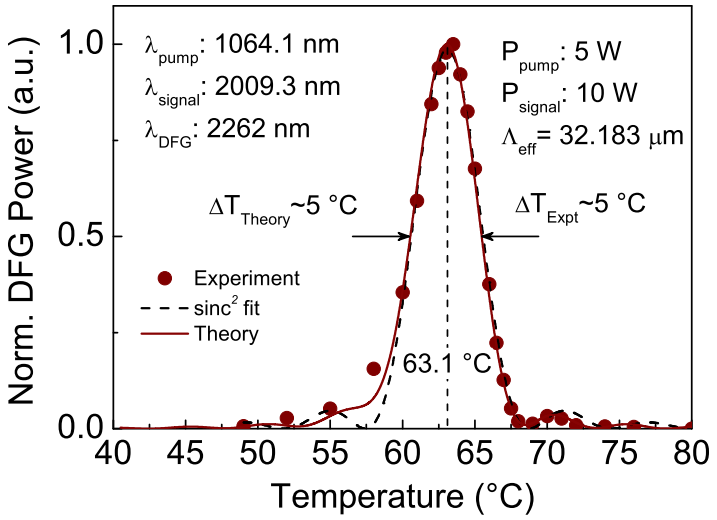


Figure 7.6: Temperature acceptance bandwidth measurement at low DFG power.

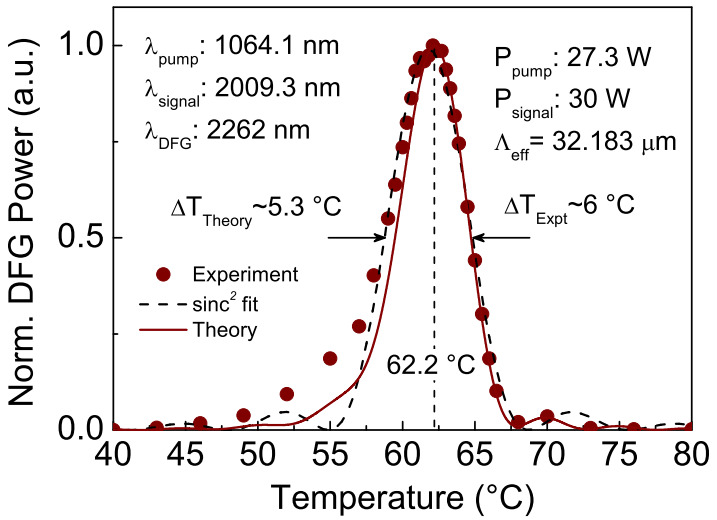


Figure 7.7: Temperature acceptance bandwidth measurements at high DFG power.

with a FWHM temperature acceptance bandwidth of 5 °C, extracted from the $sinc^2$ fit to the experimental data, which also matches perfectly with the focused Gaussian beam theory calculations. It is to be noted that a grating period of $\Lambda$ = 32.183 µm for the MgO:PPLN crystal is deduced from the theoretical calculations to match the experimentally measured phase-matching temperature. This corresponds to a deviation of $\Delta\Lambda$=0.023 µm from the actual grating period of $\Lambda$ = 32.16 µm, which is almost entirely attributed to the thermal expansion of the MgO:PPLN crystal while operating at high temperatures, as presented in the inset of Fig. 7.3. The focused Gaussian beam theoretical calculations also reveal a difference in the optimum phase-matching temperature of >2 °C, compared to the calculations using the plane-wave approximation shown in Fig. 7.3. However, at low input powers, the measured temperature acceptance bandwidth is in perfect agreement with the focused Gaussian beam theoretical simulations. Further, the theoretical simulation is also in good agreement with the $sinc^2$ fit at low power, as shown in Fig. 7.6. Similarly, for high-power operation, the pump and signal powers were set to the maximum input values of 27.3 W and 30 W, respectively, to generate 3.84 W of DFG power at 2.26 µm, with the variation of the normalized DFG power with respect to the phase-matching temperature, together with the theoretical calculations, shown in Fig. 7.7. As can be seen, at high-power, the optimum phase matching temperature is shifted towards a lower temperature of 62.2 °C, with a measured FWHM temperature acceptance bandwidth of ∼6 °C. The corresponding focused Gaussian beam theoretical simulations result in a FWHM temperature acceptance bandwidth of 5.3 °C. While the experimentally observed asymmetry in the temperature acceptance bandwidth is reproduced by the theoretical simulations, both under low-power and high-power DFG, a quan-

titative deviation of the simulations from the experimental data can be seen at high power, as evident from Fig. 7.7. This deviation, together with a reduction in the phase-matching temperature at high-power as compared to that at low-power, is a clear indication of thermal effects. These thermal effects include longitudinal as well as transverse thermal gradients across the interacting beams, caused by finite absorption at the pump, signal, and DFG wavelengths.

### 7.3.2 Power scaling, power stability, and thermal effects

We studied the power scaling performance of our DFG source with respect to the input pump as well as the signal power, with the results shown in Fig. 7.8. The solid circles correspond to the experimentally measured data, the dashed lines correspond to the fit, and the solid lines correspond to the theoretically calculated DFG power under optimum focusing conditions. At the optimum phase-matching temperature of 62.2 °C, and with maximum input signal power of 30 W, we gradually increased the pump power and recorded the DFG output power, as shown in Fig. 7.8(a). The output power increases linearly with the input pump power at a slope efficiency of ∼14.2%, resulting in a maximum DFG power of 3.84 W for maximum input signal power of 27.3 W, corresponding to a product of $P_P \times P_s$ ∼820 $W^2$. We also performed power scaling measurements as a function of the input signal power, while keeping the input pump power fixed at 27.3 W, with results shown in Fig. 7.8(b). As can be seen, the DFG output power again rises linearly, as expected, with a slope efficiency of ∼13%. The output powers recorded are the maximum powers observed at the corresponding input powers. The theoretical simulation of the DFG power using the focused Gaussian beam theory with a $d_{\text{eff}}$∼15.2 pm/V and relevant focusing conditions

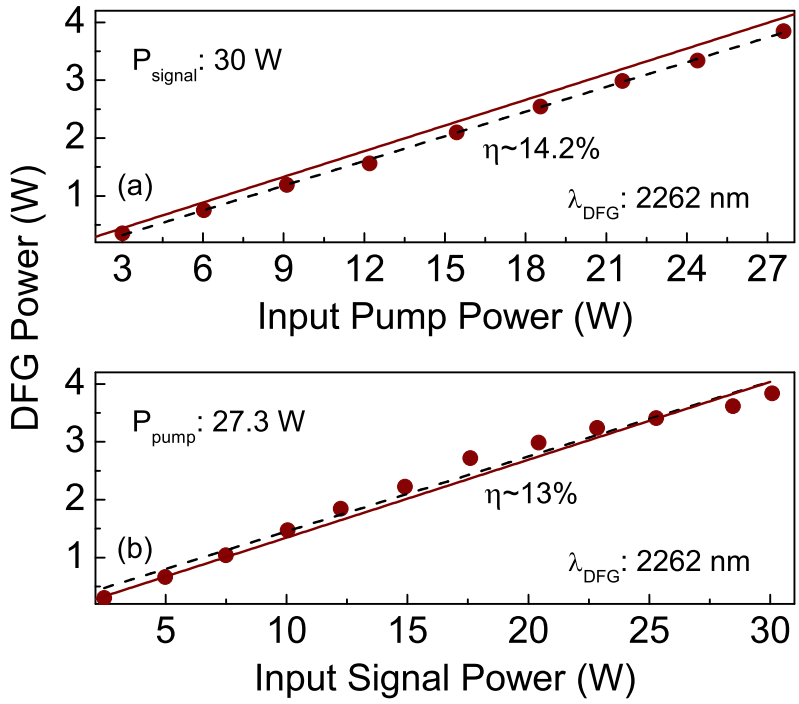


Figure 7.8: DFG power scaling as a function of (a) pump power at 1064 nm, with a constant signal power of 30 W, and (b) signal power at 2009.3 nm, with a constant pump power of 27.3 W.

used in the experiments show good agreement with the experimental measurements, indicating optimum DFG performance. Moreover, there is no evidence of saturation at maximum input powers, indicating the feasibility of further power scaling. The maximum power of 3.84 W corresponds to a single-pass DFG conversion efficiency (defined as the ratio of generated DFG output power to the product of the input pump and signal powers) of ∼0.47 %/W. The variation of the DFG efficiency as a function of the product of input pump and signal powers is presented in Fig. 7.9. For a fixed signal power of 30 W, the DFG efficiency

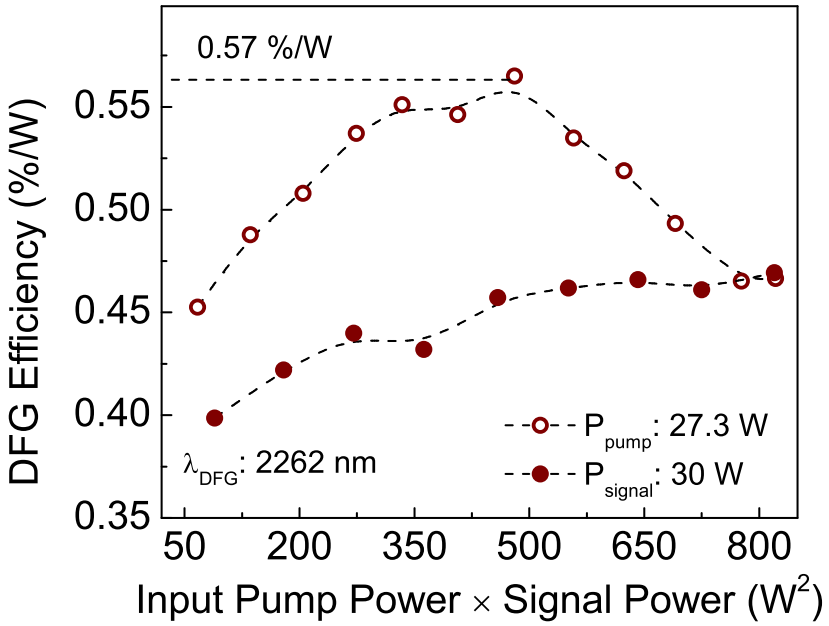


Figure 7.9: DFG efficiency as a function of the product of pump and signal power.

varies from 0.4%/W at a pump power of ∼3W ($P_P \times P_s$ ∼89 $W^2$) to 0.47%/W at a pump power of 27.3 W ($P_P \times P_s$ ∼820 $W^2$). Similar measurements for a fixed pump power of 27.3 W resulted in the variation of DFG efficiency from 0.45 %/W at ∼2.5 W ($P_P \times P_s$ ∼67 $W^2$) to 0.47 %/W at 30 W ($P_P \times P_s$ ∼820 $W^2$) of signal power, with a maximum DFG conversion efficiency of 0.57%/W. The maximum DFG efficiency is obtained for a pump power of 27.3 W and a signal power of ∼17.6 W, corresponding to $P_P \times P_s$ ∼480.5 $W^2$. Ideally, efficient parametric interaction requires one signal photon to mix with one pump photon to generate one photon at the DFG wavelength, resulting in a pump-to-signal photon ratio of 1. Although the input pumping level corresponding to $P_P \times P_s$

~480.5 $W^2$ can be achieved either by varying the pump or signal power, while one of them is fixed, it is evident from Fig. 7.9 that the maximum DFG efficiency is only achieved when the pump power is fixed at 27.3 W and the signal power is set at ~17.6 W. This combination of pump and signal powers corresponds to the ratio of pump-to-signal photon rates, $\gamma$~0.8, in the MgO:PPLN crystal, which is close to the expected value of 1. Such a condition cannot be met when fixing the signal power at 30 W and setting the pump power to ~16 W ($P_p \times P_s$ ~820 $W^2$), which results in a ratio of pump-to-signal photon rates, ~0.3, indicating that the generated DFG power is limited by the available pump power. The small deviation of the photon ratio, $\gamma$, from unity at the maximum DFG efficiency could be attributed to the unaccounted losses in our MgO:PPLN crystal. In order to

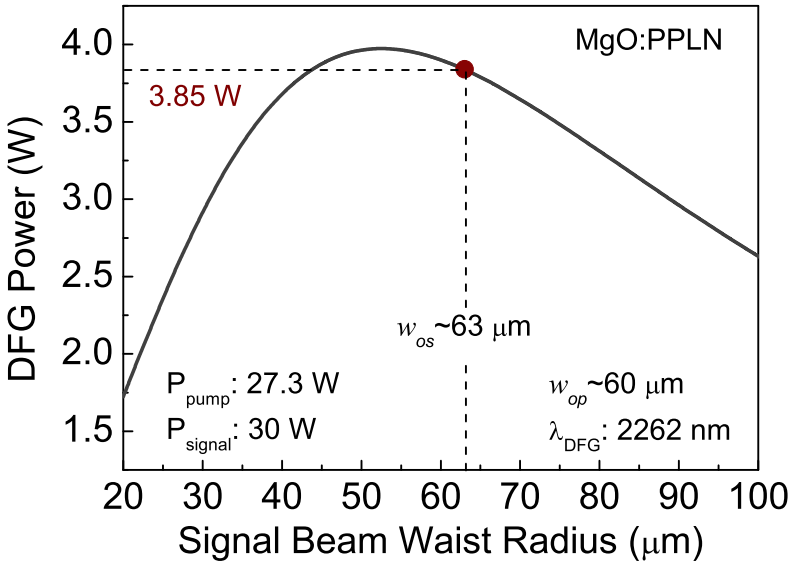


Figure 7.10: Simulated DFG power as a function of signal beam waist radius for a fixed pump beam waist radius at maximum input powers. The solid dot represents the experimentally measured DFG power.

further confirm the focusing optimization, we performed simulations to estimate the DFG power as a function of the signal beam waist radius in the MgO:PPLN crystal for a fixed pump beam waist radius of $w_{0p}$∼60 µm, at the maximum available pump and signal power levels, as presented in Fig. 7.10. The maximum achievable DFG power is found to be ∼4 W for a signal beam waist radius of $w_{0s}$∼53 µm, which is close to that used in our experiments ($w_{0s}$∼63 µm). As evident from Fig. 7.10, the experimentally measured DFG power of 3.84 W is in good agreement with theoretically estimated 3.85 W, confirming optimum signal focusing. While stronger focusing could result in slightly higher efficiency, we limited the beam waist radii to $w_{0p}$∼60 µm and $w_{0s}$∼63 µm to avoid any damage caused by the relatively low transmission of our MgO:PPLN crystal sample at the signal wavelength. We also investigated the stability of DFG output power over time from the initial condition of no input power. We observed that once the input pump and signal beams were incident on the crystal, the DFG output power would rapidly rise to the maximum value, and then gradually decline over time, as shown in Fig. 7.11, similar to what has been observed in a previous

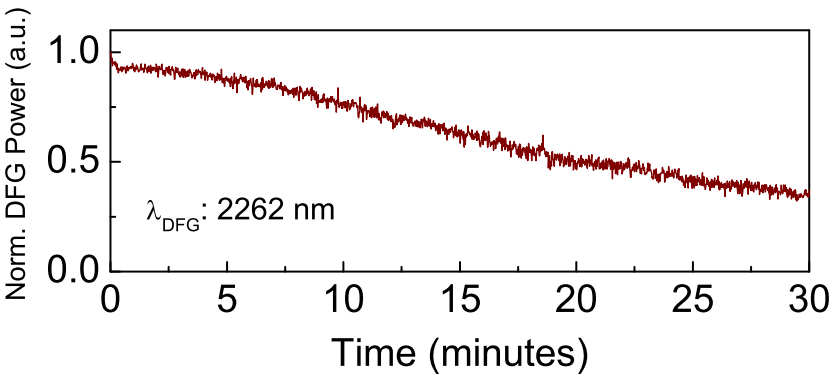


Figure 7.11: Drop in DFG output power over time.

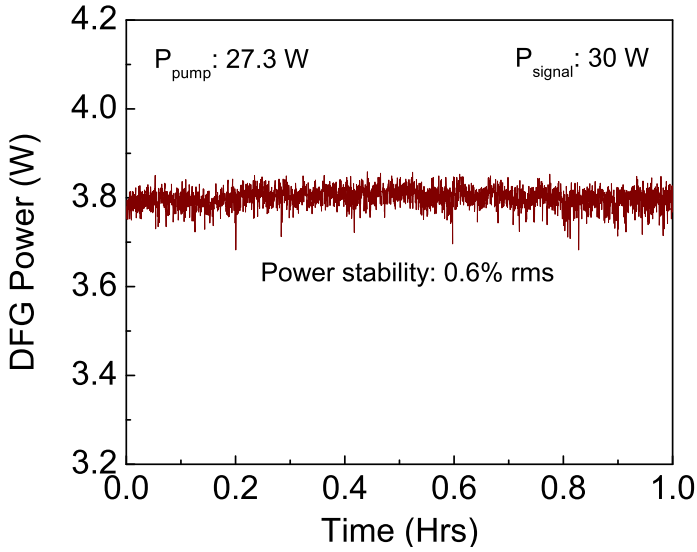


Figure 7.12: Passive power stability of the DFG output.

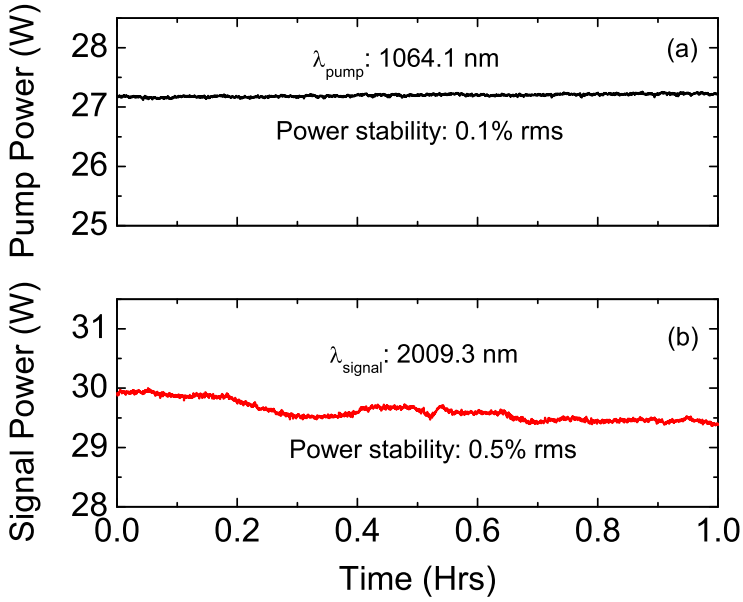


Figure 7.13: Power stability of (a) pump, and (b) signal at maximum input power levels

report [28].This drop in the DFG power at high output power levels can be attributed to the beam-pointing stability and/or thermal effects in the MgO:PPLN crystal caused by the finite linear absorption at the pump, signal, and DFG wavelengths. However, the DFG power could be recovered by optimizing the Tm-fiber laser steering mirror, $M_2$, after which the output power would remain stable for several hours. The passive power stability of DFG output after this process is shown in Fig. 7.12, where a stability better than 0.6% rms over 1 hour is recorded at the maximum output DFG power. Similar measurements of the pump and signal beam at the maximum available input power levels of 27.3 W and 30 W resulted in a passive power stability of 0.1% rms and 0.5% rms, respectively, as shown in Fig. 7.13.

On the other hand, as was previously demonstrated by our group [30,31], the linear absorption at the interacting wavelengths could lead to significant longitudinal as well as transverse thermal gradients caused by local heating in the nonlinear crystal. To study the contribution of linear absorption at the pump, signal, and DFG wavelengths to thermal effects in our 50-mm-long MgO:PPLN crystal, we performed theoretical simulations to solve the heat equation [31] with the focusing conditions used in our experiments. Further, the pump and signal powers were set to the maximum available values of 27.3 W and 30 W, respectively, to generate a maximum DFG power of 3.84 W. The thermal simulations also account for the linear variation of the DFG power along the MgO:PPLN crystal length, estimated from the focused Gaussian beam simulations. Sensitive measurements of the absorption coefficients at the pump ($\alpha_p \sim 7.61 \times 10^{-2}$ $m^{-1}$) , signal ($\alpha_s \sim 9.7 \times 10^{-3}$ $m^{-1}$), and DFG ($\alpha_{DFG} \sim 2.21$ $m^{-1}$) wavelengths were used to simulate the local temperature profiles [32]. Owing to the estimated

smallest beam waist of the DFG beam, $w_{0s}$∼43 µm, corresponding to the largest beam diameter of 404 µm on the end faces of the 50-mm-long MgO:PPLN crystal, we chose a transverse radial distance of ±250 µm from the center of the beams to simulate the temperature profiles in the focal volume. The simulated temperature profiles of the local heating caused by the independent absorption at pump, signal, and DFG beams are presented in Fig. 7.14(a)–(c). The simulated temperature profiles show that the maximum available pump power of 27.3 W leads to a temperature rise of 0.15 °C, above the experimentally measured optimum phase-matching temperature of 62.2 °C in the MgO:PPLN crystal, as shown in Fig. 7.14(a). Owing to an order-of-magnitude lower absorption coef-

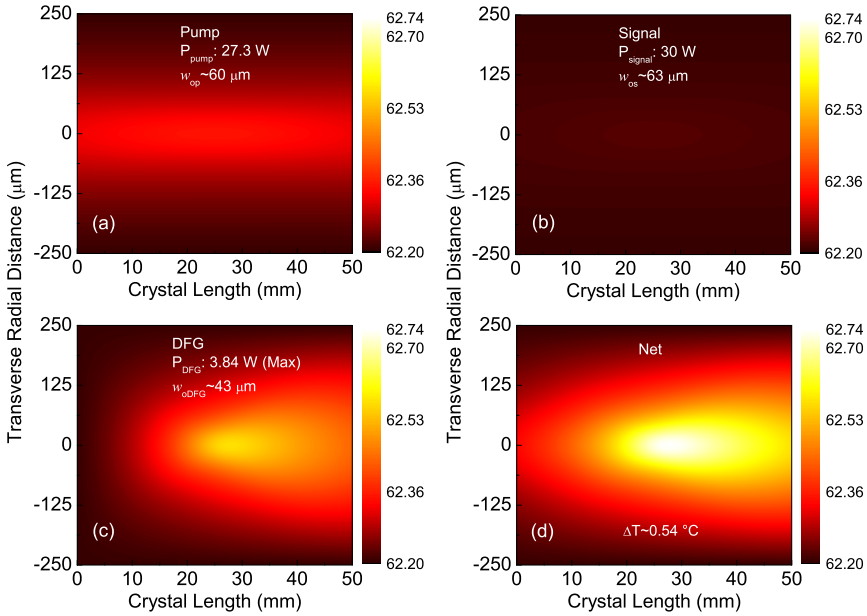


Figure 7.14: Temperature profiles in the MgO:PPLN crystal caused by local heating due to linear absorption of (a) pump, (b) signal, (c) DFG, and (d) all three interacting beams.

ficient at 2009 nm compared to 1064 nm, the signal beam is found to have a minimal contribution of ∼0.02 °C to the local heating in the MgO:PPLN crystal, even when it is exposed to the maximum available signal power of 30 W, as can be seen in Fig. 7.14(b).On the other hand, a local maxima in the absorption at 2260 nm [32] results in a relatively higher absorption coefficient at the DFG wavelength, leading to a significant temperature rise of 0.37 °C in the MgO:PPLN crystal. Further, the evolution of the DFG power as a function of the crystal length causes longitudinal as well as transverse gradients, as evident from Fig. 7.14(c). The overall temperature profile accounting for the temperature rise caused by all of the three interacting beams is shown in Fig. 7.14(d), where a net temperature rise of ∼0.54 °C is estimated. Revisiting the temperature acceptance bandwidth measurements performed while generating high DFG output power, presented in Fig. 7.7, show that the DFG power drops at a rate of ∼0.7 W/°C, beyond the optimum phase-matching temperature of 62.2 °C. Using this rate of power drop, together with the estimated temperature rise of 0.54 °C, results in a calculated DFG power drop of ∼378 mW. Considering the relatively lower transmission ($T_s$∼95.6%) of our MgO:PPLN crystal at the signal wavelength, higher temperature gradients are expected, which could further affect the DFG power drop. Hence, thermal effects are found to play a major role when generating high DFG output power at 2262 nm.

### 7.3.3 Spectral Characteristics

We also measured the DFG output spectrum using a spectrometer with a resolution of <0.5 nm, while generating the maximum power of 3.84 W, with the result presented in Fig. 7.15. The DFG spectrum has a FWHM spectral bandwidth of

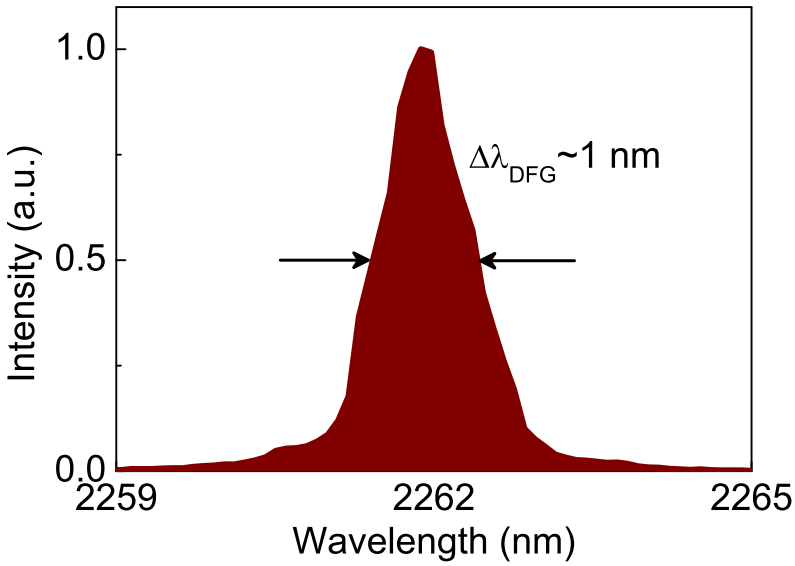


Figure 7.15: Spectrum of DFG beam at maximum output power.

~1 nm. As mentioned earlier, the signal measured using the same spectrometer exhibits a FWHM bandwidth of ~ 0.7 nm centered at 2009.3 nm, and the pump laser has a nominal linewidth of 100 kHz at 1064.1 nm. Using the measured pump and signal spectra, together with Manley–Rowe energy conservation relations, we calculate a DFG spectral width of ~0.9 nm, which is in good agreement with the measured DFG bandwidth. The long-term spectral stability of the DFG output, measured at the maximum power, is shown in Fig. 7.16. As evident, the DFG spectrum exhibits a spectral stability better than 0.01% over 1 hour, corresponding to a wavelength excursion of ~255 pm. Similar spectral stability measurements at the pump and signal wavelengths resulted in a pump frequency stability better than 1.3 GHz and a signal wavelength stability of 0.004% (~78 pm) over 1 hour, as shown in Fig. 7.17. The corresponding FWHM spectral

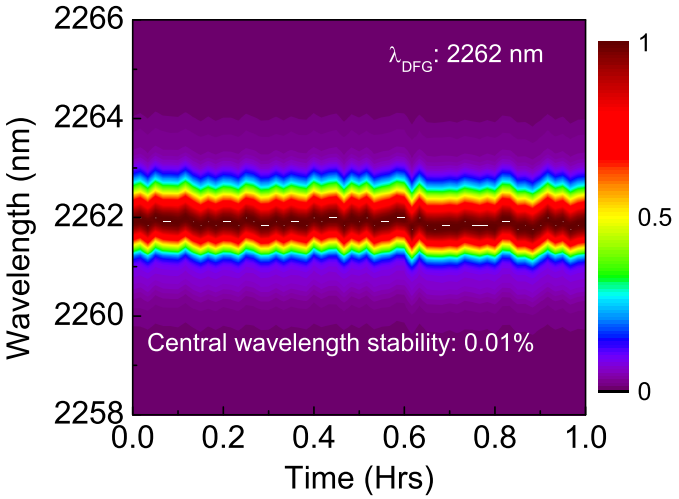


Figure 7.16: Spectral stability of the generated DFG at maximum output power.

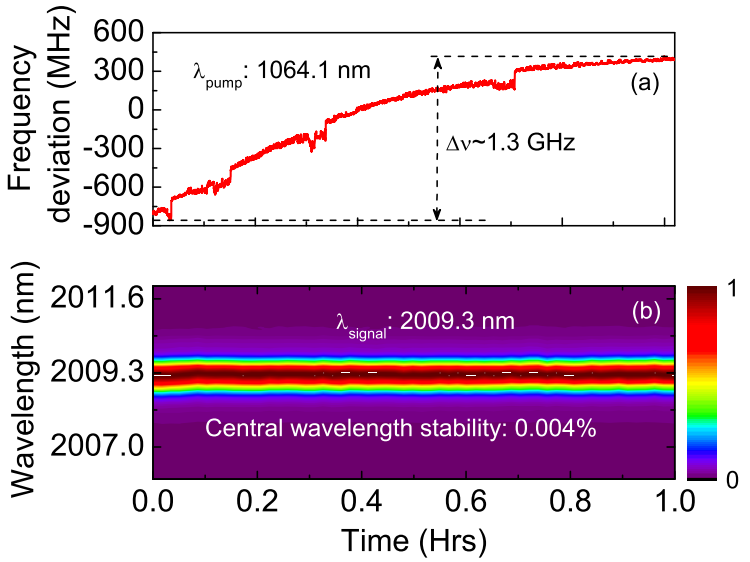


Figure 7.17: Spectral stability of (a) pump, and (b) signal at maximum input power.

bandwidth stability was measured to be 4.8% and 14% for the DFG and signal beams, respectively.

### 7.3.4 Spatial profile and beam quality

We characterized the spatial quality of the DFG output by collimating the beam and recording the profile using a pyroelectric camera, at a distance of ∼35 cm from the MgO:PPLN crystal, with the result presented in Fig. 7.18(c). As can be seen, the far-field energy distribution of the DFG beam has a single-peak Gaussian distribution with $TEM_{00}$ mode profile and a circularity of ∼99%. The corresponding spatial beam profiles of the pump and signal are presented in Fig. 7.18 (a) and (b), respectively. The DFG beam exhibits excellent beam-pointing

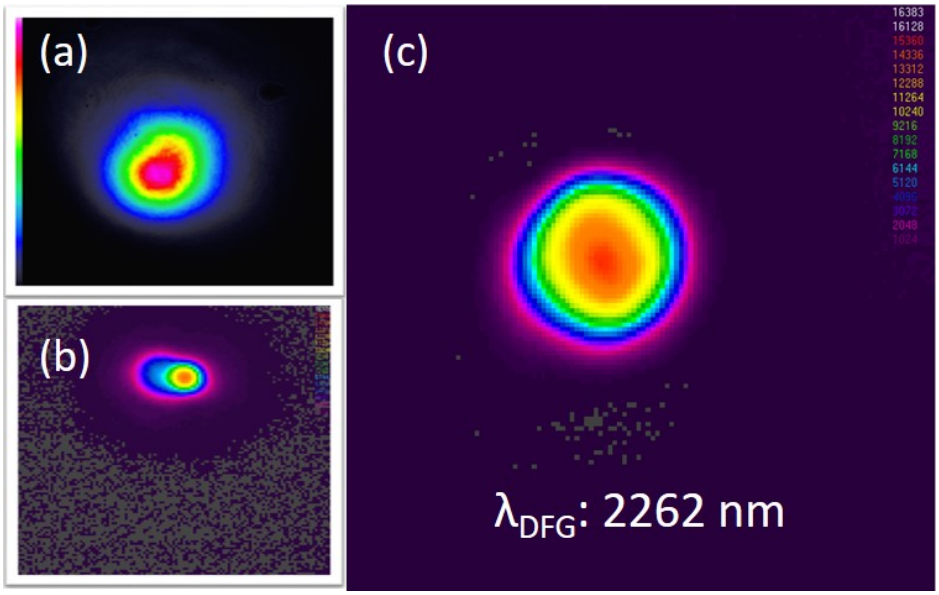


Figure 7.18: Spatial beam profile of (a) pump, (b) signal, and (c) DFG at maximum output power.

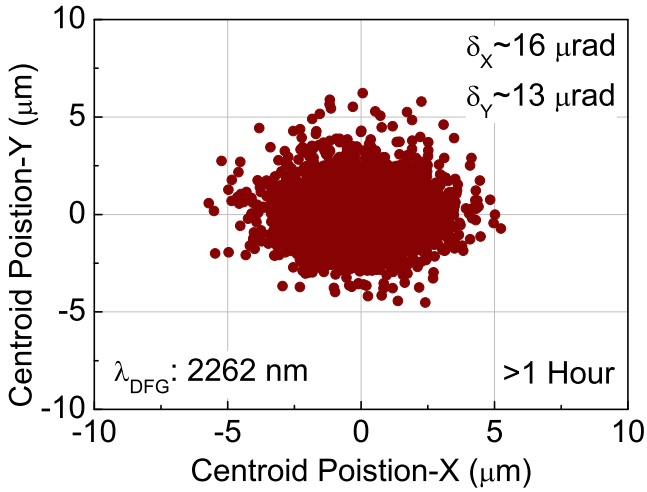


Figure 7.19: Beam pointing stability of DFG at maximum output power.

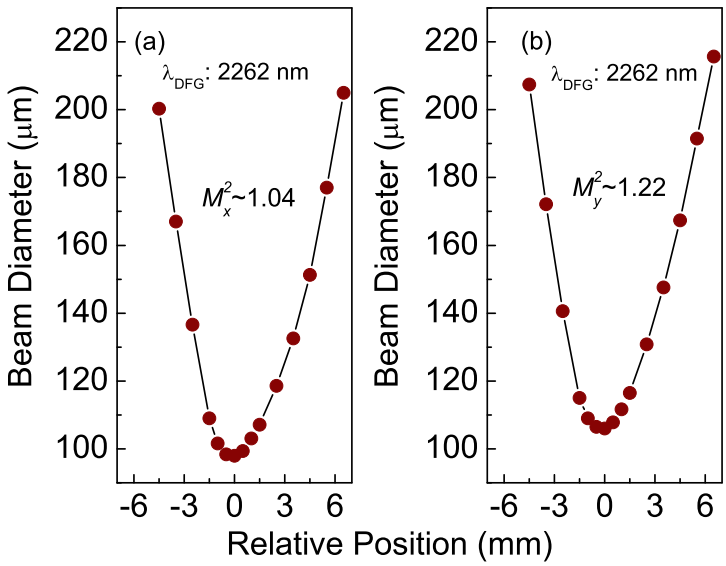


Figure 7.20: Measured beam quality factor of the DFG output in (a) horizontal, and (b) vertical direction.

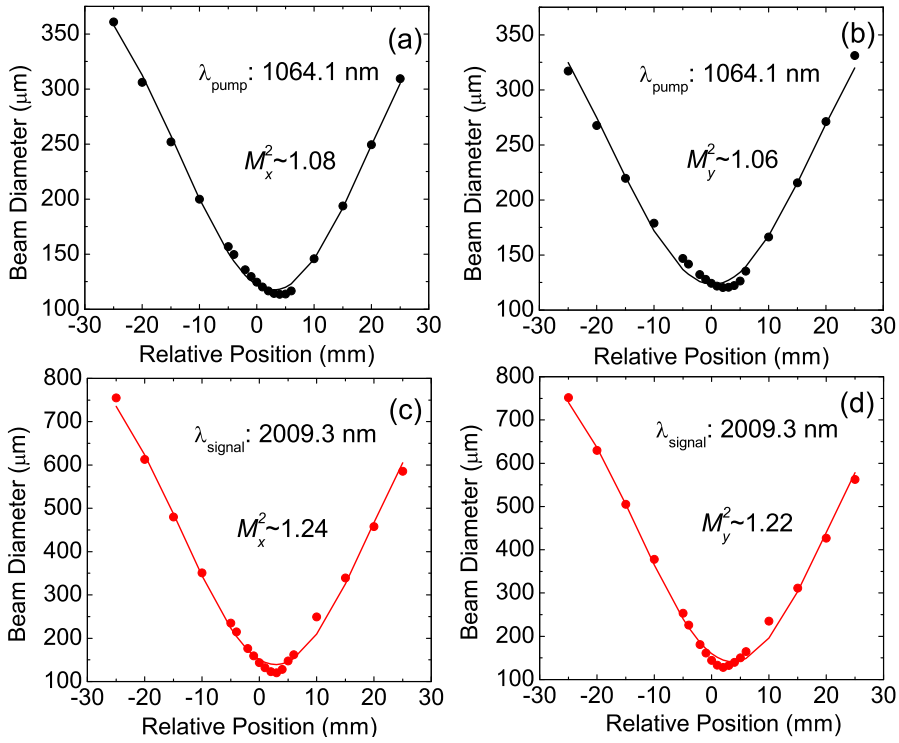


Figure 7.21: Measured beam quality factor of the pump in (a) horizontal, (b) vertical, and signal in (c) horizontal and (d) vertical direction.

stability better than 16 µrad, measured over >1 hour, as shown in Fig. 7.19. Using a scanning beam profiler and a $f$=150 mm lens, we also recorded the beam diameter along the two orthogonal directions, as a function of the relative position across the Rayleigh range through the beam waist, to estimate the beam-quality factor of the DFG beam, along with those of the pump and signal. The measurements resulted in values of $M_x^2 < 1.04$ and $M_y^2 < 1.2$ for the DFG beam, as shown in Fig. 7.20. This points to the clear feasibility of exploiting the DFG beam for subsequent applications including pumping of cw OPOs. Similar

measurements of the beam quality factor at the maximum power, as shown in Fig. 7.21 resulted in $M_x^2 < 1.08$ and $M_y^2 < 1.06$ for the pump, and $M_x^2 < 1.24$ and $M_y^2 < 1.22$ for the signal.

## 7.4 Conclusion

In conclusion, we have demonstrated a high-power source of mid-IR cw radiation at 2262 nm based on simple single-pass DFG in MgO:PPLN. using cw Yb-fiber/Tm-fiber lasers, for the first time. The DFG process is characterized by a temperature acceptance bandwidth of ∼5 °C at low power and ∼5.3 °C at high output power. Simulations based on focused Gaussian beam theory not only reproduce the asymmetry in the temperature acceptance bandwidth measurements, but also confirm the presence of thermal effects, which are experimentally verified by the observed reduction in the phase-matching temperature at high DFG output power levels. We have generated up to 3.84 W of cw power at 2262 nm at a conversion efficiency of 0.47%/W, and the DFG output scales linearly with the pump and signal input powers at a slope efficiency of 14.2% and 13%, respectively. The systematic power-scaling measurements under optimum focusing conditions confirm that the generated DFG power is limited by the available pump power. Further, a maximum DFG conversion efficiency of ∼0.57%/W is achieved when the pump-to-signal photon ratio is close to unity. The achieved maximum DFG conversion efficiency suggests the possibility of power scaling our DFG source up to ∼10 W, using a suitable high-power pump laser in the absence of thermal effects. Detailed thermal analysis shows the longitudinal and transverse thermal gradients caused by the finite absorption of the MgO:PPLN

crystal at the interacting wavelengths, confirming the origin of the sudden drop in DFG output power observed while under high-power operation, with minimal contribution from the beam-pointing instability. The spectral characterization of the generated DFG beam resulted in an FWHM spectral bandwidth of ∼1 nm, centered at 2262 nm, as expected from the Manley–Rowe analysis. The DFG beam exhibits a passive spectral stability better than 0.01% and passive power stability better than 0.6% rms over 1 hour. Moreover, the DFG beam is recorded to exhibit a beam-pointing stability better than 16 µrad over >1 hour and has excellent spatial beam quality with $TEM_{00}$ mode profile and $M^2 < 1.2$. The DFG output is reliable and repeatable. We have not observed any damage in the nonlinear crystal after long-term operation of several hours over many days. To the best of our knowledge, this is the highest cw power generated from any single-pass nonlinear frequency conversion scheme in the mid-IR. Further power scaling of the DFG source can be achieved by using longer crystals and higher input powers that are readily available with Yb-fiber and Tm-fiber lasers, paving the way for a variety of applications, including as a pump source for subsequent nonlinear frequency conversion processes for long-wave mid-IR generation.

# References

[1] G. D. Spiers, R. T. Menzies, J. Jacob, L. E. Christensen, M. W. Phillips, Y. Choi, and E. V. Browell, "Atmospheric $CO_2$ measurements with a 2 $\mu$m airborne laser absorption spectrometer employing coherent detection," Applied Optics **50**, 2098 (2011).
https://www.osapublishing.org/abstract.cfm?uri=ao-50-14-2098

[2] M. Nikodem, G. Gomółka, M. Klimczak, D. Pysz, and R. Buczyński, "Laser absorption spectroscopy at 2 µm inside revolver-type anti-resonant hollow core fiber," Optics Express **27**, 14 998 (2019).
https://www.osapublishing.org/abstract.cfm?uri=oe-27-10-14998

[3] I. Mingareev, F. Weirauch, A. Olowinsky, L. Shah, P. Kadwani, and M. Richardson, "Welding of polymers using a 2 $\mu$m thulium fiber laser," Optics and Laser Technology **44**, 2095–2099 (2012).
http://dx.doi.org/10.1016/j.optlastec.2012.03.020

[4] E. D. Onal and K. Guven, "Plasmonic photothermal therapy in third and fourth biological windows," Journal of Physical Chemistry C **121**, 684–690 (2017).
https://pubs.acs.org/doi/10.1021/acs.jpcc.6b10060

[5] W. Querido, J. M. Falcon, S. Kandel, and N. Pleshko, "Vibrational spectroscopy and imaging: Applications for tissue engineering," Analyst **142**, 4005–4017 (2017).
http://xlink.rsc.org/?doi=C7AN01055A

[6] V. Petrov, "Frequency down-conversion of solid-state laser sources to the mid-infrared spectral range using non-oxide nonlinear crystals," Progress in Quantum Electronics **42**, 1–106 (2015).
https://linkinghub.elsevier.com/retrieve/pii/S007967271500018X

[7] O. H. Heckl, B. J. Bjork, G. Winkler, P. Bryan Changala, B. Spaun, G. Porat, T. Q. Bui, K. F. Lee, J. Jiang, M. E. Fermann, P. G. Schunemann, and J. Ye, "Three-photon absorption in optical parametric oscillators based on OP-GaAs," Optics Letters **41**, 5405 (2016).
https://www.osapublishing.org/abstract.cfm?uri=ol-41-22-5405

[8] D. Garbuzov, H. Lee, V. Khalfin, R. Martinelli, J. Connolly, and G. Belenky, "2.3-2.7-$\mu$m room temperature CW operation of InGaAsSb-AlGaAsSb broad waveguide SCH-QW diode lasers," IEEE Photonics Technology Letters **11**, 794–796 (1999).
http://ieeexplore.ieee.org/document/769710/

[9] M. Garcia, A. Salhi, A. Pérona, Y. Rouillard, C. Sirtori, X. Marcadet, and C. Alibert, "Low threshold high-power room-temperature continuous-wave operation diode laser emitting at 2.26 $\mu$m," IEEE Photonics Technology Letters **16**, 1253–1255 (2004).
http://ieeexplore.ieee.org/document/1291475/

[10] S. Fu, W. Shi, Y. Feng, L. Zhang, Z. Yang, S. Xu, X. Zhu, R. A. Norwood, and N. Peyghambarian, "Review of recent progress on single-frequency fiber lasers," Journal of the Optical Society of America B **34**, A49 (2017).
https://www.osapublishing.org/abstract.cfm?uri=josab-34-3-A49

[11] B. I. Denker, V. V. Dorofeev, B. I. Galagan, V. V. Koltashev, S. E. Motorin, V. G. Plotnichenko, and S. E. Sverchkov, "A 200 mW, 2.3 $\mu$m $Tm3^{+}$-doped tellurite glass fiber laser," Laser Physics Letters **17**, 095 101 (2020).
https://doi.org/10.1088/1612-202x/aba0be

[12] J. F. Pinto, G. H. Rosenblatt, and L. Esterowitz, "$Tm^{3+}$:YLF laser continuously tunable between 2.20 and 2.46 $\mu$m," Optics Letters **19**, 883 (1994).
https://www.osapublishing.org/abstract.cfm?uri=ol-19-12-883

[13] A. Muti, M. Tonelli, V. Petrov, and A. Sennaroglu, "Continuous-wave mid-infrared laser operation of $Tm^{3+}$:$KY_3F_{10}$ at 2.3 $\mu$m," Optics Letters **44**, 3242 (2019).
https://www.osapublishing.org/abstract.cfm?uri=ol-44-13-3242

[14] A. Muti, I. Baylam, M. Tonelli, and A. Sennaroglu, "Tunable continuous-wave laser operation of Tm 3+ :BaY 2 F 8 near 23 µm," Optics Letters **45**, 4104–4107 (2020).
https://www.osapublishing.org/abstract.cfm?uri=ol-45-15-4104

[15] B.-Q. Yao, X.-M. Duan, L.-L. Zheng, Y.-L. Ju, Y.-z. Wang, G.-J. Zhao, and Q. Dong, "Continuous-wave and Q-switched operation of a resonantly pumped Ho:$YAlO_3$ laser," Optics Express **16**, 14 668 (2008).
https://www.osapublishing.org/oe/abstract.cfm?uri=oe-16-19-14668

[16] A. Godard, "Infrared (2–12 $\mu$m) solid-state laser sources: a review," Comptes Rendus Physique **8**, 1100–1128 (2007).
https://linkinghub.elsevier.com/retrieve/pii/S1631070507002368

[17] I. T. Sorokina, E. Sorokin, S. Mirov, V. Fedorov, V. Badikov, V. Panyutin, and K. I. Schaffers, "Broadly tunable compact continuous-wave $Cr^{2+}$:ZnS laser," Optics Letters **27**, 1040–1042 (2002).
https://www.osapublishing.org/abstract.cfm?uri=ol-27-12-1040

[18] I. S. Moskalev, V. V. Fedorov, and S. B. Mirov, "10-Watt, pure continuous-wave, polycrystalline $Cr^{2+}$:ZnS laser," Optics Express **17**, 2048 (2009).
https://www.osapublishing.org/oe/abstract.cfm?uri=oe-17-4-2048

[19] S. Chaitanya Kumar, R. Das, G. K. Samanta, and M. Ebrahim-Zadeh, "Optimally-output-coupled, 17.5 W, fiber-laser-pumped continuous-wave optical parametric oscillator," Applied Physics B **102**, 31–35 (2011).
http://link.springer.com/10.1007/s00340-010-4092-9

[20] M. Ebrahim-Zadeh and I. T. Sorokina, *Mid-Infrared Coherent Sources and applications.* (Springer, 2007).
https://www.springer.com/gp/book/9781402064395

[21] M. Ebrahim-Zadeh, S. C. Kumar, A. Esteban-Martin, and G. K. Samanta, "Breakthroughs in photonics 2012: Breakthroughs in optical parametric oscillators," IEEE Photonics Journal **5**, 10–15 (2013).
http://ieeexplore.ieee.org/document/6488703/

[22] M. Ebrahim-Zadeh, S. Chaitanya Kumar, and K. Devi, "Yb-Fiber-Laser-Pumped Continuous-Wave Frequency Conversion Sources from the Mid-Infrared to the Ultraviolet," IEEE Journal of Selected Topics in Quantum Electronics **20**, 350–372 (2014).
http://ieeexplore.ieee.org/document/6746032/

[23] M. Ebrahim-Zadeh, "Continuous-wave Optical Parametric Oscillators." in *Handbook of Optics* (OSA/McGraw-Hill, 2010), Vol. IV, chap. 17, third edn.

[24] W. Chen, J. Cousin, E. Poullet, J. Burie, D. Boucher, X. Gao, M. W. Sigrist, and F. K. Tittel, "Continuous-wave mid-infrared laser sources based on difference frequency generation," Comptes Rendus Physique **8**, 1129–1150 (2007).
https://linkinghub.elsevier.com/retrieve/pii/S163107050700237X

[25] O. Tadanaga, T. Yanagawa, Y. Nishida, K. Magari, T. Umeki, M. Asobe, and H. Suzuki, "Widely tunable 2.3 µm-band difference frequency generation in quasiphase-matched $LiNbO_3$ ridge waveguide using index dispersion control," Journal of Applied Physics **102** (2007).
http://aip.scitation.org/doi/10.1063/1.2767214

[26] L. Høgstedt, O. B. Jensen, J. S. Dam, C. Pedersen, and P. Tidemand-Lichtenberg, "500 nm continuous wave tunable single-frequency mid-IR light

source for C-H spectroscopy," Laser Physics **22**, 1676–1681 (2012).
http://link.springer.com/10.1134/S1054660X12110047

[27] J. Zhao, F. Jia, Y. Feng, and J. Nilsson, "Continuous-wave 3.1-3.6 $\mu$m difference-frequency generation of dual wavelength-tunable fiber sources in PPMgLN-based rapid-tuning design," IEEE Journal of Selected Topics in Quantum Electronics **24**, 1–8 (2018).
https://ieeexplore.ieee.org/document/7973076/

[28] S. Guha, J. O. Barnes, and L. P. Gonzalez, "Multiwatt-level continuous-wave midwave infrared generation using difference frequency mixing in periodically poled MgO-doped lithium niobate," Optics Letters **39**, 5018 (2014).
https://www.osapublishing.org/abstract.cfm?uri=ol-39-17-5018

[29] O. Gayer, Z. Sacks, E. Galun, and A. Arie, "Temperature and wavelength dependent refractive index equations for MgO-doped congruent and stoichiometric $LiNbO_3$," Applied Physics B **91**, 343–348 (2008).
http://link.springer.com/10.1007/s00340-008-2998-2

[30] S. C. Kumar, G. K. Samanta, and M. Ebrahim-Zadeh, "High-power, single-frequency, continuous-wave second-harmonic-generation of ytterbium fiber laser in PPKTP and MgO:sPPLT," Optics Express **17**, 13 711 (2009).
https://www.osapublishing.org/oe/abstract.cfm?uri=oe-17-16-13711

[31] S. Ghavami Sabouri, S. Chaitanya Kumar, A. Khorsandi, and M. Ebrahim-Zadeh, "Thermal effects in high-power continuous-wave single-pass second harmonic generation," IEEE Journal on Selected Topics in Quantum Electronics **20** (2014).
http://ieeexplore.ieee.org/document/6687225/

[32] M. Leidinger, S. Fieberg, N. Waasem, F. Kühnemann, K. Buse, and I. Breunig, "Comparative study on three highly sensitive absorption measurement

techniques characterizing lithium niobate over its entire transparent spectral range," Optics Express **23**, 21 690 (2015).
https://www.osapublishing.org/abstract.cfm?uri=oe-23-17-21690

# 8. Summary and outlook

In this thesis, we have demonstrated novel second-order nonlinear frequency conversion sources based on nanosecond and continuous-wave (cw) optical parametric oscillators (OPO) and cw difference-frequency-generation (DFG). The devices developed in this thesis cover a broad spectral range over 677-2479 nm. One of the OPOs demonstrated in this work was also deployed in an industrial environment for practical applications. A summary of each frequency conversion source developed is given below.

First, we developed a widely tunable cw green-pumped OPO based on fan-out grating in PPKTP. This was the first implementation of a fan-out grating design in PPKTP in a cw OPO, and by exploiting this grating structure, the OPO was continuously tunable across 741-922 nm in the signal, and 1258-1884 nm in the idler at room temperature. The tuning range could be further extend to 739 nm in the signal and to 1901 nm in the idler by increasing the crystal temperature. Signal output coupling was deployed to extract useful output power, and the OPO could deliver up to 1.65 W of total output power, with >150 mW of signal power over the entire signal tuning range and >400 mW of idler power over 66%

of the idler tuning range. The signal and idler exhibited a passive power stability better than 5.5% rms and 3.2% rms, respectively over 2.6 minutes. The signal frequency stability was better than 194 MHz over 37 seconds, and instantaneous signal linewidth was measured to be 7.5 MHz at 831 nm. The signal beam was in a Gaussian $TEM_{00}$ mode with a circularity >95%. The OPO was also characterized in a pure SRO configuration, and comparison of the results showed superior performance by deploying signal output coupling.

Second, we demonstrated the first green-pumped OPO based on MgO:cPPLT. By exploiting a fan-out grating structure, the nanosecond OPO could be continuously tuned across 689-1025 nm in the signal, and 1106-2336 nm in the idler at room temperature. By increasing the crystal temperature to 200 °C, the tuning range could be extended to 677 nm and 2479 nm in the signal and idler respectively. The OPO could deliver upto 131 mW of average power at 1476.5 nm for a pump power of 1.8 W at 25 kHz repetition rate, with passive power stability better than 3.9% rms over 30 minutes. The signal pulses had a typical duration of 6.5 ns, shorter than the pump pulses of 7 ns. Thermal effects and damage in the nonlinear crystal were observed at high pump powers.

Third, we developed the first green-pumped OPO based on MgO:PPLN in a fan-out grating structure. The cw OPO could be continuously tuned across 813-1032 nm in the signal and 1098-1539 nm in the idler at a fixed temperature of 55 °C. Optimising the pump focusing condition and using signal output coupling together with a relatively short interaction length reduce the thermal load on the crystal, resulting in superior performance of the OPO. The device could deliver a total simultaneous output power up to 714 mW at an extraction efficiency of 30%, with signal powers up to 339 mW and idler powers up to 400 mW.

The signal and idler exhibited passive power stabilities better than 2.8% rms and 1.8% rms, respectively, over 1 hour. The power scalability of the OPO was limited by linear absorption, together with green-induced infrared absorption (GRIIRA). The single frequency signal beam had an instantaneous linewidth of 3.3 MHz, and a frequency stability of 84 MHz over 72 seconds. Both the signal and idler output beams had a highly circular Gaussian profile, with the signal beam having an excellent spatial beam quality with $M^2$<1.1. Given the long-term stable output from the OPO, it can be used for practical applications requiring moderate power levels in the near-IR.

Fourth, we built a fiber-laser-pumped cw SRO as a part of an industrial internship at Radiantis, which was used to evaluate an InGaAs sensor for the aerospace sector. Based on a fan-out grating MgO:PPLN crystal, the green-fiber-pumped cw OPO was tunable across 846-1030 nm in the signal and 1100-1420 nm in the idler. The OPO could deliver upto 560 mW of idler power at 1100 nm, and the idler output was in a Gaussian $TEM_{00}$ mode with circularity of ∼87%. Compared to the pre-existing light source consisting of a monochromator on a tungsten-halogen lamp, the OPO output had significantly narrower spectra and higher output power. Using the OPO in the device characterization setup resulted in 3 orders-of-magnitude higher response in the InGaAs sensor, leading to a more precise and accurate characterization with a significantly lower measurement error. Thus using the OPO as the input light source can lead to significant improvement in the device characterization process.

Fifth, we developed a high-power source of cw mid-IR radiation at 2.26 µm based on DFG. By combining the output of Yb- and Tm-fiber lasers in a MgO:PPLN crystal, for the first time, we were able to generate up to 3.84 W of

output power at 2262 nm at a conversion efficiency of 0.47%/W, with a maximum conversion efficiency up to 0.57%/W when the pump to signal photon ratio is close to unity. The DFG power scaled linearly with input pump and signal powers, and the DFG process was characterized by a temperature acceptance bandwidth of ∼5 ˚C at low power and ∼5.3 ˚C at high output power. Theoretical simulations closely agree with experimental observations, including the presence of thermal effects. The output DFG had a FWHM spectral bandwidth of ∼1 nm with a spectral stability of 0.01% over 1 hour, and the DFG beam exhibited a passive power stability better than 0.6% rms over 1 hour. The output beam had a pointing stability better than 0.16 µrad over >1 hour, in a Gaussian $TEM_{00}$ mode profile with $M^2 < 1.2$.

As seen in this thesis, the use of fan-out grating structure leads to wide and rapid wavelength tunability, at a fixed temperature, making it possible to cover the entire wavelength tuning range of an OPO in a short period of time. Thus using such grating structures is attractive, and advantageous over the conventional process of temperature tuning in a QPM OPO. Moreover, a more precise tuning resolution can be achieved by use of a fan-out grating structure as wavelength tuning is not limited by the temperature resolution of the oven. A summary of cw green-pumped OPOs based on fan-out grating crystals is given in Table 8.1

| Crystal | Crystal length (mm) | Pump Power (W) | Signal (nm) | Idler (nm) | Signal Power (mW) | Idler Power (mW) | Extraction efficiency | Ref |
|---|---|---|---|---|---|---|---|---|
| MgO:sPPLT | 29 | 9 | 734-1033 | 1097-1929 | - | 2200 (1097 nm) | 25% | 7 of Ch. 3 |
| PPKTP | 30 | 5.5 | 741-922 | 1258-1884 | 450 (901 nm) | 1200 (1299 nm) | 30% | Ch. 3 |
| MgO:PPLN | 25 | 2.4 | 813-1032 | 1098-1539 | 339 (1019 nm) | 400 (1098 nm) | 30% | Ch. 5 |

Table 8.1: Green-pumped cw OPOs based on fan-out grating crystals.

The performance of quasi-phase-matched (QPM) cw green-pumped OPOs is strongly affected by thermal effects in the nonlinear crystals. As seen from the chapters in this thesis, all the crystals used in this thesis, PPKTP, MgO:cPPLT and MgO:PPLN had a transmission <95% at 532 nm. This residual absorption contributes to thermal effects, affecting the performance of the OPO, and also limits the power scalability and the crystal length that can be practically used. Proper management of thermal effects is required to extract good quality stable output from green-pumped OPOs based on these crystals. As demonstrated in chapter 6, cw green-pumped OPOs have great potential to be used as light source in the near-IR for various applications requiring broad tunability in single-frequency output. Improving crystal transmission losses in the green will lead to reduced thermal effects, resulting in improved power scalability and making it feasible to use longer QPM crystals, resulting in higher output powers. Moreover, improving the bulk crystal quality can make it feasible to develop a cw green-pumped OPO based on MgO:cPPLT.

The output power of the mid-IR cw DFG source can be increased by using higher input powers, that are readily available with Yb- and Tm-fiber lasers, and using longer crystal lengths. This can pave the way for using the DFG source as a input source for subsequent nonlinear frequency conversion process for long wave mid-IR generation. Wavelength tuning in the DFG process can be achieved by using a tunable input source, such as an OPO. Using a single frequency signal source in the future can result in a single-frequency output, which can subsequently be used to pump cw OPOs to develop tunable long-wave mid-IR (LWMIR) sources.

The output power of the DFG source can be further enhanced by a subsequent

DFG stage. Using a MgO:PPLN crystal identical to the first one, the undepleted pump and signal from the first DFG stage can be used for the second DFG stage. Since 2.26 µm is within the transparency range of MgO:PPLN, this will result in an overall amplification of the output power at 2.26 µm.

In the future, the undepleted 1.064 µm pump from the DFG process can be used to pump a cw OPO based on MgO:PPLN. Such OPOs are already well established. The tunable high-power idler output from this OPO could be combined with the DFG output in a nonlinear crystal such as orientation-patterned GaP (OP-GaP) for subsequent DFG to generate LWMIR. Such a source could provide useful power in the LWMIR region, and have broad tunability, with the output DFG wavelength spanning the spectral region of 5-12 µm and beyond.

In the nanosecond regime, the output of two 1.064 µm pumped OPOs can be combined for generating LWMIR. The output from one OPO would be the pump, and the second OPO, the signal, for the DFG process. One way to build two such OPOs by using a single pump laser would be to use a modified ring cavity geometry such that the undepleted pump from the first OPO is used to pump the second OPO. The tunable high-power output from the two OPOs can then be combined in a suitable nonlinear crystal such as OP-GaP or orientation-patterned Ga-As (OP-GaAs) for tunable LWMIR generation. This scheme can be extended to mid-IR pumped OPOs as well.

The Yb- and Tm-fiber lasers can be combined in MgO:PPLN in a manner similar to the DFG setup shown in this thesis for sum-frequency-generation (SFG) at 696 nm. Being a single-pass scheme, the characteristics of the input lasers are expected to be transferred to the SFG output. Using this scheme, stable high-power output in good beam quality can be expected at 696 nm.

The Tm-fiber laser can be combined with the DPSS green laser in a nonlinear crystal for SFG to develop a blue light source. However, under QPM, this requires short grating periods $\Lambda$ ~4.5 µm. Conversely, crystals such as $BiB_3O_6$ (BiBO) or $LiB_3O_5$ (LBO) can be used for birefringent phase-matching (BPM). Using a multi-crystal scheme, it should be possible to obtain high output power at 420 nm.

Using the existing fan-out structures used for green-pumping, cw idler-resonant OPOs can also be developed. Since the idler is the resonant wave in the cavity, using suitable output coupling would result in higher output power, and excellent beam quality in the extracted near-IR beam. As mentioned before, fan-out grating structure will enable wide and rapid tuning in such idler-resonant OPOs.

Future research possibilities also include the development of red-pumped cw OPOs, to take advantage of lower transmission losses in the red compared to green in the common QPM crystals, as well as eliminate GRIIRA. A suitable pump source for such OPOs in the future could be developed by using the second harmonic of a high-power single-frequency Er-fiber laser at 1.55 µm.

Bulk nonlinear frequency conversion devices, including those developed in this thesis, make it possible to achieve broad spectral coverage and high spectral brightness in a table top source. This makes them attractive for practical applications over other competing sources. Since the beginning of this century, the market for commercial OPOs has been growing, with more companies joining the fray. With continued research and development in laser technology, together with the recent development of promising new nonlinear materials such as $CdSiP_2$, OP-GaAs, OP-GaP and $BaGa_2GeSe_6$ (BGGSe), nonlinear frequency conversion will continue to be attractive for research and development for the foreseeable future.